UNIVERSITY OF CALIFORNIA,
IRVINE

Advanced Deep Learning Frameworks for Improving Near Real-time and Historical Precipitation Estimations Using Remotely Sensed Information

DISSERTATION

submitted in partial satisfaction of the requirements
for the degree of

DOCTOR OF PHILOSOPHY

in Civil and Environmental Engineering

by

Mojtaba Sadeghi

Dissertation Committee:
Professor Soroosh Sorooshian, Chair
Professor Kuo-lin Hsu
Professor Phu Nguyen
Prof. Tirtha Banerjee

2021

DEDICATION

To

My beloved parents and brothers: The pure source of joy, love, and passion and all my loved in recognition of their worth, love and efforts which made me who I am today.

TABLE OF CONTENTS

LIST OF FIGURES

LIST OF TABLES

ACKNOWLEDGMENTS

Growing up with humble beginnings in Iran, I never could have dreamt that I would have the opportunity to earn my PhD at the prestigious University of California, Irvine ("UCI"). Looking back, choosing to pursue my PhD at UCI was the best decision I ever made. Undertaking this PhD program has been one of the most challenging, life-changing, and rewarding experiences of my life. I know that I would not be where I am today, nor would I have been able to finish the program without the incredible support and guidance I received from my professors and mentors, friends and family.

First and foremost, I would like to express my deepest thanks to my academic adviser, Professor Soroosh Sorooshian, at the UCI Center for Hydrometeorology and Remote Sensing (CHRS). Professor Sorooshian has provided a friendly research environment for me and has been a great mentor, not only in my academic endeavors, but also as a friend outside of school. Professor Sorooshian has taught me out-of-the-box thinking and the importance of scientific curiosity and a hard-working mindset. Professor Sorooshian's astute guidance, unconditional advice, and enthusiastic personality inspired me to explore science more deeply, to find the best resources, and to craft solutions for any research question I encounter. I am also grateful for his generous financial support during my graduate studies. Because of Professor Sorooshian's support, I feel confident in my abilities to contribute to the field for years to come. I also feel grateful to have found a lifelong mentor and friend.

I am honored to be one of the recipients of the Maseeh Fellowship. I would like to thank Dr. Fariborz Maseeh for being so generous and sponsoring my education. My sincere thanks also goes to Professor Phu Nguyen for his patience, motivation and immense knowledge. Professor Nguyen's door was always open for me when I ran into problems or had questions during research, and I am forever grateful for his contribution to my academic growth. He also steered me in the right direction for this thesis and provided his opinion whenever I asked or needed it. I would like to thank my committee members, Prof. Kuo-lin Hsu and Prof. Tirtha Banerjee for their constructive suggestions and invaluable feedback throughout my PhD work.

Lastly, I would like to extend my heartfelt thanks to my friends and family. I would like to express my sincere gratitude to Dr. Yaling Lui for her continuous support, insightful advice and mentorship in various stages of my PhD and my life. I would also like to extend a special thanks to my genuine friends, Amin Anjileli, Hassan Anjileli, Maryam Alaeipour, Ata Akbari Asanjan, Samin Donyanavard, Iman Mallakpour, Sara Jalal, Baoxiang Pan, Matin Rahnamay Naeini, Khashayar Mohammadi, Erin Farrel and Mohammad Faridzad, who have offered me unwavering support throughout my graduate studies. I am deeply appreciative of the thoughtful discussions and inspiration these friends have provided me during the pursuit of my PhD. I would like to thank Mr. Dan Braithwaite for his technical support and assistance

with preparing the data for my research. Also, I appreciate Mrs. Diane Hohnbaum for her administrative assistance and for her kind during my Ph.D. studies.

Finally, I would like to thank my family. My family's endless love, support, encouragement and patience throughout my entire life has not only provided me with motivation to pursue my PhD, but motivation to be the best version of myself I can possibly be. I am certain that I would not be where I am today without my family, and I am forever grateful for their support.

I hope to make my mentors, professors, family and friends proud with this thesis and through all of my future contributions to the field. I am excited for my academic, professional, and personal adventure to continue.

CURRICULUM VITAE

Mojtaba Sadeghi

Education:

Doctor of Philosophy in Civil and Environmental Engineering University of California, Irvine	Jan. 2019 - Nov. 2021
Master of Science in Civil and Environmental Engineering University of California, Irvine **M.Sc. Thesis**: Performance Evaluation of the PERSIANN-CDR Products Bias-corrected with GPCP V2.3& V2.2	Sep. 2017 - Dec. 2018
Bachelor of Science in Civil Engineering Sharif University of Technology, Tehran **B.Sc. Thesis**: An integrated framework for seismic risk mitigation decision making	Sep. 2012 - Aug. 2016

Awards and Honors:

Recognized as a CERC-WET fellow for outstanding contributions to research, United States Department of Energy: U.S./ China Clean Energy Center for Water-Energy Technologies (CERC-WET).	2020-2021
Received Research Translation Group Fellowship, UCI Beall Applied Innovation.	2021
Received Orange County Outstanding Engineering Award, Orange County Engineering Council, CA	2020
Nominated for the best graduate engineering student of the year, University of California, Irvine.	2019
Received Maseeh Fellowship for academic excellent, University of California, Irvine.	2017-2018

Ranked first among 112 peer B.Sc. students of Civil and Environmental Engineering, Sharif University of Technology, Iran. 2012-2016

Dr. Tavakoli prize for achieving the highest GPA among B.S. students in Civil Engineering, Sharif University of Technology, Iran. 2012-2016

Ranked among the top 0.17 % of about 270,000 participants in the Nationwide University Entrance Exam in Mathematics and Physics, Iran 2011

Technical Summer School:

Using Satellite Observations to Advance Climate Models, **Summer 2019**
NASA's Earth Science Division -JPL Center for Climate Sciences (CCS) **Pasadena, Ca**

Publications:

Sadeghi, Mojtaba, Phu Nguyen, Matin Rahnamay Naeini, Kuolin Hsu, Dan Braithwaite, and Soroosh Sorooshian. "PERSIANN-CCS-CDR, a 3-hourly 0.04° global precipitation climate data record for heavy precipitation studies." Scientific Data 8, no. 1 (2021): 1-11.

Sadeghi, Mojtaba, Eric J. Shearer, Hamidreza Mosaffa, Vesta Afzali Gorooh, Matin Rahnamay Naeini, Negin Hayatbini, Pari-Sima Katiraie-Boroujerdy, Bita Analui, Phu Nguyen, and Soroosh Sorooshian. "Application of remote sensing precipitation data and the CONNECT algorithm to investigate spatiotemporal variations of heavy precipitation: Case study of major floods across Iran (Spring 2019)." Journal of Hydrology 600 (2021): 126569.

Sadeghi, Mojtaba, Phu Nguyen, Kuolin Hsu, and Soroosh Sorooshian. "Improving near real-time precipitation estimation using a U-Net convolutional neural network and geographical information." Environmental Modelling & Software 134 (2020): 104856.

Sadeghi, Mojtaba, Ata Akbari Asanjan, Mohammad Faridzad, Phu Nguyen, Kuolin Hsu, Soroosh Sorooshian, and Dan Braithwaite. "PERSIANN-CNN: Precipitation estimation from remotely sensed information using artificial neural networks–convolutional neural networks." Journal of Hydrometeorology 20, no. 12 (2019): 2273-2289.

Sadeghi, Mojtaba, Ata Akbari Asanjan, Mohammad Faridzad, Vesta Afzali Gorooh, Phu Nguyen, Kuolin Hsu, Soroosh Sorooshian, and Dan Braithwaite. "Evaluation of PERSIANN-CDR constructed using GPCP V2. 2 and V2. 3 and a comparison with TRMM 3B42 V7 and CPC unified gauge-based analysis in global scale." Remote Sensing 11, no. 23 (2019): 2755.

Mosaffa, Hamidreza, **Mojtaba Sadeghi**, Negin Hayatbini, Vesta Afzali Gorooh, Ata Akbari Asanjan, Phu Nguyen, and Soroosh Sorooshian. "Spatiotemporal variations of precipitation over iran using the high-resolution and nearly four decades satellite-based PERSIANN-CDR dataset." remote sensing 12, no. 10 (2020): 1584.

Nguyen, Phu, Mohammed Ombadi, Vesta Afzali Gorooh, Eric J. Shearer, **Mojtaba Sadeghi**, Soroosh Sorooshian, Kuolin Hsu, David Bolvin, and Martin F. Ralph. "PERSIANN Dynamic Infrared–Rain Rate (PDIR-Now): A Near-Real-Time, Quasi-Global Satellite Precipitation Dataset." Journal of hydrometeorology 21, no. 12 (2020): 2893-2906.

Sorooshian, Soroosh, Vesta Afzali Gorooh, Negin Hayatbini, Mohammed Ombadi, **Mojtaba Sadeghi**, Phu Nguyen, and Kuolin Hsu. "Predictability of Hydrometeorological Extremes and Climate Impacts on Water Resources in Semiarid Zones: Expectations and Reality."

Asanjan, Ata Akbari, Mohammad Faridzad, Negin Hayatbini, Vesta Afzali Gorooh, **Mojtaba Sadeghi**, Eric J. Shearer, Soroosh Sorooshian, Phu Nguyen, Kuolin Hsu, and Mehrdad Taghian. "An assessment of the unprecedented extreme precipitation events over Iran: from satellite perspective." Irvine (CA): University of California (2019).

Kabir, Hossein, and **Mojtaba Sadeghi**. "An optimized method for calculating the linear and nonlinear response of SDOF system subjected to an arbitrary base excitation." International Journal of Civil and Environmental Engineering 11, no. 3 (2017): 380-385.

Kabir, Hossein, and **Mojtaba Sadeghi**. "Unconfined Strength of Nano Reactive Silica Sand Powder Concrete." International Journal of Structural and Construction Engineering 11, no. 3 (2017): 369-373.

Kabir, Hossein, and **Mojtaba Sadeghi**. "Reactive Silica Sand Powder Concrete (RSSPC) Uniaxial Compressive Strength Investigation." The Open Access Journal of Science and Technology 5, no. 2 (2017): 1-8.

Conference Abstracts:

Sadeghi, Mojtaba, Phu Nguyen, Matin Rahnamay Naeini, Kuolin Hsu, and Soroosh Sorooshian. "PERSIANN-CCS-CDR: A 3-hourly 0.04° Global gridded Precipitation Climate Data Record (1983–present) for Extreme Precipitation Studies." In 101st American Meteorological Society Annual Meeting. AMS, 2021.

Sadeghi, Mojtaba, Phu Nguyen, K. L. Hsu, and Soroosh Sorooshian. "Application of Deep Neural Networks and Geographical Information for Improving the Near Real-time Precipitation Estimation Products." In 101st American Meteorological Society Annual Meeting. AMS, 2021.

Naeini, Matin Rahnamay, **Mojtaba Sadeghi**, Phu Nguyen, Kuo-lin Hsu, and Soroosh Sorooshian. "The performance assessment of PERSIANN-CCS-CDR rainfall estimates for hydrometeorological applications." In AGU Fall Meeting 2020. AGU, 2020.

Hsu, K. L., **Mojtaba Sadeghi**, Phu Nguyen, M. Rahnamay Naeini, Dan Braithwaite, and Soroosh Sorooshian. "PERSIANN-CCS-CDR: A Global Precipitation Climate Data Record for Hydro-climate Studies." In AGU Fall Meeting Abstracts, vol. 2020, pp. H020-01. 2020.

Sadeghi, Mojtaba, Phu Nguyen, K. L. Hsu, and Soroosh Sorooshian. "Application of Deep Neural Networks and Geographical Information for Improving the Near Real-time Precipitation Estimation Products." In AGU Fall Meeting Abstracts, vol. 2020, pp. H020-03. 2020.

Rahnamay Naeini, M., T. Yang, B. Analui, V. Afzali Gorooh, **Mojtaba Sadeghi**, A. A. Tavakoly, S. J. Turnbull, K. L. Hsu, and S. Sorooshian. "Many-objective Shuffled Complex-Self Adaptive Hybrid EvoLution (MSC-SAHEL): A flexible optimization framework for water-energy systems." In AGU Fall Meeting Abstracts, vol. 2019, pp. H52C-04. 2019.

Sadeghi, Mojtaba, Jinny Lee, Phu Nguyen, K. L. Hsu, Soroosh Sorooshian, and Dan Braithwaite. "Precipitation Estimation from Remotely Sensed Information using Artificial Neural Networks-Cloud Classification System-Climate Data Record (PERSIANN-CCS-CDR)." In AGU Fall Meeting Abstracts, vol. 2019, pp. H13P-1964. 2019.

Sadeghi, Mojtaba, Ata Akbari Asanjan, Mohammad Faridzad, Phu Nguyen, K. L. Hsu, Soroosh Sorooshian, and Dan Braithwaite. " A Convolutional Neural Network for Near-Real time Precipitation Estimation from Bispectral Satellite Information" In 5th CUAHSI conference on HydroInformatics for scientific knowledge, informed policy, and effective response, 2019.

Sadeghi, Mojtaba, Ata Akbari Asanjan, Mohammad Faridzad, Phu Nguyen, K. L. Hsu, Soroosh Sorooshian, and Dan Braithwaite. "Precipitation Estimation from Remotely Sensed Information Using Deep Neural Networks" In 12th International Precipitation Conference (IPC12), 2019.

Sadeghi, Mojtaba, V. Afzali Gorooh, Phu Nguyen, K. L. Hsu, and Soroosh Sorooshian. "Performance Evaluation of PERSIANN-CDR Constructed Using GPCP V2. 2 vs. GPCP V2. 3." In AGU Fall Meeting Abstracts, vol. 2018, pp. H43F-2494. 2018.

Invited Presentations:

Thermal and Microwave Remote Sensing: Application for Water Vapor, Cloud and Precipitation 2020-2021
Workshop: An international distance learning course organized by the Atmospheric Science and Meteorological Research Center (ASMERC) with collaboration of World Meteorological Organization (WMO) Tehran-RTC, Meteo-France, National Institute.

Oral Presentations:

American Geophysical Union, Fall Meeting 2020, Application of Deep Neural Networks and Geographical Information for Improving the Near Real-time Precipitation Estimation Products. December 2020

American Meteorological Society, 101st Annual Meeting, January 2021
PERSIANN-CCS-CDR: A 3-hourly 0.04 Global gridded Precipitation Climate Data Record (1983present) for Extreme Precipitation Studies

Journal Reviewer for:

- IEEE Transactions on Neural Networks and Learning Systems
- Journal of Hydrology
- Journal of Atmospheric Research
- Journal of Hydrometeorology
- Journal of Environmental Science and Pollution Research
- International Journal of Climatology
- Journal of Remote Sensing
- Journal of Remote Sensing
- Journal of Remote Sensing
- Journal of Atmosphere
- International Journal of Remote Sensing
- Journal of Hydroinformatics
- Journal of Computers and Geo-sciences
- Journal of Hydrologic Engineering
- Journal Natural Hazards
- Journal of Atmospheric and Oceanic Technology

Teaching Experience:

Engineering Hydrology, Instructor: Prof. Soroosh Sorooshian — Fall 2021
University of California, Irvine

Hydrological System, Instructor: Prof. Soroosh Sorooshian — Spring 2020, Spring 2021
University of California, Irvine

Engineering Hydrology, Instructor: Prof. Kuolin Hsu — Fall 2020
University of California, Irvine

Introduction to Computational Engineering Problem Solving, — Fall 2019
Instructor: Prof. Kuolin Hsu
University of California, Irvine

Open Channel Hydraulics, Instructor, Prof. Ahmad Abrishamchi — Fall2014, Fall 2015, Fall 2016
Sharif University of Technology, Tehran

Design of Reinforced Concrete Structure I, Instructor: Prof. Morteza Eskandari
Sharif University of Technology, Tehran — Fall 2016

Design of Reinforced Concrete Structure II, Instructor: Prof. Morteza Eskandari
Sharif University of Technology, Tehran — Spring 2016

Fluid Mechanics, Instructor: Prof. Mohammad Raie
Sharif University of Technology, Tehran — Spring 2015

Open Channel Hydraulics, Instructor: Prof. Mohammad Raie
Sharif University of Technology, Tehran — Spring 2014

Volunteer Experience:

Cope Health Scholar at Kaiser Permanente Hospital in Irvine — 2020-Present

NASA Data Intensive Research and Education Center for STEM workshop — 2019

Graduate Interconnect Peer Mentor at University of California, Irvine — 2018-2019

Volunteer administrator for managing the "How to apply" meetings to share the successful experience of previous applicants in Tehran University of Technology — 2017

Technical Skills:

Computer Languages	Python, MATLAB
Geospatial Tools	GDAL, Arc-GIS
Computer Vision Processing	TensorFlow, Theano, Keras
Cloud-based Computing	AWS, HPC, Linux

ABSTRACT OF THE DISSERTATION

Advanced Deep Learning Frameworks for Improving Near Real-time and Historical Precipitation Estimations Using Remotely Sensed Information

By

Mojtaba Sadeghi

Doctor of Philosophy in Civil & Environmental Engineering

University of California, Irvine, 2021

Professor Soroosh Sorooshian, Chair

Accurate and timely precipitation estimates are critical for many hydrological applications, including monitoring and forecasting natural disasters, developing water resources management and planning strategies, as well as conducting climatological studies. Despite having high-resolution satellite information, precipitation estimation from remotely sensed data still suffers from methodological limitations. State-of-the-art deep learning algorithms, renowned for their skill in learning accurate patterns within large and complex data sets, appear well-suited to the task of precipitation estimation. Contents of this dissertation are based on the collection of a number of reviewed journal articles which have been published over the course of my doctoral research.

By leveraging the deep learning algorithms with an ample amount of high-resolution satellite datasets, I introduce one historical and one near-real time precipitation estimation dataset: 1) The near-real time dataset called Precipitation Estimation from Remotely Sensed Information using Artificial Neural Networks-Convolutional Neural Networks (PERSIANN-

CNN). This developed near- real time dataset provides precipitation estimates at 0.08-degree spatial and an hourly temporal resolution. 2) The historical precipitation estimation dataset named Precipitation Estimation from Remotely Sensed Information using Artificial Neural Networks-Cloud Classification System-Climate Data Record (PERSIANN-CCS-CDR). This dataset offers precipitation estimates at 0.04° spatial and 3-hourly temporal resolutions from 1983 to present over the globe.

Chapter 2 and 3 investigate the application of two different deep neural networks algorithms for improving the near-real time precipitation estimation. Most near real-time precipitation retrieval algorithms utilize infrared (IR) information as their input due to its fine spatiotemporal resolution and near-instantaneous availability. Their sole reliance on IR information is problematic. Indeed, it limits their ability to learn different mechanisms of precipitation during training, resulting in less accurate estimates. However, recent advances in the field of machine learning offer attractive opportunities to improve the precipitation retrieval algorithms. Chapters 2 investigates the effectiveness of adding Water Vapor (WV) channels from geostationary satellites to IR information and the application of convolutional neural networks for improving the accuracy of near real-time precipitation algorithms. Chapter 3 further improves the model introduced in Chapter 2 by adding geographical information (i.e., latitude and longitude) to IR information and utilizing a U-Net-based convolutional neural network. The developed dataset called PERSIANN-CNN, which provides near-real time precipitation estimates at the spatial resolution of 0.08-degree and at an hourly time scale over the CONUS. Results demonstrate that the proposed model (PERSIANN-CNN) provides more accurate rainfall estimates compared to the current operational near-real time precipitation datasets at various temporal and spatial scales.

Chapter 4 and 5 introduce a new historical precipitation estimation dataset through introducing a new framework for bias correcting and downscaling the precipitation estimates. Accurate, long-term, global precipitation estimates, especially for heavy precipitation rates, at fine spatial and temporal resolutions is vital for a wide variety of climatological studies. Most of the available operational precipitation estimation datasets provide either high spatial resolution with short-term duration estimates or lower spatial resolution with long-term duration estimates. Furthermore, previous research has stressed

that the available satellite-based precipitation products show poor performance for capturing extreme events at high temporal resolution. Therefore, there is a need for a precipitation product that reliably detects heavy precipitation rates with fine spatiotemporal resolution and a longer period of record. Chapters 4 and 5 introducing a new historical dataset that address these limitations by introducing a bias correcting and a downscaling framework, respectively. The developed dataset (called PERSIANN-CCS-CDR) provides precipitation estimates at 0.04° spatial and 3-hourly temporal resolutions from 1983 to present over the global domain of 60°S to 60°N. PERSIANN-CCS-CDR shows improved performance compared to PERSIANN-CDR in representing the spatiotemporal resolution, magnitude, and spatial distribution patterns of precipitation, especially for extreme events.

In chapter 6, the applications of the developed datasets as well as PERSIANN family datasets are assessed to investigate the spatiotemporal variations in heavy precipitation events that occurred in early spring (March 21st to April 20th) over Iran. The Results show that PERSIANN family datasets are an attractive dataset for detecting the near-real time and historical precipitation estimates.

CHAPTER ONE:

INTRODUCTION

1.1. Overview of near-real time precipitation estimation algorithms

Precipitation is the main driver of the hydrological cycle and it plays a key role in hydro-meteorological and climate studies (Trenberth et al. 2003). Accurate and timely precipitation estimates are of paramount importance for water resources management, as well as many hydrological applications such as flood forecasting, drought modeling, and soil moisture monitoring (Beck et al. 2017, Miao et al. 2015). Rain gauges, weather radars, and earth-observing satellites are the most common instruments for estimating precipitation. Ground-based rain gauges provide direct rainfall measurement and are considered the most reliable method for rainfall estimation (Huffman et al. 1997). Yet, the inadequacy and the sparsity of gauge networks over remote and high elevation areas that receive large amounts of precipitation tend to undermine the applicability of gauge-based estimates (Gehne et al. 2016, Huffman et al. 2001). Additionally, there are no gauge data over water bodies and oceans (Maggioni et al. 2016). Radar networks provide a continuous precipitation measurement with high temporal and spatial resolutions (Habib et al. 2012). However, radar networks do not cover many countries and remote regions around the world (Guo et al. 2015, Yilmaz et al. 2005). Additionally, they suffer from beam overshooting and beam blockage by mountains, which makes them suitable mostly for flat regions (Germann et al. 2006).

Satellite-based quantitative precipitation estimation (QPE) is a promising alternative to ground-based rain gauge and radar measurements, offering global precipitation estimates with high spatial and temporal resolutions over land surfaces and oceans (Sun et al. 2018). Satellite-based QPEs can be derived from a range of observations with different types of sensors. The most commonly used satellite sensors are infrared (IR) from geosynchronous Earth orbiting (GEO) satellites and passive microwave (PMW) data from low-Earth orbiting (LEO) satellites (Michaelides et al. 2009, Sorooshian et al. 2002, Weng et al. 2003). PMW observations have the advantage of being directly retrieved by measuring microphysical information including both liquid and frozen hydrometeors within the clouds, while IR information is limited to cloud-top information (Joyce et al. 2004). PMW sensors are only onboard LEO satellites which provide a relatively poor temporal and spatial sampling (Behrangi et al. 2009, Marzano et al. 2004). IR images are produced at least once per hour

and provide useful information regarding cloud-top texture (e.g. size and phase of cloud particles) (Grecu et al. 2004). In addition, the resolution of IR sensors is around 4 km, while the resolutions of LEO sensors are typically not better than 50 km over the oceans and 10 km over land (Kidd and Levizzani 2011). Thus, the IR-based products have the advantage in terms of temporal and spatial resolutions among other satellite-based QPEs and better meet the requirements many near real-time applications(Sadeghi et al. 2021b). Such applications include monitoring the complete evolution of local precipitation events and flash floods, where the life cycle of most storms occurs within a short period of time and is confined to a small area (Arkin and Meisner 1987, Behrangi et al. 2009).

Different methodologies have been proposed in order to establish the relationships between IR observations and precipitation rate (Ba and Gruber 2001, Behrangi et al. 2009, Bellerby et al. 2000, Hsu et al. 1997, Roebeling and Holleman 2009). One well-known algorithm and product is Precipitation Estimation from Remotely Sensed Information using Artificial Neural Networks (PERSIANN) which relates cloud top temperature data obtained from IR imagery to the precipitation rate (Hsu et al. 1997). PERSIANN is a near real-time data set with 0.25 degree (i.e. 25 km) spatial and hourly temporal resolutions (Sorooshian et al. 2000). PERSIANN-Cloud Classification System (PERSIANN-CCS, Hong et al. 2004) is the next generation of PERSIANN, which improves the estimation algorithm by employing techniques to identify the cloud patch features. PERSIANN-CCS data is a product at 0.04 degree (i.e. 4 km) spatial and half-hourly temporal resolutions. Both PERSIANN and PERSIANN-CCS extract information based on manually defined features including coldness, texture, and geometry, which limits the capability of these products for precipitation estimation (Hong et al. 2004, Shen 2018). Manual feature extraction is always limited due to the tendency of humans to select the most relevant and physically obvious features that have a direct impact on a phenomenon. However, due to the complexity and non-linear behavior of the precipitation phenomena, there may be some factors hidden to humans that play significant roles in increasing the accuracy of simulations. Additionally, in practice, human-based feature selection is biased toward the most obvious factors due to insufficient time to explore and test all related and co-related factors. Therefore, applying more advanced data-driven methodologies for automatically extracting features from the input data will enhance precipitation estimation accuracy(Mosaffa et al. 2022).

Recent advances in the field of Machine Learning (ML) offer exciting opportunities to expand our knowledge about the Earth system (Lary et al. 2016). Among the different machine learning methods, the Deep Neural Network (DNN) method is a fast-growing branch characterized by its flexibility and capacity to deal with huge and complex data sets, especially extracting features from a large amount of image data (Bengio et al. 2007, Hinton et al. 2006). DNN's ability to deal with huge amounts of data allows us to better exploit spatial and temporal structures in the data from multi-satellite imageries for precipitation estimation. Akbari Asanjan et al. (2018) employed a deep neural network framework and proposed a short-term quantitative precipitation forecasting model. A more closely related work for applying DNNs for precipitation estimation is the research conducted by Tao et al. (2018) , who employed the stacked denoising auto-encoders technique. The proposed model, referred to as PERSIANN stacked denoising auto-encoders (PERSIANN-SDAE), utilizes infrared (IR) and water vapor (WV) channels to detect rain/no-rain and then estimate the precipitation. The results suggest that PERSIANN-SDAE can better capture both the spatial pattern and the peak precipitation compared to PERSIANN-CCS. Although PERSIANN-SDAE has the advantage of automatic feature extraction from the IR data, it cannot efficiently use the neighborhood information in retrieving the rain rate at each pixel due to an inefficient structure for learning from image data sets. In other words, for each output pixel estimated by SDAE and in general Fully-Connected (FC) neural networks, information from the corresponding pixel of the input data sets is utilized instead of using information from neighboring pixels in the same image. The inefficient structure of SDAE and FC networks leads to results focusing on the pixel-to-pixel relationship between cloud-top temperature and rainfall rate. However, in addition to the one-to-one relation of IR temperature and rain rate, local spatial variations in IR provide useful factors for accurate rainfall estimation. For example, frontal rainfalls can be well-described by spatial variations in IR. Frontal rainfalls happen when cold and warm regimes collide, and this is only captured by leveraging spatial patterns.

1.2. PERSIANN-CNN dataset

Convolution Neural Networks (CNNs) are one of the most popular and efficient types of DNN frameworks (Rezaee et al. 2018). CNNs rely on efficient structures for learning the essential

features without requiring prior feature extraction and thereby offer a greater generalization capability (Long et al. 2017). One of the main advantages of CNNs for image processing is that they can more efficiently use local neighborhood features via convolution transformation (Miao et al. 2015). In other words, CNNs use the n×n neighborhood pixels centered by the targeted pixel to estimate the rain rate at that pixel. This feature is due to the CNN structure, which allows sharing the same filter in a single layer. By offering this unique feature, the CNN can extract valuable features from the hidden layer without requiring large amounts of data. This greatly reduces the number of parameters in the network and allows the model to have more layers (deeper structure), which are good for capturing more complex patterns, and to be more efficient by reducing the number of parameters compared to FC models(Chen et al. 2016).

Due to the rapid growth in the amount of annotated data and the uniqueness of CNN structures, remote sensing and hydrology communities have exploited CNN techniques for many applications. These include land cover and land use classification (Castelluccio et al. 2015, Chen et al. 2014, Luus et al. 2015, Makantasis et al. 2015, Rezaee et al. 2018, Ševo and Avramović 2016), image segmentation (Basaeed et al. 2016, Längkvist et al. 2016), object localization(Long et al. 2017, Salberg 2015), extreme event detection(Liu et al. 2016), urban water flow and water level prediction (Assem et al. 2017), tropical cyclone intensity estimation(Pradhan et al. 2017), and extreme precipitation prediction (Zhuang and Ding 2016). The CNN structure can also be utilized to address the drawback of PERSIANN-SDAE to efficiently utilize neighborhood pixel information for rain-rate estimation (Shen 2018). The CNN offers a viable tool for precipitation estimation problems since it can gain more abstract and more expressive information from multi-spectral channels. Recently, a CNN was implemented to estimate precipitation based on the dynamic and moisture fields from numerical weather model analysis (Pan et al. 2018). Pan et al. (2018) showed that the CNN technique can improve numerical precipitation estimation on the west and east coasts of United States. Miao et al. (2019) applied a combination of CNN and Long Short Term Memory (LSTM) to improve the resolution and accuracy of precipitation estimates based on dynamical simulations. Both of these studies employ predictions from the numerical model's resolved dynamic and moisture fields. However, there is no remote sensing information being explicitly utilized in their models.

In this study, we propose a framework for real-time precipitation estimation using the IR and WV information and applying a CNN model. The National Centers for Environmental Prediction (NCEP) Stage IV Quantitative Precipitation Estimation (QPE) have been utilized as the ground-truth observation for training the model. The proposed model will be called PERSIANN–Convolutional Neural Network (PERSIANN-CNN) hereafter. Then, the effectiveness of this model has been evaluated, and its performance is compared with two baseline models. The detailed objectives of chapters 2 and 3 are:

1) Introduce a rainfall estimation model based on the bispectral satellite information (IR and Water Vapor (WV) channels) using convolutional neural networks.
2) Evaluate the performance of the proposed model (PERSIANN-CNN) through various categorical and continuous verification indices. Contrasting the proposed model with PERSIANN-CCS and PERSIANN-SDAE at hourly and daily time scales.
3) verify the performance of PERSIANN-CNN in capturing the characteristics of an extreme rainfall event throughout its evolution stages.
4) investigate the effectiveness of adding geographical information (i.e. latitude and longitude) to IR information and the application of a U-Net-based convolutional neural network for improving the accuracy of retrieval algorithms.

1.3. Overview of historical precipitation estimation datasets

Precipitation is widely recognized as the main driving component for the global hydrological cycle and has an essential role for regulating the climate system (Trenberth et al. 2003; Wang et al. 2012). Providing reliable estimation of precipitation, especially heavy precipitation, at fine spatial and temporal resolutions is crucial for many hydrological applications, including the development of water resources management and planning strategies, the development of early warning systems, as well as climatological studies. (Hou et al. 2014; Nguyen et al. 2018b; Mehran and AghaKouchak 2014; Nguyen et al. 2015). Gauge, radar, and satellite instruments are considered primary sources for measuring precipitation (Tapiador et al. 2012). Ground-based rain gauges directly measure precipitation; however, their uneven and sparse distribution, especially over oceans and remote regions, limits their application for developing a global high spatial resolution precipitation dataset (Michaelides et al. 2009; Sun et al. 2018). Radar networks, which provide continuous precipitation

measurements with high spatiotemporal resolutions, are viable alternatives for ground-based rain networks. However, the establishment of a global radar network is difficult due to high installation and maintenance costs (Maggioni et al. 2016; Habib et al. 2012).

In recent decades, rapid advancement in remote sensing technologies has brought an unprecedented opportunity for offering homogenous precipitation estimation at fine spatial and temporal resolutions over the globe (Kidd and Levizzani 2011; He et al. 2018; Sorooshian et al. 2011; Sadeghi et al. 2019c). During the last three decades, a series of satellite-derived global precipitation datasets have been developed and made operational (Maggioni et al. 2016; Sun et al. 2018). Operational satellite-based precipitation products vary from 0.04 to 2.5 degrees in terms of spatial resolution, from 30 minutes to monthly in terms of temporal resolution and up to 40 years of temporal span. These datasets have been designed for different applications and their usability depends upon the type of application along with the accuracy, latency, and temporal and spatial resolutions of the estimates.

Climate studies applications require long-term precipitation records (Wentz et al. 2007); the World Meteorological Organization (WMO) reported that at least 30 years of weather information is needed for climatological studies (Sadeghi et al. 2020). Therefore, a reliable long-term global precipitation estimation product is crucial for climatological studies. On the other hand, several studies have shown that spatial–temporal variability of precipitation plays an important role in catchment response and performance of hydrological models (Lobligeois et al. 2014; Vieux and Imgarten 2012; Huang et al. 2019; Cristiano et al. 2017; Ficchì et al. 2016; Lee et al. 2019). For example, Das et al. (2008) explored the sensitivity of distributed, semi-distributed and semi-lumped models to the spatial and temporal resolution of the precipitation input. Their results indicated that low spatial and temporal resolutions of precipitation estimates are responsible for the low efficiency of distributed models compared to simpler model structures. Lobligeois et al. (2014) investigated the impact of the spatial resolution of precipitation inputs on the performance of semi-distributed hydrological models over 181 catchments with a variety of sizes and climate conditions. They concluded that semi-distributed models significantly outperform lumped models when precipitation inputs have higher spatial resolution, while they perform similarly when precipitation have low spatial resolution. Huang et al. (2019)

explored the sensitivity of hydrological model performance to the temporal resolution of precipitation inputs using lumped and distributed models. They showed that providing sub daily precipitation estimates rather than daily inputs can significantly improve the performance of the hydrologic model. Ochoa-Rodriguez et al. (2015) investigated the impact of spatial and temporal resolution of rainfall inputs on hydrological modeling and urban hydrology. They showed that spatial and temporal variability of precipitation information translates into large variations in flows; as a result, developing a precipitation dataset with high spatial and temporal resolution is needed in order to represent urban runoff processes well.

Nonetheless, most of the available operational precipitation products are either high resolution/short-duration estimates or low resolution with long-term estimates (Kidd and Levizzani 2011); therefore, there is a need for providing precipitation products with both fine spatial and temporal resolution and a long period of record(Sadeghi et al. 2021a). Precipitation products with such attributes would provide the opportunity for researchers to study the spatial details and complete evolutions of extreme events including hurricanes and convective storms in the context of historical events (Funk et al. 2015; Yoshimoto and Amarnath 2017). Most of the currently available satellite-based precipitation estimation products are not ideal for detecting extreme events at high temporal resolutions (3-hourly) (Mehran and AghaKouchak 2014; Anagnostou et al. 2009; Yong et al. 2015; AghaKouchak et al. 2011; Prakash et al. 2014; Liu and Zipser 2015). For example, Mehran et al. (2014) evaluated the performance of Tropical Rainfall Measuring Mission (TRMM) Multisatellite Precipitation Analysis (TMPA), Precipitation Estimation from Remotely Sensed Information Using Artificial Neural Networks (PERSIANN) and CPC MORPHing technique (CMORPH) for detecting heavy precipitation rates against Stage IV radar observations over the CONUS. They showed that all these precipitation datasets miss a significant volume of rainfall. They concluded that none of the 3-hourly estimates from these products are suitable for detecting extreme events and their detection skills decrease dramatically as the extreme threshold increases. Precipitation Estimation from Remotely Sensed Information using Artificial Neural Networks-Cloud Classification System-Climate Data Record (PERSIANN-CCS-CDR), which provides 0.04° spatial and 3-hourly temporal resolution estimates from 1983 to present, has been explicitly designed to address the need for having a long term dataset with

fine spatiotemporal resolution precipitation estimation which is reliable for extreme event detection.

PERSIANN-CCS-CDR is a new satellite-based precipitation product which was developed based on IR imagery. In general, satellite-based precipitation products have been developed based on utilizing passive microwave (PMW) sensors on low-Earth-orbiting (LEO) satellites and/or visible/IR (VIS/IR) sensors on geosynchronous Earth-orbiting (GEO) satellites (Behrangi et al. 2009; Michaelides et al. 2009; Sorooshian et al. 2000). GEO satellites provide IR imagery with a rapid temporal cycle (30 minutes or less) and high resolution (0.04° × 0.04°) continuously over the globe. Therefore, IR-based products have the advantage of offering precipitation estimates at fine temporal and spatial resolutions over the globe. VIS/IR precipitation estimation algorithms link the IR cloud-top temperature (brightness) to the probability and intensity of rainfall (Kummerow and Giglio 1995). The lower the cloud-top temperature (the brighter clouds), the higher the probability for and the amount of precipitation these algorithms expect (Arkin and Meisner 1987; Adler and Negri 1988). This assumption results in poor performance of these algorithms since there is no direct relationship between rainfall rate and cloud-top temperature. On the other hand, passive microwave (PMW) radiometers offer more direct methods for precipitation estimation as they can probe through most of the clouds and measure precipitation-sized particles (Sun et al. 2018; Joyce et al. 2004). However, PMW sensors are only available from LEO satellites with relatively poor temporal resolution (two observations per day per satellite) (Marzano et al. 2004). In order to take advantage of the strengths that each sensor offers, most precipitation estimation algorithms combine high-frequency information from GEO satellites and sparsely sampled data from LEO satellites. These algorithms mostly serve VIS/IR information as fundamental sources for precipitation estimation and utilize PMW for post processing (Behrangi et al. 2009; Joyce et al. 2004; Nguyen et al. 2020). For example, Precipitation Estimation from Remotely Sensed Information using Artificial Neural Networks (PERSIANN) utilizes IR information as the primary input for the artificial neural network (ANN) model and then employs PMW information for continuously adapting the parameters of the model (Hsu et al. 1997; Sorooshian et al. 2000). PERSIANN provides hourly precipitation estimates at 0.25° spatial resolution from March 2000 to present and is

accessible at a time lag of 2 days at the Center for Hydrometeorology and Remote Sensing (CHRS) data portal (http://chrsdata.eng.uci.edu/) (Nguyen et al. 2018a, 2019).

In order to increase the spatial resolution and decrease the lag time of PERSIANN, Hong et al. (2007) introduced a cloud-patch-based algorithm called PERSIANN-Cloud Classification System (PERSIANN-CCS). This algorithm extracts pre-defined local and regional features from IR satellite imagery under specified temperature thresholds in order to estimate rainfall in four steps. First, IR imagery is separated into distinctive cloud patches based on different temperature thresholds using an incremental temperature threshold algorithm. Then, cloud features including coldness, texture, and geometry are extracted from segmented images. In the third step, a self-organizing feature map (SOFM) approach is utilized in order to classify the cloud patches into well-organized categories. Finally, historical matching is employed to develop a relationship between rain rates and cloud-top temperature and then exponential regression is utilized for rain rate estimation in each pixel (Hong et al. 2007). The PERSIANN-CCS dataset at 0.04° spatial resolution with a lag time of around an hour has been available since January 2003 in hourly time steps at the CHRS data portal (http://chrsdata.eng.uci.edu/).

PERSIANN-Climate Data Record (PERSIANN-CDR) is the next PERSIANN system product which was introduced to provide long-term precipitation records for climate studies (Ashouri et al. 2015). PERSIANN-CDR offers historical records of precipitation estimates dating back to 1983 with 0.25° spatial and daily temporal resolutions and is publicly available through the NOAA National Centers for Environmental Information (NCEI) (https://www.ncdc.noaa.gov/cdr/atmospheric/precipitation-persiann-cdr) and the CHRS Data Portal (http://chrsdata.eng.uci.edu/). PERSIANN-CDR employs infrared imagery data from Gridded satellite infrared data (Gridsat-B1) merged IR and then utilizes the National Centers for Environmental Prediction (NCEP) Stage IV hourly precipitation for training the ANN model. Then, the Global Precipitation Climatology Project (GPCP) monthly 2.5° precipitation data is used for reducing the bias (Sadeghi et al. 2019a). A comprehensive description of the PERSIANN-CDR algorithm can be found in Ashouri et al. (2015).

1.4. PERSIANN-CCS-CDR dataset

Improvement of the PERSIANN systems for precipitation estimation toward higher spatiotemporal resolutions with longer period of records is ongoing at CHRS at the University of California, Irvine. The development of the PERSIANN-CCS-CDR product, which provides precipitation estimates at 0.04° × 0.04° spatial and 3-hourly temporal resolution from 1983 to present, is presented in this paper. PERSIANN-CCS-CDR combines the algorithms that were used in developing the PERSIANN-CCS and PERSIANN-CDR and leverages information from GEO satellites as input data in order to provide a fine spatiotemporal precipitation dataset with a long period of record. In this process, the PERSIANN-CCS algorithm is applied to Gridded satellite (GridSat-B1) and NOAA Climate Prediction Center (CPC-4km) global merged infrared products. Then, the estimates are bias adjusted using the Global Precipitation Climatology Project (GPCP) dataset for the entire period of record. In this study, PERSIANN-CDR, Stage IV and CPC Global Unified Gauge-Based Analysis of Daily Precipitation are used as the reference data for comparison.

1.5. Dissertation Outline

This dissertation is organized as follow: Chapter 2 investigates the effectiveness of applying Convolutional Neural Networks (CNNs) together with the Infrared (IR) and Water Vapor (WV) channels from geostationary satellites for precipitation estimation. The proposed model (PERSIANN-CNN) performances are evaluated during summer 2012 and 2013 over central CONUS at the spatial resolution of 0.08-degree and at an hourly time scale. Chapter 3 explores the effectiveness of adding geographical information (i.e., latitude and longitude) to IR information and the application of a U-Net-based convolutional neural network for improving the accuracy of retrieval algorithms. In Chapter 2, both PERSIANN-SDAE and PERSIANN-CNN models were trained over the central United States and then compared with PERSIANN-CCS over that same region during the summer. However, it is unclear how the models would perform across other regions or seasons where the mechanisms of precipitation may vary. Therefore, the first question to address is: Can a CNN-based model outperform PERSIANN-CCS over the contiguous United States (CONUS)? Secondly, both proposed SDAE and CNN models leverage the water vapor (WV) information in conjunction with IR images; however, PERSIANN-CCS only estimates the rainfall based on IR information. The next question is: Can a CNN-based model outperform the current PERSIANN-CCS using

the same input (IR information)? The last question to investigate is: How can we improve the proposed CNN-based model in Chapter 2 based on the characteristics of rainfall and the features of the CNN architectures? In chapter 3, I answer these questions by exploring the performance of CNN-architectures by adding geographical information as inputs. Then, the performance of the PERSIANN-CNN dataset, which applies U-Net architecture on IR and geographical information (referred to as PERSIANN-CNN) is tested against PERSIANN-CCS at hourly and daily scales during summer and winter over the CONUS. In Chapter 4, a method for constructing PERSIANN-CDR with the new version of GPCP (V2.3) is explored. The newly constructed version of PERSIANN-CDR with GPCP V2.3, called PERSIANN-CDR V2.3, was compared and evaluated with the previous V2.2 version for the period of 2009 to 2013. For comparison, the differences between PERSIANN-CDR V2.3 and the previous version (PERSIANN-CDR V2.2) and also the two latest versions of GPCP (V2.2 and V2.3) at the monthly scale are investigated. The estimation accuracy of the two versions of PERSIANN-CDR is evaluated over land and ocean surfaces using the CPC gauge-based precipitation dataset and the TRMM 3B42 V7 product. Chapter 5 presents the development of PERSIANN-CCS-CDR, which provides accurate estimation of extreme precipitation with fine spatiotemporal resolution (0.04° spatial and 3-hourly temporal resolution) from 1983 to present over the global domain of 60°S to 60°N. Finally, chapter 6 illustrates the application of near-real time and historical precipitation to investigate spatiotemporal variations of heavy precipitation.

CHAPTER TWO:

PERSIANN-CNN: PRECIPITATION ESTIMATION FROM REMOTELY SENSED INFORMATION USING ARTIFICIAL NEURAL NETWORKS - CONVOLUTIONAL NEURAL NETWORKS

The contents of Chapter 2 are published in the Journal of Hydrometeorology.

Citation: Sadeghi, M., Asanjan, A. A., Faridzad, M., Nguyen, P., Hsu, K., Sorooshian, S., & Braithwaite, D. (2019). PERSIANN-CNN: Precipitation estimation from remotely sensed information using artificial neural networks–convolutional neural networks. Journal of Hydrometeorology, 20(12), 2273-2289.

2.1. Abstract

Accurate and timely precipitation estimates are critical for monitoring and forecasting natural disasters such as floods. Despite having high-resolution satellite information, precipitation estimation from remotely sensed data still suffers from methodological limitations. State-of-the-art deep learning algorithms, renowned for their skill in learning accurate patterns within large and complex data sets, appear well-suited to the task of precipitation estimation, given the ample amount of high-resolution satellite data. In this study, the effectiveness of applying Convolutional Neural Networks (CNNs) together with the Infrared (IR) and Water Vapor (WV) channels from geostationary satellites for estimating precipitation rate is explored. The proposed model performances are evaluated during summer 2012 and 2013 over central CONUS at the spatial resolution of 0.08-degree and at an hourly time scale. Precipitation Estimation from Remotely Sensed Information using Artificial Neural Networks (PERSIANN) Cloud Classification System (CCS), which is an operational satellite-based product, and PERSIANN-Stacked Denoising Autoencoder (PERSIANN-SDAE), are employed as baseline models. Results demonstrate that the proposed model (PERSIANN-CNN) provides more accurate rainfall estimates compared to the baseline models at various temporal and spatial scales. Specifically, PERSIANN-CNN outperforms PERSIANN-CCS (and PERSIANN-SDAE) by 54% (and 23%) in the Critical Success Index (CSI), demonstrating the detection skills of the model. Furthermore, the Root Mean Squared Error (RMSE) of the rainfall estimates with respect to the National Centers for Environmental Prediction (NCEP) Stage IV gauge-radar data, for PERSIANN-CNN was lower than that of PERSIANN-CCS (PERSIANN-SDAE) by 37% (14%), showing the estimation accuracy of the proposed model.

2.2. Data and Study Area

2.2.1. Model Inputs and the Observational Data set

NOAA GOES Imagery (IR & WV)

The input data used in this study are IR and WV channels from Geostationary Operational Environmental Satellite (GOES) satellites with wavelengths of 10.7 μm and 6.7 μm, respectively. The WV channel is utilized as a supplementary input to the IR data since previous studies by (Behrangi et al. 2009) have shown the contribution the WV channel can

add for rainfall estimation. Physically, the conversion of water vapor is necessary for precipitation formation (Stohl and James 2004). Previous studies have shown that the WV channel in conjunction with IR can recover a great amount of missing precipitation under warm clouds (Kurino 1997). In this study, both IR and WV channel data from the Geostationary Operational Environmental Satellite (GOES) are processed to an hourly scale with a 0.08-degree (8 km) spatial resolution.

NCEP Stage IV QPE Product

The National Centers for Environmental Prediction (NCEP) Stage IV Quantitative Precipitation Estimation (QPE) is often assumed to be the best long-term precipitation observation over the CONUS due to its extensive quality control procedures and uniform space-time grid (Smalley et al. 2014). This product, hereafter referred to Stage IV, combines the national Weather Surveillance Radar-1988 Doppler (WSR-88D) network of ground radars and surface gauges for precipitation estimation (Lin and Mitchell 2005). For this study, hourly NCEP Stage IV QPE precipitation accumulations at 0.04 degree (4 km) spatial resolution were obtained from the Stage IV QPE distribution website to serve as the ground-truth observations[1]. The original 0.04-degree data set was resampled to 0.08-degree (8 km) spatial resolution to match the resolution of the IR and WV data.

2.2.2. Baseline Models

PERSIANN-CCS

PERSIANN-CCS is a near real-time precipitation estimation at 0.04-degree spatial resolution and half-hourly temporal resolution and has become popular as an operational product. The PERSIANN-CCS algorithm employs IR satellite imagery to extract local and regional cloud features to estimate rainfall (Hong et al. 2004) in 4 steps: 1) cloud segmentation: Separates IR imagery into distinctive cloud patches using an incremental temperature threshold algorithm, 2) feature extraction: Extracts local and regional cloud patch features including coldness, texture, and geometry, 3) cloud classification: cluster cloud patches into well-organized subgroups using self-organizing feature maps (SOFMS) based on cloud patch

[1] http://www.emc.ncep.noaa.gov/mmb/ylin/pcpanl/stage4/

features, 4) rainfall mapping: uses cloud-top temperature and rainfall relationships for each classified cloud cluster. In step 4, the relationship between the cloud-top temperature and the rain rate is obtained for every cluster by applying probability matching method (PMM) and an exponential curve fitting. One of the main advantages of this algorithm is its simplicity and its ability to capture extreme precipitation events. For this study, PERSIANN-CCS[1] was resampled to a 0.08 degree spatial resolution and an hourly temporal resolution for the purpose of comparison.

PERSIANN-SDAE

Developed by Tao et al. (2018) the PERSIANN-SDAE algorithm uses IR and WV data in a fully connected deep neural network model to detect and estimate the rainfall rate. The SDAE technique, introduced by (Modarres and da Silva 2007; Shay-El et al. 1999; Sadeghi et al. 2019b), is an unsupervised pre-training method to extract useful information from the input data and is particularly useful for image recognition tasks. The PERSIANN-SDAE algorithm applies a three layer fully connected neural network employing a greedy layer-wise pre-training based on stacked denoising autoencoders utilizing IR and WV channels. Kullback-Leibler (KL) divergence and Mean Square Error (MSE) were used as the loss functions in the PERSIANN-SDAE algorithm. These objective functions help decrease estimation error while preserving the distribution of the rainfall. Another advantage of the SDAE algorithm is that it can automatically extract useful features from the input data. This results in a complicated functional mapping between the raw input data and the observational data. On the other hand, traditional neural networks like PERSIANN-CCS use manually designed features for data extraction Tao et al. (2016), which does not efficiently utilize the neighborhood pixels' information for precipitation estimation of each pixel .study, we utilize the same data set for PERSIANN-SDAE that Tao et al. (2016) presented.

2.2.3. Study area

The study area of this research is the central United States between the latitudes 30° - 45° N and longitudes 90° - 105°W (Fig 2.1). This region has been chosen primarily because of its predominant convective precipitation mechanism that leads to intense storms during

[1] https://chrsdata.eng.uci.edu/

summer time. As a result, many satellite-based precipitation retrieval algorithms experience challenges in detection and estimation of rainfall in the region (Houze Jr 2012). Another reason for choosing this study area is the availability of high-quality radar data which allows for better training and more accurate verification of the models.

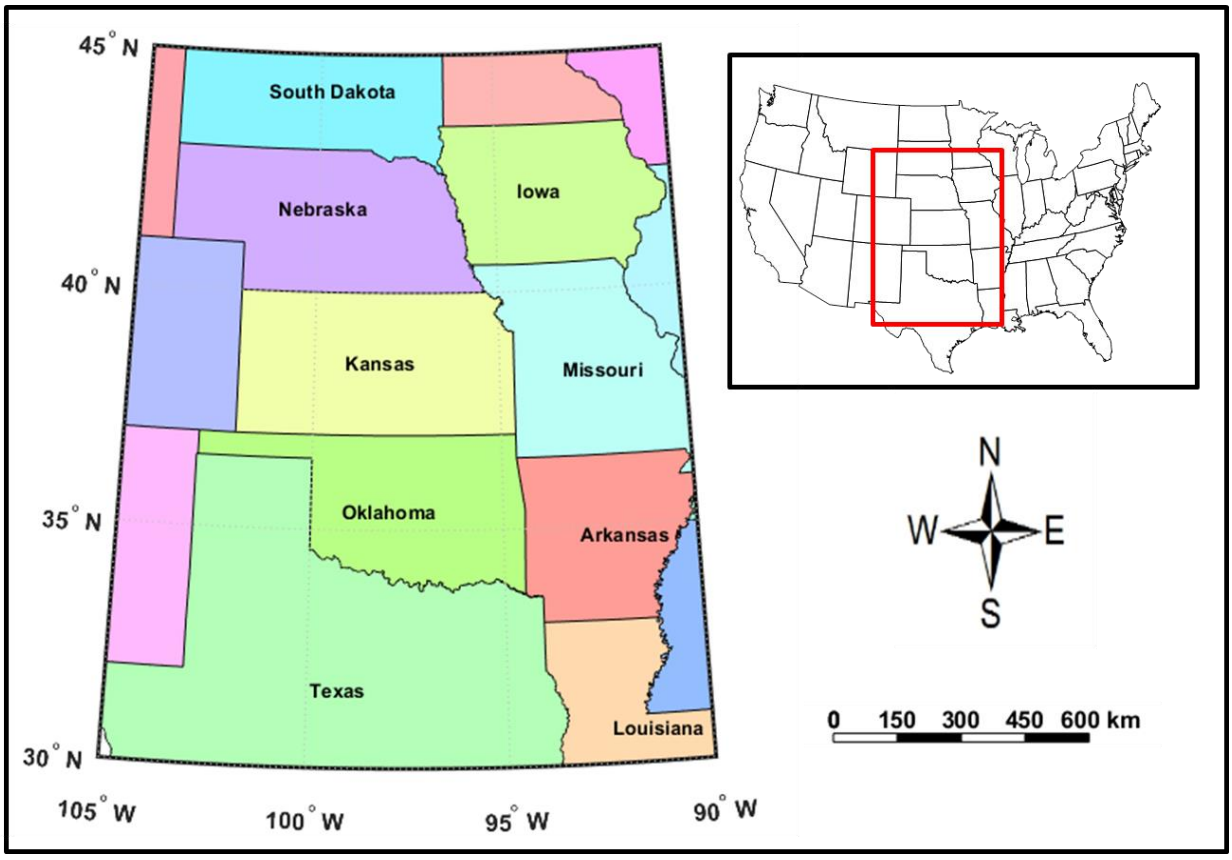

Figure 2.1 Map of the study region in the central United States

2.3. Methodology

2.3.1. CNN architecture

The CNN is one of the most widely-used deep learning algorithms, having recently gained much interest in the field of image processing (Zhu et al. 2017). The CNN is superior to other DNN algorithms due to its ability to preserve the spatial information by maintaining the interconnection between pixels (Rezaee et al. 2018). The CNN is one type of feed-forward neural network in which an input passes through one or multiple layers of "neurons". Each neuron represents a linear combination of inputs that passes through a typically nonlinear function, called the activation layer, and then passes to the next layer. The model can then be

trained with a backpropagation algorithm. The goal of training is to update sets of weight matrices and bias vectors to minimize the loss function, i.e. the distance between the estimation and observation. A CNN network is typically constructed with one or more convolution layers and pooling layers (Krizhevsky et al. 2012; Shen 2018). In convolution layers, outputs (feature maps) of the previous layer are convolved by sliding convolution filters, which have learnable weights, to extract hidden features from the input. Fig 2.2a represents an example of applying a two-dimensional convolutional filter (Conv 2D) to an input matrix. Each element of the output is obtained from summing the element-wise product of the input matrix and the convolutional filter. The output of the convolution operator is added by a separately trained bias vector. The result is plugged into an activation function to construct the feature map of the next layer (Yang et al. 2015). A Convolution layer is often paired with a pooling layer (also called sub-sampling layer). In the pooling layer, the spatial resolution of feature maps is reduced to decrease the number of parameters; thus decreasing the computation cost and avoiding overfitting. There are many methods for subsampling, such as average-pooling and max-pooling. In an average-pooling layer, elements of the input are averaged within a window to form the output, while the maximum element of that window is obtained as the output in a max pooling layer (Fig 2.2b). For this study we utilized max pooling layers since they can further reduce the scale of the input and greatly decrease the model's dimensionality to avoid overfitting.

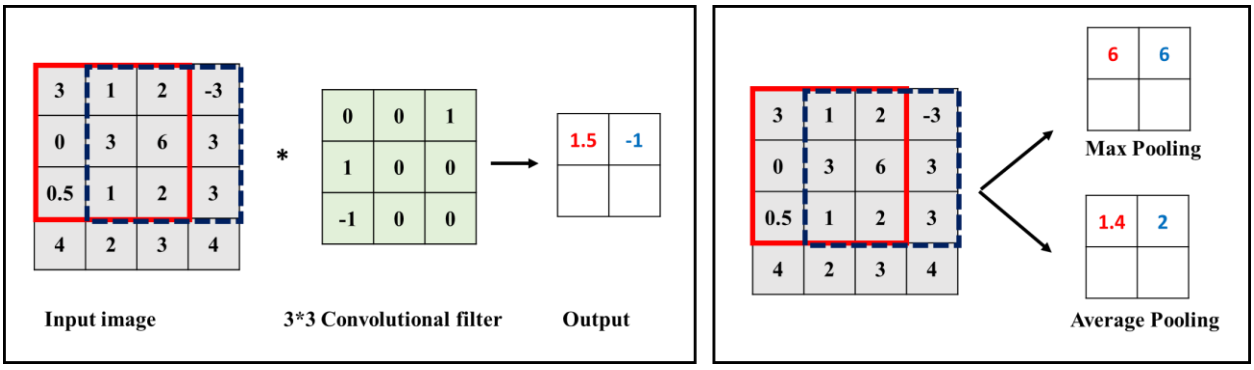

Figure 2.2 a) An Example of a 3*3 convolutional filter applied to a 4*4 matrix; b) An Example of 3*3 max pooling / average pooling filter applied to a 4*4 matrix

2.3.2. Model Setup

Overview of the layers

The architecture of the proposed CNN model with details of input shape, filter size, stride size and output is shown in Fig 2.3. The inputs are two 32×32 matrices containing the IR and WV channels of GOES-West satellite. The inputs are separately convolved in order to learn information from each channel individually. Then, we utilize a concatenation function to merge the two map features. The output can be up-sampled from low resolution to high resolution in two steps using a two-dimensional convolutional transpose function (2D ConvTranspose). Then the final feature maps were derived after convolving the output of the previous layers for two times. The output of the model is the rain rate with the same spatial and temporal resolutions as the input data. Furthermore, in all steps we utilize a Rectified Linear Unit (ReLU) activation function for nonlinearity. The ReLU function is f(x)=max (0,x). This function can be quickly computed since it does not have any exponential or multiplication function and assigned zero for negative elements. Furthermore, computing the gradient of the ReLU function is simple and can be either 0 or 1 based on the sign of the element.

Parameter Tuning

The inputs (IR and WV) and target (Stage IV) data sets are divided into the training, validation, and test periods. Summer 2012 (June, July, and August) and the first month of summer 2013 (June) were used for training and July 2013 was used for validation. The training and validation data set are utilized to optimize the model parameters and also prevent overfitting. August 2013 was kept unused during the training phase and was used for testing the developed model. Various combinations of the hyperparameters were tested during the training phase of the CNN model to optimize the 869,665 learnable parameters of the proposed model. Hyperparameters are the variables which determine the structure of a DNN (i.e. layer type, neuron size) and the variables which determine how the CNN network should be trained (i.e. learning rate) (Erhan et al. 2010). MSE was defined as the loss function to minimize during the training and validation phases. The initial values of the parameters are randomly selected from a standard normal distribution. Then, the parameters are trained using the gradient descent method in order to minimize the errors at each epoch.

Also, an early stopping criterion was introduced which halted the training if the objective function value did not improve after 10 epochs. The lowest MSE in both training and validation periods are achieved by defining the model specific hyperparameters leading to the configuration shown in Fig 2.3. Furthermore, a learning rate of 0.01, a minibatch size of 32, and an epoch size of 100 were determined through the minimizing processes.

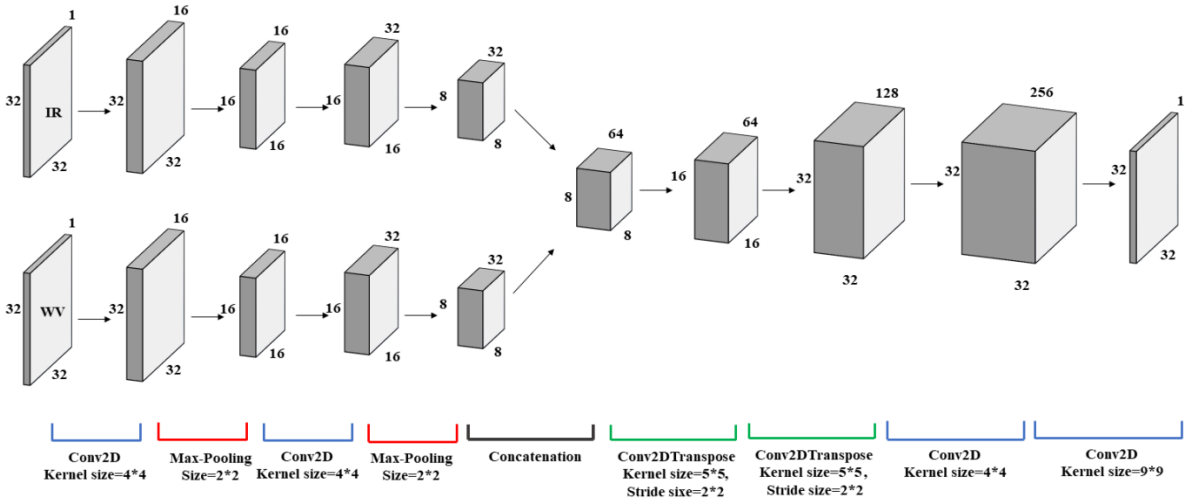

Figure 2.3 schematic of the proposed CNN model.

2.3.3. Performance Measurements

Categorical Evaluation Statistics

Categorical evaluation statistics are used to evaluate the abilities of the models in detecting rain/no-rain pixels. These statistical indices include the probability of detection (POD), false alarm ratio (FAR), and the critical success index (CSI). The mathematical formulations for each of these indices are given below:

$$\mathrm{POD} = \frac{\mathrm{TP}}{\mathrm{TP+MS}} \quad \text{(Range: from 0 to 1; desirable value: 1)}$$

$$\mathrm{FAR} = \frac{\mathrm{FP}}{\mathrm{TP+MS}} \text{ (Range: from 0 to 1; desirable value: 0)}$$

$$\mathrm{CSI} = \frac{\mathrm{TP}}{\mathrm{TP+FP+MS}} \quad \text{(Range: from 0 to 1; desirable value: 1)}$$

Where:

TP: Number of pixels correctly classified as rain (true positive events)

FP: Number of pixels incorrectly classified as rain (false positive events)

MS: Number of pixels incorrectly classified as no rain (missing events)

Continuous Evaluation Statistics

Continuous indices are employed to evaluate the skill of each algorithm in estimating rainfall intensity. Statistics in this category include: Root Mean Squared Error (RMSE), Correlation Coefficient (CC), and Mean Absolute Error (MAE), which are calculated by the following equations:

$$\mathrm{RMSE} = \frac{1}{\mathrm{n}}\sqrt{\sum_{\mathrm{i}=1}^{\mathrm{n}}(Sim_i - Obs_i)^2}$$

$$\mathrm{CC} = \frac{\frac{1}{n}\sum_{i=1}^{n}(Sim_i - \overline{Sim_\iota})(Obs_i - \overline{Obs_\iota})}{\sigma_{Sim}\,\sigma_{obs}}$$

$$\mathrm{MAE} = \frac{1}{\mathrm{n}}\sum_{\mathrm{i}=1}^{\mathrm{n}}|Sim_i - Obs_i|$$

Where:

Sim: Simulation (PERSIANN-CCS, PERSIANN-SDAE, PERSIANN-CNN)

Obs: Ground reference observation (Stage IV)

2.4. Results and Discussion

2.4.1. Performance Evaluation at Hourly Scale

An extreme storm that occurred on the 3rd of August 2013 over the study area is examined to compare the performance of PERSIANN-CNN against PERSIANN-CCS and PERSIANN-SDAE. On Aug. 3rd, 2013 at 11:00 AM UTC, two separate cloud patches can be detected using the IR (Fig 2.4a) and WV channels (Fig 2.4b) which show intense rainfalls mostly near the central areas of the larger patch (Fig 2.4c). As shown in Fig 2.4e, PERSIANN-CNN provides a more realistic representation of the extent and the pattern of the rainfall patches (Fig 2.4c) as compared to PERSIANN-CCS (Fig 2.4f) and PERSIANN-SDAE (Fig 2.4d). Both PERSIANN-SDAE and PERSIANN-CCS falsely detect precipitation occurrence over the majority of the larger cloud patch where the cloud temperature is relatively lower. Also, PERSIANN-CNN is more accurate than the other two models in identifying the location of the rainfall patches. This can be observed by looking at the location of the smaller rainfall patch, where the PERSIANN-SDAE estimates seems to have a northward shift. PERSIANN-CNN gives more accurate intensity estimates compared with PERSIANN-SDAE and PERSIANN-CCS (Fig 2.4d and Fig 2.4f), which underestimate and overestimate, respectively. Overall, Fig 2.4 demonstrates that PERSIANN-CNN is capable of providing more accurate estimates of the shape, location, and intensity of precipitation in comparison to PERSIANN-CCS and PERSIANN-SDAE.

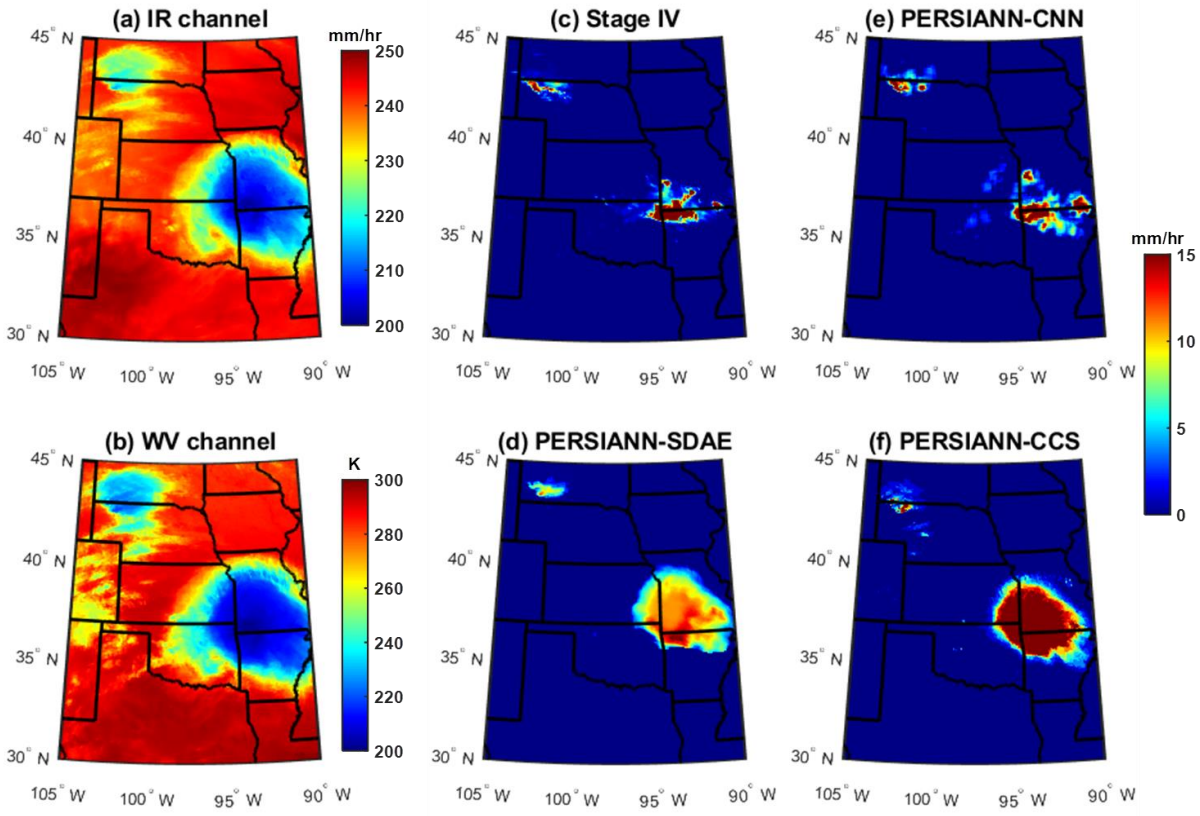

Figure 2.4 Case study I: Maps of cloud-top temperature (in °K) from (a) IR imagery, (b) WV imagery, and precipitation rate (in mm/hr) from (c) Stage IV radar observation (d) PERSIANN-SDAE, (e) PERSIANN-CNN, and (f) PERSIANN-CCS for Aug. 3, 2013 11:00 UTC.

Similar maps for another case study (Aug. 16, 2013 9:00 UTC) also demonstrate the superior performance of PERSIANN-CNN in detecting the precipitation spatial pattern and the magnitude (Fig 2.5).These observations can be justified based on the models' structures. PERSIANN-SDAE employs a pixel-based approach that does not leverage the neighborhood information efficiently. In specific, SDAE links all of the pixels of IR and WV to all of the hidden neurons in the autoencoder algorithm. This architecture known as a fully-connected network makes it hard to efficiently and effectively learn the structure of the rainy patches and thus estimate the correct shapes and rainfall rates. Due to the higher complexity level of fully-connected networks for learning spatially correlated data (i.e. images), they tend to restrict the learning to one-on-one pixels in most cases, meaning that they train the parameters of each pixel separately. In addition, in most cases due to the fuzzy and patchy

nature of rainfall spatial structure, the SDAE model cannot effectively link neighborhood information. Therefore, SDAE learns an indirect relationship between the cloud temperature and the rain-rate, resulting in colder clouds showing more intense precipitation and in larger patches of rainfall compared to ground-truth radar observations. On the other hand, PERSIANN-CCS is a patch-based approach which classifies each rainfall event based on its cold cloud patches and the patch features; however, in the last step of the algorithm which is the rainfall mapping step (i.e., nonlinear regression), a fully-connected layer is assigned to find the relationship of infrared brightness temperature and rainfall rates. The same deficiencies of the above-explained fully connected for SDAE apply to the rainfall mapping step of PERSIANN-CCS also resulting in estimating larger patches of rainfall compared to ground-truth radar observations.

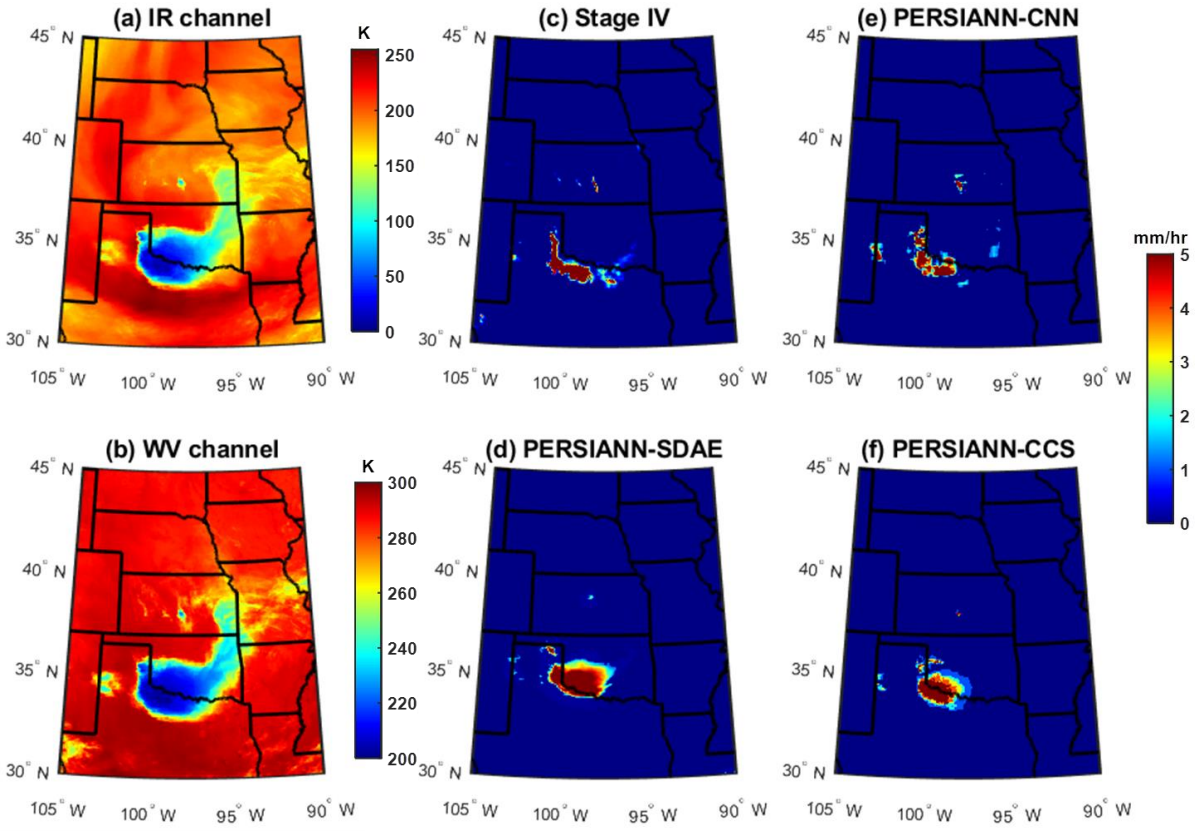

Figure 2.5 Case study II: Maps of cloud-top temperature (in °K) from (a) IR imagery, (b) WV imagery, and precipitation rate (in mm/hr) from (c) Stage IV, (d) PERSIANN-SDAE, (e) PERSIANN-CNN, and (f) PERSIANN-CCS snapshots for Aug. 16, 2013 9:00 UTC.

Table 1 summarizes the performance of each model in terms of categorical (POD, FAR, and CSI) and continuous (MAE, RMSE, and CC) metrics throughout the verification period of August 2013. All verification metrics were computed for each pixel and at hourly time scale over the study area for the entire verification period. In addition, Figure 2.6 presents the spatial distribution of the mentioned metrics of the PERSIANN-CNN and the two baseline models for the verification period. In general, PERSIANN-CNN shows substantial improvement compared to PERSIANN-CCS and PERSIANN-SDAE according to the performance metrics. Compared to the baseline models, PERSIANN-CNN shows a significant improvement in POD and CSI, especially in the central and western regions of the study area. For FAR, the performance of the PERSIANN-CNN and PERSIANN-SDAE are almost the same and obviously better than PERSIANN-CCS, which is also obvious from the FAR values presented in Table 2.1. Furthermore, PERSIANN-CNN calculates more accurate rainfall intensity estimates as evident by its lower MAE, RMSE, and higher CORR values during the verification period (Table 2.1 and Fig 2.6). As shown in the figures, PERSIANN-CNN performance metrics are more homogeneous compared to PERSIANN-CCS and PERSIANN-SDAE across space over the whole study area. This spatial homogeneity is more noticeable in the spatial pattern of FAR where PERSIANN-CNN performs almost the same for the entire study area while PERSIANN-SDAE performs well in some areas and poor for other parts. This shows the capability of the PERSIANN-CNN to generalize features across spatial domains; conversely, PERSIANN-CCS and PERSIANN-SDAE show diverse performances metrics across the case-study area, showing their localized features. The localized performance of PERSIANN-SDAE is partially due to selecting a small and fixed portion of study area for the training samples of the model (Tao et al. 2018).

Table 2.1 Summary of hourly precipitation estimation performance for discussed models over the CONUS

	POD	**FAR**	**CSI**	**MAE (mm)**	**RMSE (mm/hr)**	**CC**
PERSIANN-CCS	0.39	0.66	0.24	0.19	1.40	0.22

PERSIANN-SDAE	0.45	**0.52**	0.30	0.14	1.02	0.28
PERSIANN-CNN	**0.67**	0.56	**0.37**	**0.12**	**0.88**	**0.41**

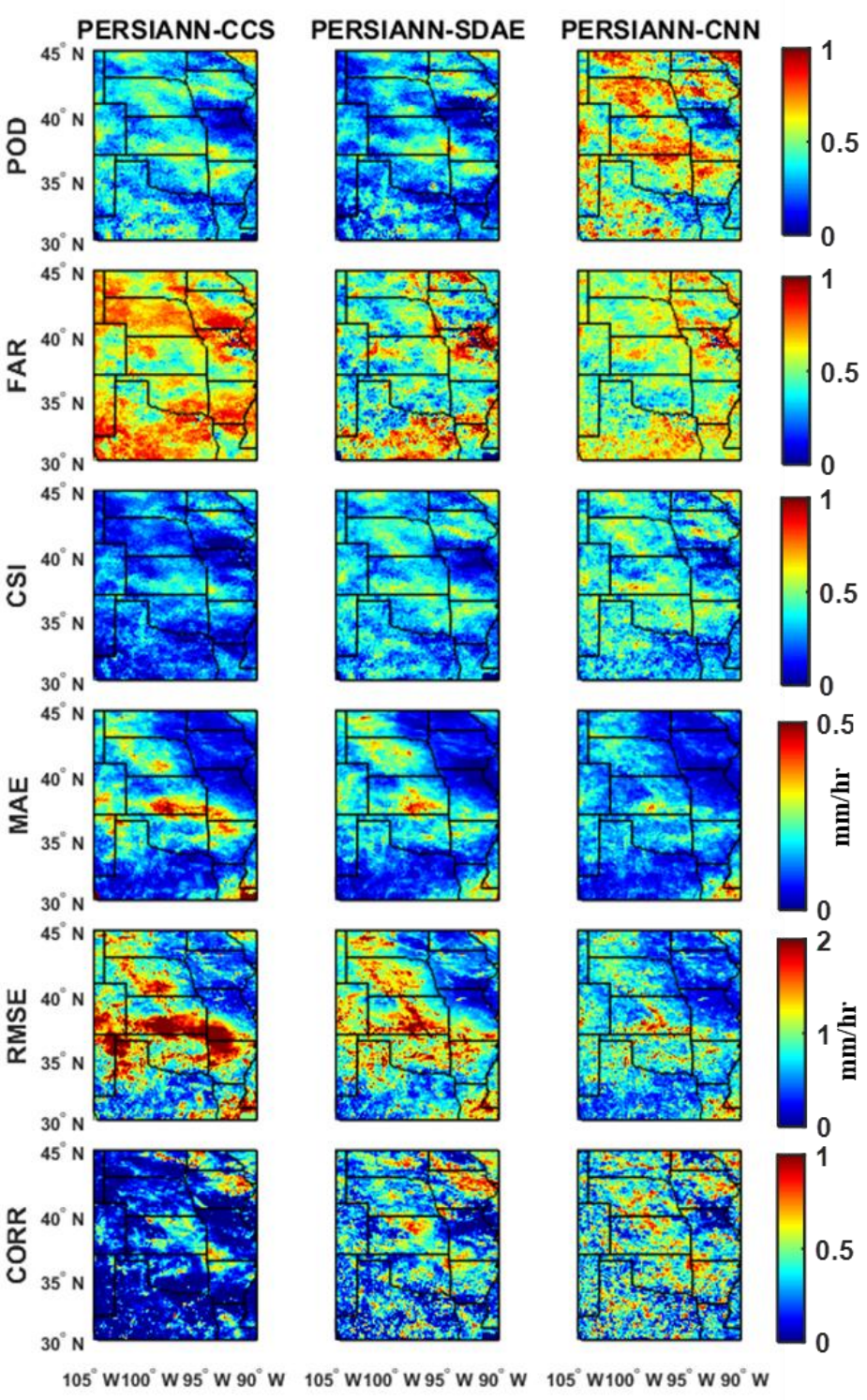

Figure 2.6 categorical (POD, FAR, CSI) and continuous (MAE, RMSE, CORR) metrics of the PERSIANN-CCS, PERSIANN-SDAE, and PERSIANN-CNN over the entire verification period.

2.4.2. Performance Evaluation at Daily Scale

The proposed model, PERSIANN-CNN, was also evaluated and compared with the baseline models at a daily time scale. To do so, hourly estimates were accumulated to daily values for the extreme event that occurred from August 3 to 10, 2013. According to the National Weather Service, heavy rainfalls were observed in various locations across the Missouri, southeast Kansas, and Arkansas from August 3rd through August 10th, 2013[1]. Rainfall rates of around 5 mm per hour are reported across these areas for several days, receiving between 20 to 25 mm accumulated rain in a short window of time in some locations. This extreme amount of precipitation resulted in flash flooding causing 3 deaths with many water rescues and hundreds of flooded roadways in those areas. Specifically, on August 3rd, an extreme heavy rainfall occurred in Missouri, Kansas, and Arkansas with an intensity of approximately 5 mm per hour, lasting almost 12 hours from 4:00 to 15:00 UTC[2]. Some areas received between 40-60 mm of precipitation in a short period of time. This considerable amount of rainfall triggered dangerous flash floods, with lots of property damages.

Figures 2.7 and 2.8 present the daily values for the extreme precipitation event that occurred on Aug 3 and Aug 10, 2013, respectively. In both cases PERSIANN-CNN provides a more accurate detection of the rainfall pattern compared to the baseline models. Furthermore, the spatial variation of the PERSIANN-CNN estimation for this day is more similar to that of the radar observations than the PERSIANN-CCS and PERSIANN-SDAE estimations. For the extreme event on August 3rd, both PERSIANN-CCS and PERSIANN-SDAE overestimate the rain rate and assign heavy rainfall to larger areas, while PERSIANN-CNN provides a more realistic representation of heavy rainfall areas (Fig 2.7). For the August 10th event, the peak of heavy extreme rainfall can be observed mostly at the northern part of Arkansas State (Fig 2.8). PERSIANN-CCS captures both the spatial pattern and intensity of the rainfall fairly well. On the other hand, PERSIANN-CCS and PERSIANN-SDAE underestimate the rain rate. In addition, a northward shifting can be seen in PERSIANN-SDAE's estimates.

[1] https://www.weather.gov/sgf/events_2013aug3
[2] https://www.weather.gov/ict/event_08042013

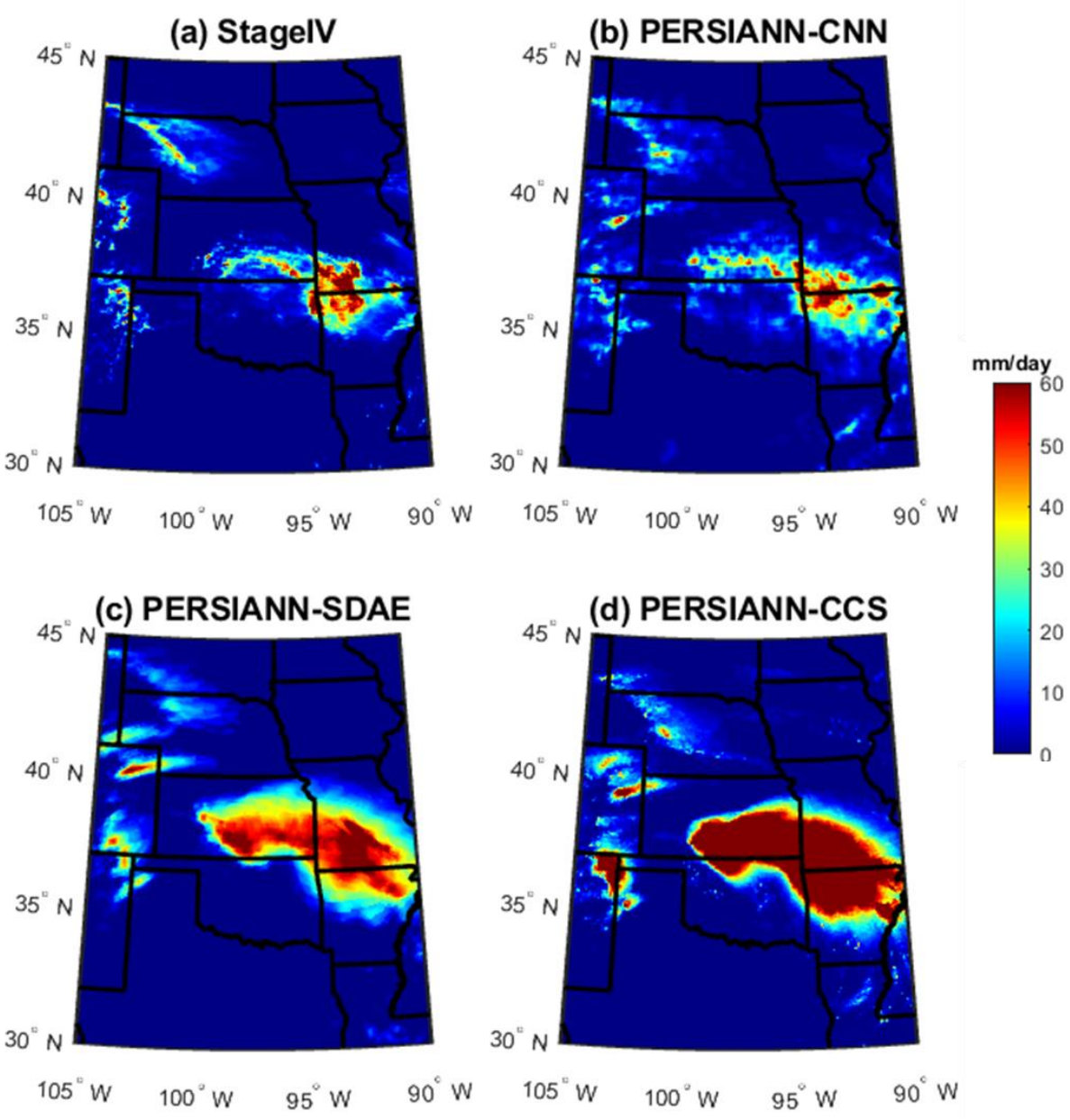

Figure 2.7 Comparison of daily rainfall from radar, PERSIANN-CNN, PERSIANN-SDAE, PERSIANN CCS estimates at 0.08° for Aug 3, 2013.

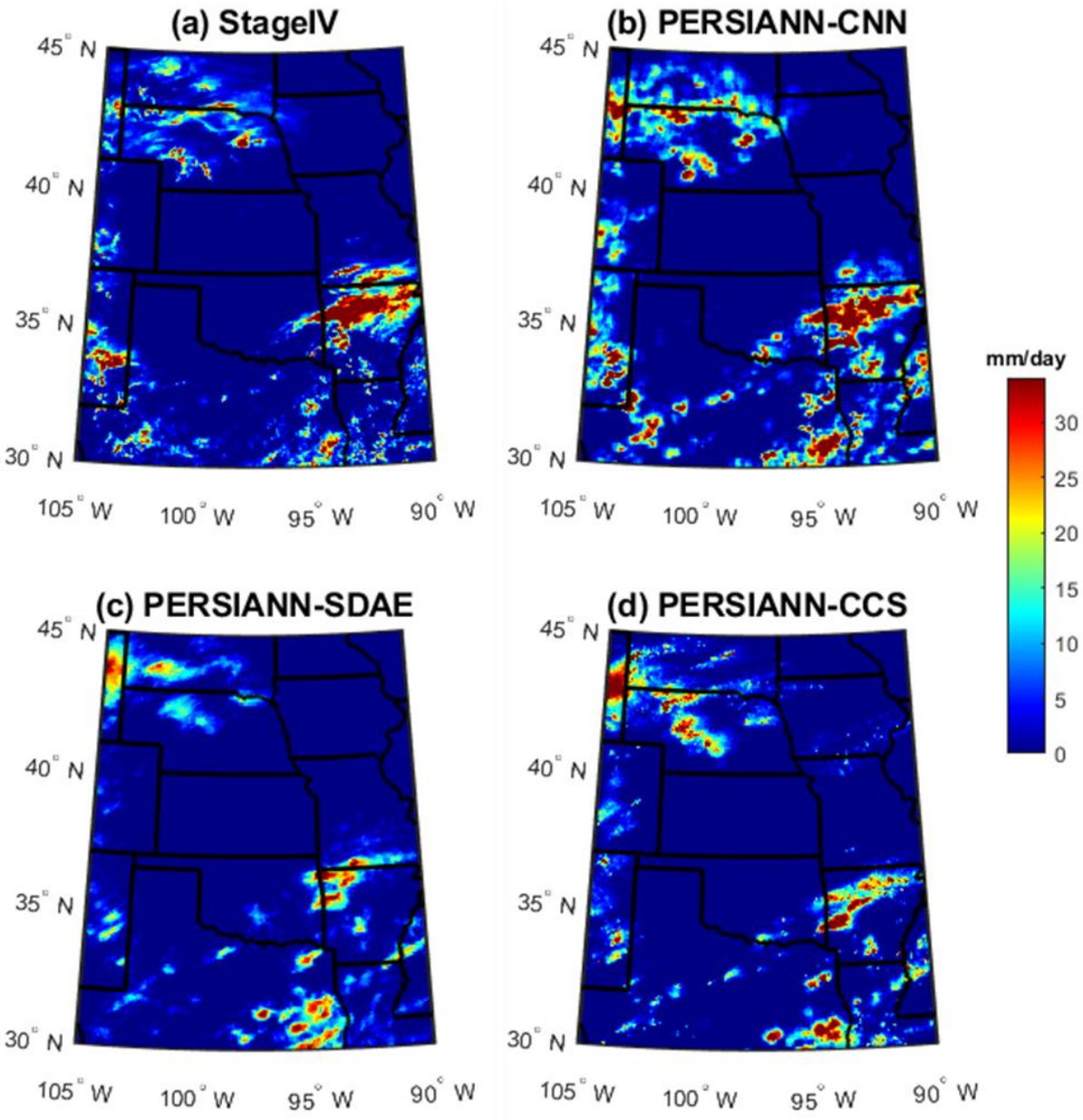

Figure 2.8 Comparison of daily rainfall from radar, PERSIANN-CNN, PERSIANN-SDAE, PERSIANN CCS estimates at 0.08° for Aug 10, 2013.

These two daily case studies emphasize the superior of the CNN-based model compared to the baseline models in terms of accurately estimating the rainfall distribution. Similar to the hourly performance, PERSIANN-CNN estimates the spatial pattern and volumetric of the rainfall more accurately than the baseline models due to its efficient structure. In addition, although PERSIANN-SDAE uses KL divergence, which was utilized for preserving the rainfall distribution, along with MSE as the loss functions, PERSIANN-CNN can perform better only

by applying the MSE loss function in the training process. This indicates that CNN-based models can effectively learn features for preserving the spatial and volumetric distribution of precipitation during the training process without needing to add some other terms to the loss function.

Figure 2.9 demonstrates how the proposed model and the baseline models perform in detecting and estimating the rainfall intensity throughout the different evolution stages of the intense storm that occurred over latitude 34 –38 N and longitude 90 –100W on August 3rd, 2013. Time series plots for the hourly rainfall estimates by the radar observations, PERSIANN-CNN, PERSIANN-CCS, and PERSIANN-SDAE are shown in Fig 2.9a. PERSIANN-CCS and PERSIANN-SDAE overestimate the rainfall for the entire event. However, PERSIANN-CNN's estimates correspond well with the radar observations although there is a slight overestimation and underestimation before and after 11:00 UTC, respectively. The time-series plot of the CC (Fig 2.9b) reveals that PERSIANN-CNN's estimates have higher correlation with Stage IV radar observations during the event compared to PERSIANN-CCS and PERSIANN-SDAE. PERSIANN-CCS and PERSIANN-SDAE demonstrate positive bias ratios with maximums of approximately 10mm/hr and 4mm/hr, respectively (Fig 2.9c), However, the bias ratio for PERSIANN-CNN (approximately 1 mm/hr) is noticeably less than that of the baseline models. For detection skill (Fig 2.9d), all of the models perform more or less the same, each outperforming the other two models at some stages of the storm's evolution.

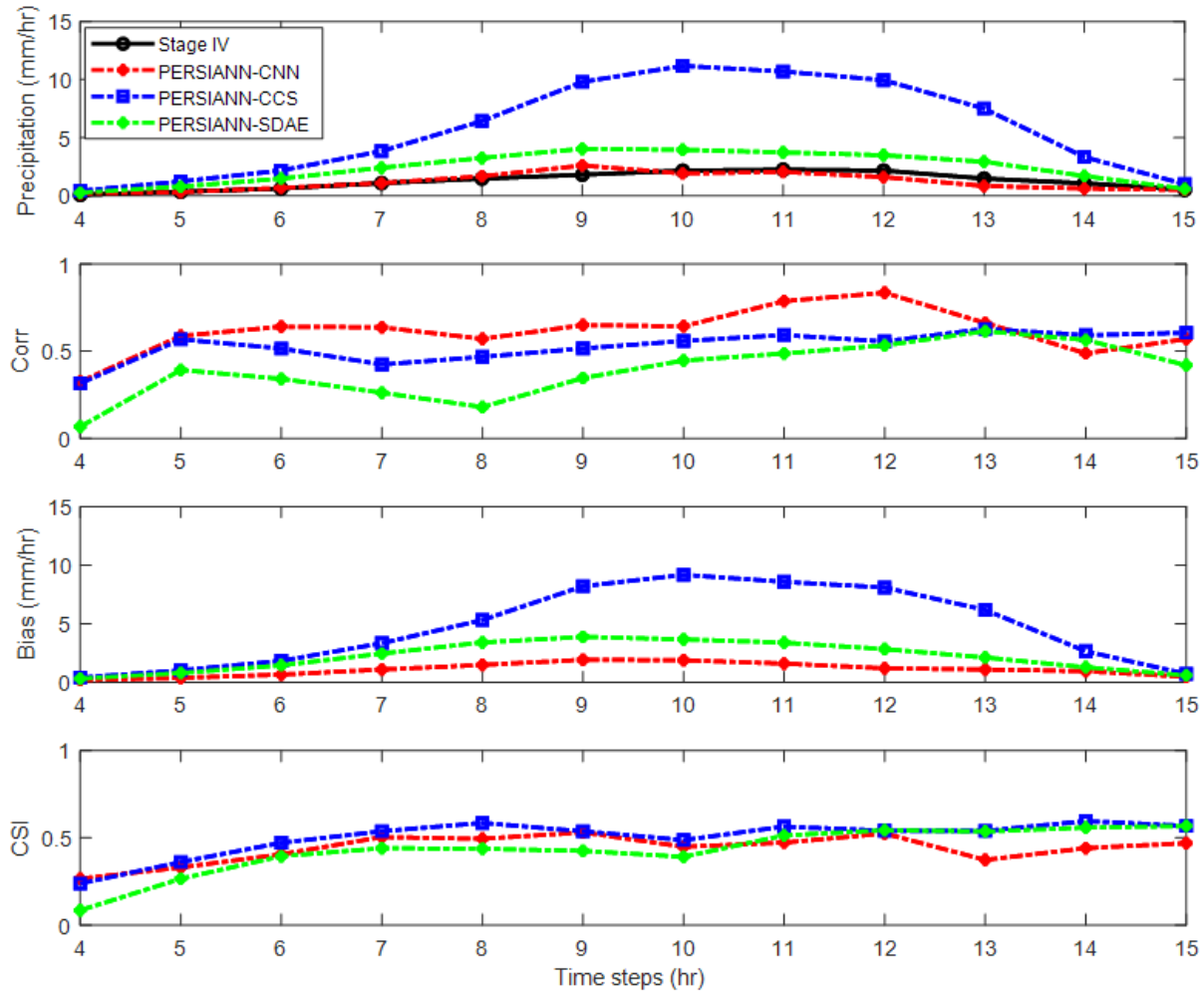

Figure 2.9 Time series plots of (a) hourly rainfall estimates, (b) correlation coefficient, (c) bias (mm/hr), and (d) CSI derived from Stage IV radar observation, PERSIANN-CCS, PERSIANN-SDAE, and PERSIANN-CNN throughout the evolution of the storm event on Aug. 3rd

To explore the daily performance of PERSIANN-CNN against PERSIANN-CCS and PERSIANN-SDAE at various spatial resolutions, scatterplots of their daily precipitation estimation versus the radar observations for August 3rd, 2013 are presented (Figure 2.10). These figures demonstrate the pixel-by-pixel association between the satellite-based estimates and the radar observations for various spatial resolutions and at daily time scale. As shown, during the described extreme event on Aug 3rd, 2013, both PERSIANN-CNN and PERSIANN-CCS show a high correlation (0.75) with the radar observations at 0.08-degree spatial

resolution. However, RMSE and MAE for PERSIANN-CCS are relatively higher than for PERSIANN-CNN and PERSIANN-SDAE. Furthermore, it can be seen that PERSIANN-CCS tends to overestimate intense precipitation in all spatial resolutions, while PERSIANN-SDAE and PERSIANN-CNN tend to underestimate rain rates at both 0.08 and 0.16-degree resolution, but underestimation of heavy precipitation is improved as the resolution decreases to 0.25 and 0.5 degrees.

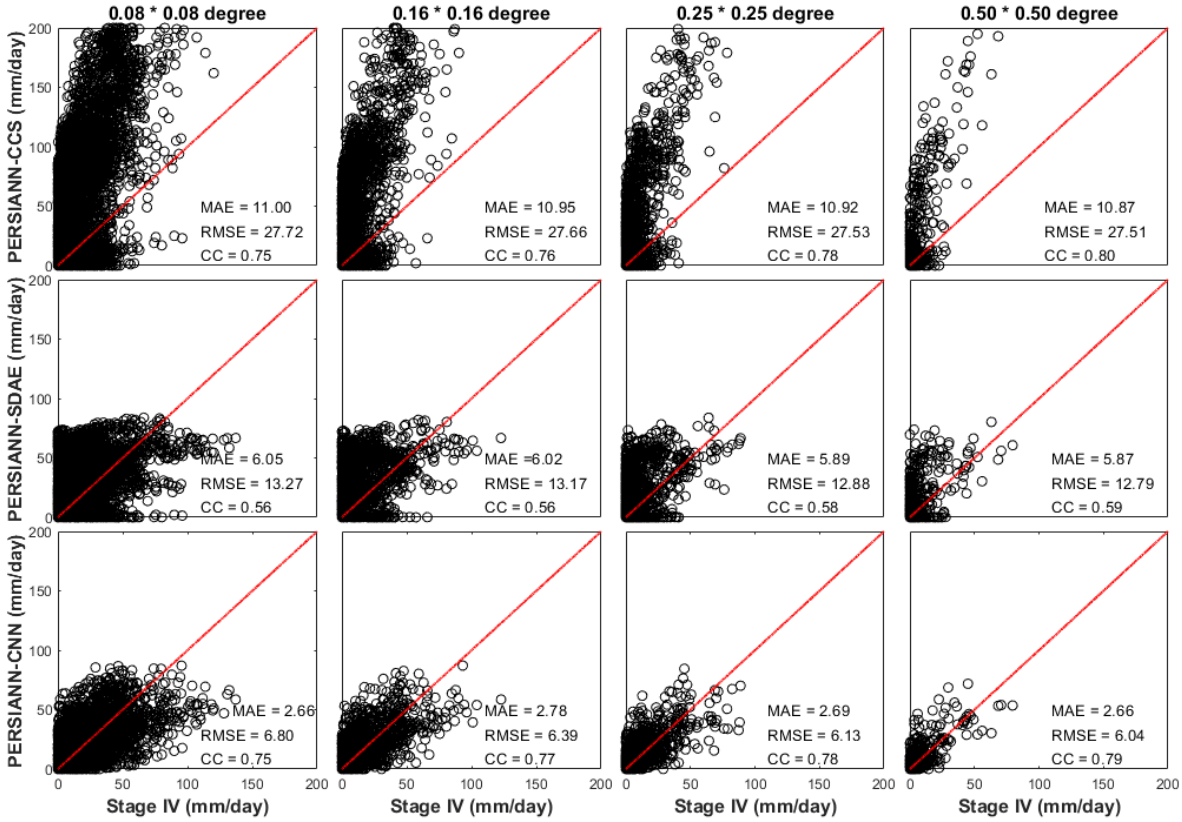

Figure 2.10 Scatterplots of radar measurements vs PERSIANN-CCS, PERSIANN-SDAE, and PERSIANN-CNN: daily rainfall estimation at four spatial scales for the study area on Aug. 3rd, 2013.

2.5. Conclusions

In this study, the application of Convolutional Neural Networks (CNNs) in detecting and estimating precipitation from bispectral satellite imagery (Infrared (IR) and Water Vapor (WV) channels) was explored. A case study over the central United States was conducted to

assess the effectiveness of the presented model at 0.08-degree spatial for both hourly and daily temporal resolution. The proposed model was evaluated against Stage IV radar observations and two existing satellite data sets, PERSIANN-CCS and PERSIANN-SDAE.

Model evaluation procedures at hourly and daily scales showed that PERSIANN-CNN outperforms PERSIANN-CCS and PERSIANN-SDAE in capturing the extent and shape of the rainfall patches by providing a more realistic representation of the precipitation pattern. Model evaluation during the verification period showed that the proposed model performs better than the baseline models in rainfall detection. In terms of POD and CSI, PERSIANN-CNN outperformed PERSIANN-CCS (PERSIANN-SDAE) by 72% (49%) and 54% (23%), respectively. In terms of FAR, PERSIANN-CNN performed better than PERSIANN-SDAE by 12%; however, it performed poorer than PERSIANN-CCS by 10 %. Despite the lower performance of PERSIANN-CNN for FAR compared to PERSIANN-SDAE, PERSIANN-CNN has a more homogeneous and consistent performance for the various evaluation metrics, especially FAR. Additionally, the proposed model had the best overall performance in estimation accuracy over the verification period. For RMSE and MAE, PERSIANN-CNN was more accurate than PERSIANN-CCS (PERSIANN-SDAE) by 37 % (14%) and 8 % (74 %) respectively.

To assess the performance of the models in estimating extreme precipitation, a storm event that affected the central United States in August 2013 was selected. Results indicate that PERSIANN-CNN can capture the spatial shape and peak values of rainfalls more precisely than the baseline models according to the RMSE and MAE indices. Furthermore, rain rate time series demonstrated better overall performance by PERSIANN-CNN. Specifically, the proposed model gave the closest approximations to Stage IV radar for the hourly rainfall, as well as the lowest bias values across the hourly time steps. Finally, a pixel-by-pixel performance evaluation of the PERSIANN-CNN and baseline models with respect to the radar observations was implemented at various spatial resolutions (0.08, 0.16, 0.25, and 0.5 degrees). Results of this analysis demonstrated that PERSIANN-CNN and PERSIANN-CCS show higher correlation (0.75) with the radar observations at 0.08-degree spatial resolution compared to PERSIANN-SDAE. However, RMSE and MAE of PERSIANN-CCS are relatively higher than PERSIANN-CNN and PERSIANN-SDAE. In addition, PERSIANN-CCS

overestimates the rain rate for all spatial resolutions, while PERSIANN-CNN and PERSIANN-SDAE tended to underestimate very intense precipitation at a high spatial resolution; however, their underestimations of extreme precipitation were improved as the spatial resolution decreased.

Expanding on the research presented here, researchers at CHRS will implement the framework to a larger spatial extent with longer verification periods to investigate the stability of the model. The presented model's skill in capturing meaningful IR features can leverage PMW information to better describe the precipitation phenomenon. We are currently extending the proposed model to provide near real-time global precipitation estimation using PMW information as observation for training the model. In addition, NOAA's latest GOES-R Series satellites will provide data at higher temporal and spatial resolutions for use in the model framework.

CHAPTER THREE:

IMPROVING NEAR REAL-TIME PRECIPITATION ESTIMATION USING A U-NET CONVOLUTIONAL NEURAL NETWORK AND GEOGRAPHICAL INFORMATION

The contents of Chapter 3 are published in the Journal of Environmental Modelling & Software.

Citation: Sadeghi, M., Nguyen, P., Hsu, K., & Sorooshian, S. (2020). Improving near real-time precipitation estimation using a U-Net convolutional neural network and geographical information. Environmental Modelling & Software, 134, 104856.

3.1. Abstract

Reliable near real-time precipitation estimates are essential for monitoring and managing of natural disasters such as floods. Quality of inputs and capability of the retrieval algorithm are two important aspects for developing satellite-based precipitation datasets. Most retrieval algorithms utilize infrared (IR) information as their input due to its fine spatiotemporal resolution and near-instantaneous availability. However, their sole reliance on IR information limits their capability to learn different mechanisms of precipitation during training, resulting in less accurate estimates. Moreover, recent advances in the field of machine learning offer attractive opportunities to improve the precipitation retrieval algorithms. This study investigates the effectiveness of adding geographical information (i.e. latitude and longitude) to IR information and the application of a U-Net-based convolutional neural network for improving the accuracy of retrieval algorithms. This research suggests that applying an appropriate CNN architecture on geographical and IR information provides an opportunity to improve the satellite-based precipitation products.

3.2. Data

3.2.1. Model Inputs

NOAA GOES Infrared Imagery

The NOAA Climate Prediction Center (CPC) globally merged IR product was developed to provide near-real time data for monitoring global precipitation (Janowiak et al. 2001). This dataset offers near-global (60°N-60°S) IR data with a 4-km spatial and an hourly temporal resolution from the international constellation of operational geostationary meteorological satellites for the period from 2000 to the present. The CPC-IR product comprises all channel observations from several international GEO satellites, including Meteosat-5 and Meteosat-7 (half-hourly IR images), Himawari-8 (hourly IR images) (Bessho et al. 2016), and GOES (3-hourly IR images). This dataset is accessible for public use through the Climate Prediction Center webpage[1].

Combined Passive Microwave Precipitation dataset (MWCOMB)

[1] https://www.cpc.ncep.noaa.gov/products/global_precip/html/wpage.full_res.html

Combined Passive Microwave Precipitation dataset (MWCOMB) was developed by the NOAA Climate Prediction Center. This product provides precipitation estimates with an 8-km spatial and 30-min temporal resolution by averaging the calibrated PMW rain rates from individual LEO satellites. MWCOMB combines precipitation information from multiple sensors, such as DMSP SSM/I, NOAA AMSU-B, and TRMM Microwave Imager (Weng et al. 2003; Joyce et al. 2004; Joyce and Xie 2011). The MWCOMB dataset can be obtained from the Climate Prediction Center[1]. In this study, we use MWCOMP dataset for training the model due to the following reasons: First, we do not have well-distibuted gauge observations over some regions and oceans; however, the goal of the proposed model is to be implemented over both land and oceans in the future. Second, PMW observations have the advantage of being retrieved through measuring direct microphysical information including liquid and frozen hydrometeors within the clouds. However, IR information is limited to indirect cloud-top information. Since the PMW sensors are direct means of measuring precipitation, utilizing less frequent PMW data to train model would help the retrieval algorithms to extend continuously over time. Third, MWCOMP is one of the most reliable satellite-based dataset, which have been used for training many real-time satellite precipitation estimation models (Sadeghi et al. 2021c).

3.2.2. Observation and Baseline Datasets

NCEP Stage IV QPE Product

National Centers for Environmental Prediction (NCEP) stage IV is a national multi-sensor (real-time gauge and WSR-88D radar) product covering the CONUS. This product merges data from 140 radars and around 5500 rain gauges over the CONUS (Lin and Mitchell 2005). Stage IV was produced as a 4 km x 4 km gridded product available over the Hydrologic Rainfall Analysis Project (HRAP) national grid system at hourly, 6-hourly, and 24-hourly intervals. Precipitation estimates derived from the a variety of sensors at the 12 regional National Weather Service (NWS) River Forecast Centers (RFCs) are subject to manual quality control and then mosaicked under the supervision of NCEP (Yilmaz et al. 2005). Continued efforts are made to investigate the development, processing, and improvement of stage IV

[1] ftp://ftp.cpc.ncep.noaa.gov/precip/global_MWCOMB/30min_8km/

concerning moderate to heavy rainfall events (Prat and Nelson 2015). The NCEP Stage IV is widely considered as the best gridded precipitation dataset over the CONUS due to its extensive quality control procedures (Smalley et al. 2014; Mehran and AghaKouchak 2014). Due to its long history and consistency of data production over CONUS, stage IV has been widely used in many previous satellite QPE (Quantitative Precipitation Estimation) comparisons such as TRMM, CMORPH, and PERSIANN (Chen et al. 2013; Mehran and AghaKouchak 2014; Beck et al. 2019; AghaKouchak et al. 2011). Stage IV data is available at noaa.org[1]. In this study, the daily temporal resolution of NCEP Stage IV data are used as benchmarks for evaluating the performance of PERSIANN-CCS and CNN-based models.

3.2.3. Baseline Model (PERSIANN-CCS)

The PERSIANN-CCS product provides the near-real time global precipitation estimates at 0.04° spatial resolution and half-hourly temporal resolution (Hong et al. 2004). This operational precipitation product has been developed at the CHRS and implemented as a part of NASA global precipitation measurement (GPM) integrated multi-satellite retrievals for GPM (IMERG) (Huffman et al. 2015). The PERSIANN-CCS dataset is accessible through the CHRS data portal[2].

3.3. Methodology

3.3.1. Convolutional Neural Network

Building blocks of a CNN architecture

A typical CNN network is generally comprised of three types of layers, namely the convolution layers, the pooling layers, and one or more fully connected layers at the end. The arrangement of CNN components plays a vital role in achieving the sustained high-performance model:

Convolutional layers: Convolution layers are the most important components of a CNN that extract features from input images (or feature maps from previous layers) through filters in the image domain. Filters are an array of numbers, which are called learnable weights, that

[1] https://www.emc.ncep.noaa.gov/mmb/ylin/pcpanl/stage4/
[2] http://chrsdata.eng.uci.edu/

determine the type of information to be extracted. Each of those filters is independently convolved followed by a nonlinear transformation (activation function) to generate the feature maps, which serve as inputs for the next layer.

Pooling layers: A convolutional layer is mostly followed by a pooling layer (also called subsampling layer). The pooling layers reduce the dimensions of the input layer through some local non-linear operations, such as average pooling and max pooling which are the most common operations. The average pooling calculates the average of the elements within the window to form the feature maps, while max pooling uses the maximum element within the window to form the output layer. The pooling operations result in the resolution of the feature maps becoming coarser. This can help the next convolution layer to extract high-level representations of the input data in a CNN model. Furthermore, the pooling layers reduce the number of subsequent learnable parameters to decrease the computation time and to control the over-fitting in the network.

Fully-connected layers: The fully-connected layers are typically used as the last few layers of a CNN model. These layers summarize the information from all hidden units in the previous layer to make the final decision.

Training a CNN

Training a network is the process of finding learnable parameters (i.e., kernels and weights) by minimizing the difference between the model prediction and given a truth dataset. In the first step, the input data under initial kernels and weights are transformed into the final output through the discussed layers in a CNN architecture. Then the model is trained by updating the learnable parameters with a backpropagation algorithm where the loss function and gradient descent algorithm play vital roles. The loss function measures the differences between model output and truth observation, while a gradient descent optimization algorithm is used to iteratively update the learnable parameters to minimize the loss (Yamashita et al. 2018).

3.3.2. Four Different CNN architectures for Precipitation Estimation

Overview of layers

Figure 3.1a depicts a convolutional encoder-decoder architecture that was used by Sadeghi et al. (2019b) for near-real time precipitation estimation over the central United States (30°–45°N, 90°–105°W) using IR and water vapor images. This convolutional encoder-decoder architecture consists of an encoder (contracting) section on the left side, a bottleneck section in the middle and a decoder (expansive) section on the right side. The encoder section follows the typical architecture of a CNN network. It consists of applying two 5×5 padded convolutions with a rectified linear unit (ReLU), as activation function, and a 2×2 max pooling operation for downsampling. The number of feature maps doubles at each downsampling step so that the architecture can learn the complex structures effectively. The bottleneck section mediates between contraction and expansion sections and is made of two 5×5 padded convolutions followed by a ReLU activation function. The decoder section consists of several expansion blocks for upsamling the feature maps. Each expansion block passes the feature maps to two 5×5 padded convolutions followed by a 2x2 convolution transpose function ("up-convolution"). In each block, the number of feature maps of the first convolution layer is reduced by half through the second convolution to maintain symmetry. At the final layer, a convolution is used to map each 32-component feature vector to the final output which is rainfall estimates with the same size as input(s).

In this work, we train and test the proposed encoder-decoder architecture using IR images (model 1) as well as using IR and latitude and longitude information (model 2). The water vapor information that was used in Sadeghi et al. (2019c) model is not included in these models due to two reasons: First, the water vapor information, unlike IR information, is not available globally. Here, we want to investigate capabilities of a CNN-based model for reliably estimating the rain rate based on only IR images for its future global implementation. Second, the operational PERSIANN-CCS algorithm utilizes only IR information for its rain rate estimation. For a fair comparison, we train and test a CNN-based model that leverage only IR images as input. In the second model, we input location information through adding latitude and longitude inputs to the same architecture used in model 1 to investigate whether it can improve the performance of the model's estimations. The hypothesis is that importing location information as inputs can facilitate training a CNN-based model to learn the various mechanisms of precipitation over the study area.

Figure 3.1b illustrates a U-Net convolutional architecture similar to that proposed by Ronneberger et al. (2015) for biomedical image segmentation. The U-Net architecture that we use for training model 3 (with IR input) and model 4 (with IR, latitude and longitude inputs) has the same layers to the convolutional encoder-decoder architecture shown in Fig 3.1a The only difference in these two architectures can be seen in the decoder section of U-Net architecture where the outputs of the upsampling layer are appended by feature maps of the corresponding encoder layer (copy and concatenate). The neurons in the first two hidden layers view only a small image window to learn low-level (detailed) features. Then, the size of the input information is reduced gradually in the encoder side in order to help a CNN-based model to view a larger portion of the image to extract high-level features (context) and to efficiently leverage the neighborhood information. However, some of the information is lost during this process in an encoder-decoder architecture. The U-Net architecture overcomes this problem by transferring the information from each encoding layer and concatenating it to a corresponding decoding layer to recover the features that are lost in the encoder side. This action helps a U-Net model to learn more expressive features by combing the low-level and high-level features in an efficient manner. We explore the performance of a U-Net convolutional architecture against a convolutional encoder-decoder architecture that was used by Sadeghi et al. (2019c) for near-real time precipitation estimation.

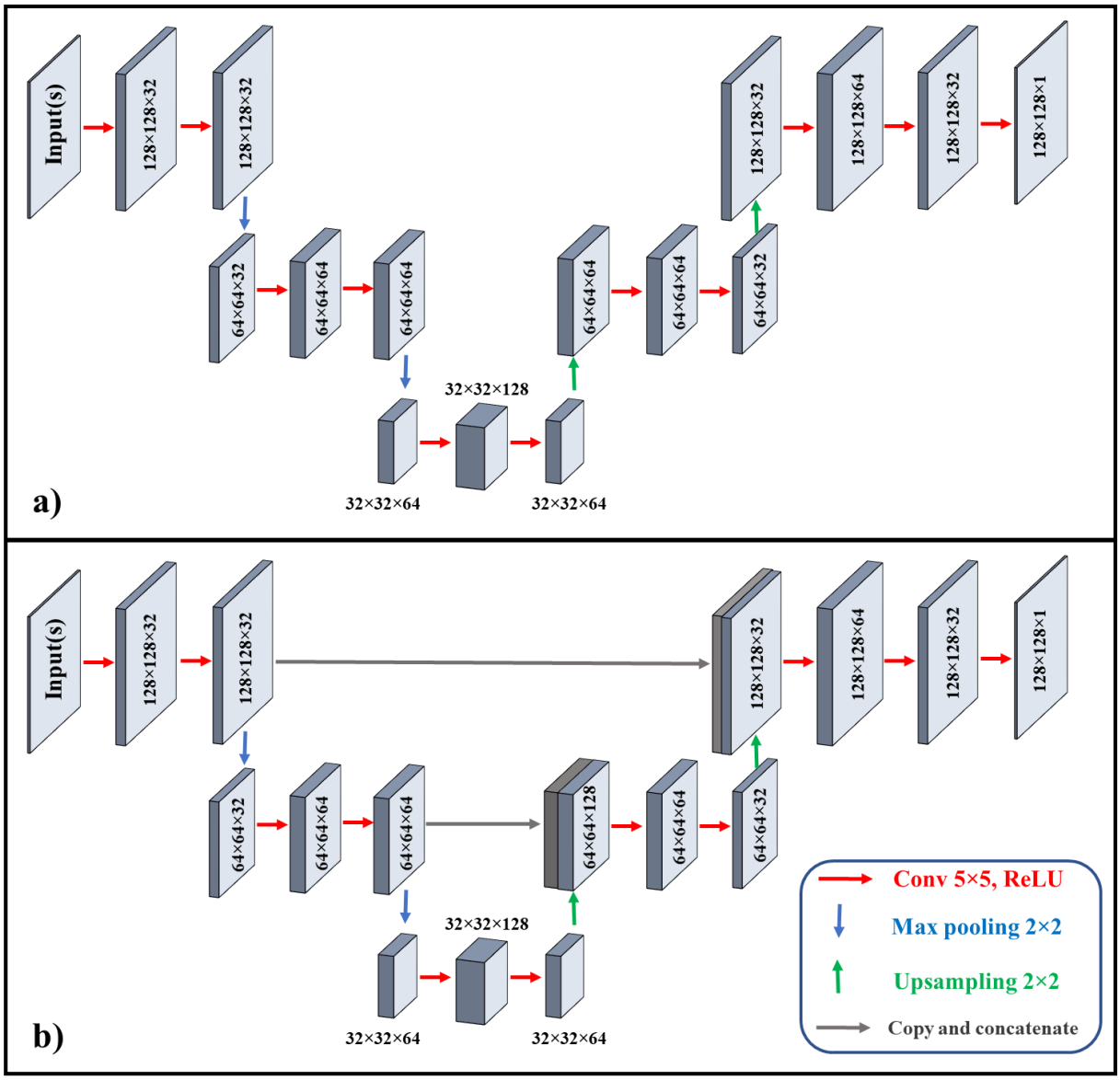

Figure 3.1 Overview of a) a convolutional encoder-decoder architecture for model 1 (Input: IR) and 2 (Inputs: IR and Latitude and longitude), b) a U-Net convolutional architecture (U-Net) for model 3 (Input: IR) and 4 (Inputs: IR and Latitude and longitude) for

Parameter tuning

The inputs and target datasets are divided into the training, validation, and test periods. The four proposed models are trained and validated separately for summer (June - August) of 2013, 2014, and 2015 using the MWCOMB dataset as the target. During the training and validating procedures of the CNN models, we used 80% of the samples to learn the weights

and biases of neurons in each model (training procedure). The remaining 20% of the samples was used for validating procedure to find the hyperparameters and the proper architecture. The training and validating procedures are vital to optimize the model parameters and also prevent overfitting (Chen et al. 2016). Then, the summer of 2017 is used for testing the proposed models to choose the best model through comparing all the proposed models with the NCEP stage IV radar observation as a reference. Then, the performance of the best model, referred to as PERSIANN-CNN, is compared with PERSIANN-CCS against the NCEP stage IV radar dataset during both summer and winter (October- December) of 2017 and for an extreme event, Hurricane Harvey (2017).

The proposed models were implemented in TensorFlow python platform (Abadi et al. 2016). To speed up the training process, the models were run on a graphics processing units (GPU) and a compute unified device architecture (CUDA). The training process starts with selecting initial parameter values, then applies the backpropagation algorithm to adjust the parameters in order to minimize the loss function using a gradient descent algorithm (Erhan et al. 2010). In the current study, the initial values were randomly chosen from a normal distribution. Then, the Adam gradient-based optimizer was utilized for minimizing the loss function, which was determined by calculating the mean square error (MSE) between the simulated and observed precipitation. Hyperparameters are the variables which determine the structure of a CNN model (e.g. number of hidden units, neuron size) and the variables which determine how the CNN network is trained (e.g. learning rate, batch size, epoch size). In the current study, we tested different combinations of the hyperparameters for each of the proposed models to optimize their learning parameters. Also, an early stopping criterion was implemented that halted the training if the MSE values did not improve after 10 epochs. In addition, to further reduce overfitting problems, the dropout method with varies ratio for different layers is adapted in this study. We found that the learning rate of 0.001, the minibatch size of 32, and epoch size of 75 leads the best performance for the proposed models.

3.3.3. Performance Measurements

Categorical Evaluation Metrics

To evaluate the ability of PERSIANN-CCS and CNN-based models in detecting rain/no rain pixels, categorical evaluation metrics are utilized. Statistics metrics in this category include the probability of detection (also called hit rate) (POD), false alarm ratio (FAR), and the critical success index (CSI), which are calculated by the following equations:

$$\mathrm{POD} = \frac{\mathrm{TP}}{\mathrm{TP+FN}} \quad \text{(Range: from 0 to 1; Perfect value: 1)}$$

$$\mathrm{FAR} = \frac{\mathrm{FP}}{\mathrm{TP+FN}} \text{ (Range: from 0 to 1; Perfect value: 0)}$$

$$\mathrm{CSI} = \frac{\mathrm{TP}}{\mathrm{TP+FP+FN}} \text{ (Range: from 0 to 1; Perfect value: 1)}$$

Where:

TP: Number of true positive events (Number of pixels correctly classified as rain) FP: Number of false positive events (Number of pixels incorrectly classified as rain)

FN: Number of false negative events (Number of pixels incorrectly classified as no rain)

Continuous Evaluation Metrics

To evaluate the performance of PERSIANN-CCS and CNN-based models against NCEP Stage IV in estimating the rainfall intensity, continuous evaluation metrics are calculated. These statistical metrics include Root Mean Square Error (RMSE), Correlation Coefficient (CC), and Mean Absolute Error (MAE), which are given below:

$$\mathrm{RMSE} = \frac{1}{\mathrm{n}}\sqrt{\sum_{\mathrm{i=1}}^{\mathrm{n}}(Sim_i - Ref_i)^2}$$

$$\mathrm{CC} = \frac{\frac{1}{n}\sum_{i=1}^{n}(Sim_i - \overline{Sim_i})(Ref_i - \overline{Ref_i})}{\sigma_{Sim}\,\sigma_{Ref}}$$

$$\mathrm{MAE} = \frac{1}{\mathrm{n}}\sum_{\mathrm{i=1}}^{\mathrm{n}}|Sim_i - Ref_i|$$

Where:

Sim: Simulation (PERSIANN-CCS, CNN-based models)

Ref: Reference observation (NCEP Stage IV)

n: number of observations

σ: standard deviation

3.4. Results and Discussion

3.4.1. Evaluating the performance of the 4 designed models at an hourly scale

In this section, the performance of the designed models described in the methodology section (Figure 3.1) is evaluated over the continental United States (CONUS). Figure 3.2 indicates the spatial distribution of each model with reference to the NCEP stage IV radar observation, over summer 2017. In general, model 4, which applies the U-Net architecture on IR information along with latitude and longitude, has performed substantially better compared to other models according to all performance metrics. In addition, comparing model 1 (without leveraging latitude and longitude as inputs) and model 2 (with leveraging latitude and longitude as inputs), which both apply an identical CNN architecture indicates that adding geographical information can improve the performance of a CNN-based model for estimating the near-real time precipitation. In terms of POD and CSI, model 2 outperformed model 1 by 25 % and 13%, respectively. However, model 2 performed poorer than model 1 by 38% in terms of FAR. Despite the lower performance of model 2 for FAR compared to model 1, model 2 has performed more homogeneously and consistently over the CONUS. This highlights that a CNN-based model can learn the different mechanisms of rainfall occurring in different regions over the CONUS by adding latitude and longitude as inputs. For RMSE, and MAE model 2 was more accurate than model 1 by 1%, and 19%, respectively. Comparing model 3 and 4 which both apply an identical U-Net architecture on different inputs also supports the previous finding that adding geographical inputs can improve the accuracy of a CNN- based model for precipitation estimation. Furthermore, model 4 outperformed in all representative evaluations including FAR.

Comparing model 1 (architecture (a) in Fig. 3.1) with model 3 (architecture (b) in Fig. 3.1), which use different architectures on the same inputs, reveals that the U-Net architecture can significantly improve the performance of CNN models compared to the architecture employed by Sadeghi et al. (2019d). More Specifically, model 3 outperformed model 1 by 16%, 12%, and 19% in terms of POD, FAR, and CSI, demonstrating the detection skill of the U-Net architecture. Furthermore, RMSE and MAE of model 3 were lower than model 1 by 8% and 10%, demonstrating the estimation accuracy of the U-Net model. Comparing model 2

and 4, which also utilize two different architectures discussed in Fig. 3.1, also supports the outperformance of the U-Net architecture for estimating precipitation. It could be concluded that adding bypass connections between encoding layer and decoder layers in U-Net can recover the lost information during the execution of the upsampling layers. This feature of U-Net makes it to more efficient and effective in both detecting the rain/no-rain pixels and estimating the rain rate. Figure 3.2 shows that all of the designed models have a similar performance pattern for evaluation metrics, but model 4 achieved better agreement with that of NCEP stage IV as the reference. Having the same CC for all models and the similarity in distribution pattern of evaluating metrics could be due to correlation between cloud-top temperature and rainfall in different regions over the CONUS.

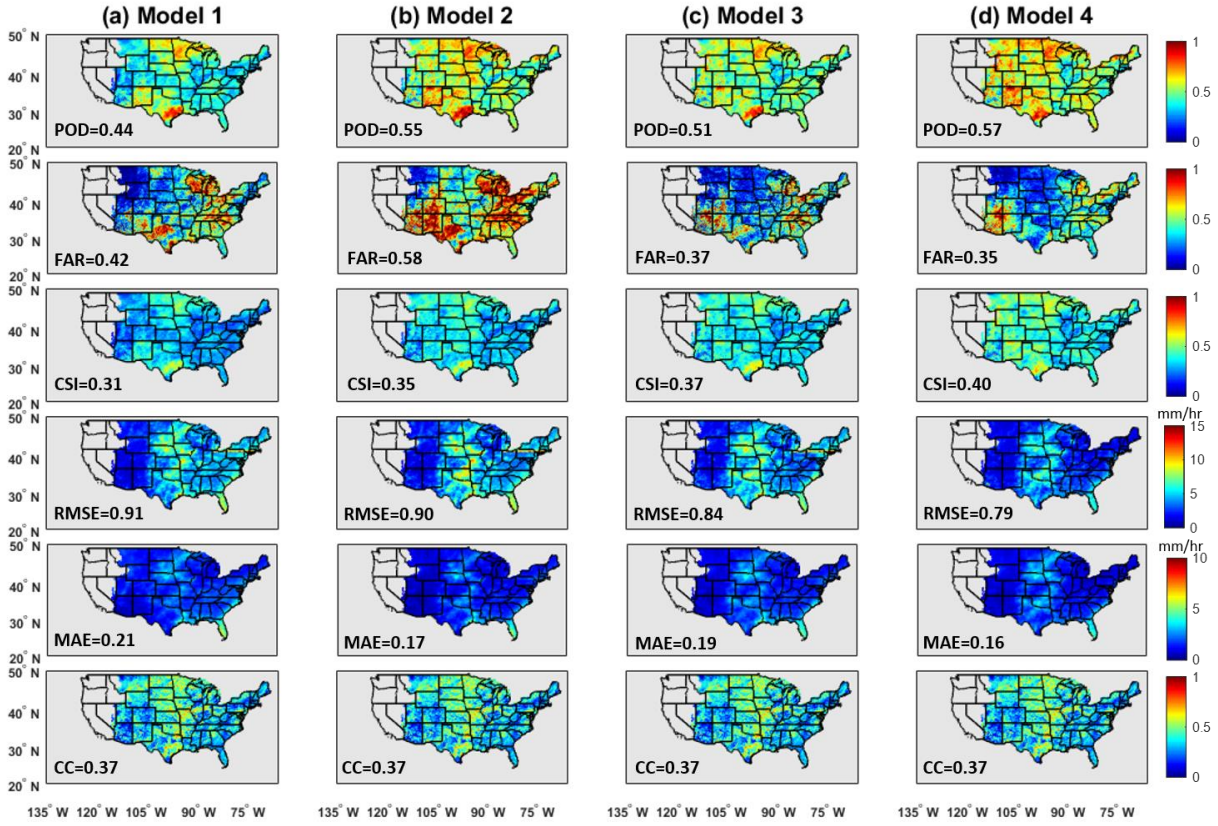

Figure 3.2 Categorical (POD, FAR, CSI) and continuous (MAE, RMSE, CC) of the four designed models at an hourly scale against NCEP stage IV radar observation during summer 2017.

3.4.2. Performance Evaluation of PERSIANN-CNN and PERSIANN-CCS against NCEP stage IV at an Hourly Scale

In this section, the performance of the best performing CNN model (model 4), PERSIANN-CNN, and PERSIANN-CCS are evaluated against NCEP stage IV at an hourly scale. Figure 3.3 shows the IR cloud-top temperature and the rainfall estimates from the PERSIANN-CNN and the PERSIANN-CCS models for the extreme rainfall occurred at 0700 UTC August 22, 2017. As shown in Fig. 3.3, PERSIANN-CNN provides a more accurate representation of the pattern and intensity of the rainfall as compared to PERSIANN-CCS. In addition, PERSIANN-CCS only captures a small portion of the extreme rain rate, where the IR cloud-top temperature was the lowest. Assigning more rain rates to clouds with lower temperature is considered as the main drawback of most IR-based precipitation retrieval algorithms such as PERSIANN-CCS. In the PERSIANN-CCS algorithm, the clouds are segmented based on IR cloud-top temperature into distinctive cloud patches with an incremental temperature threshold (ITT) method. Then, all segmented cloud patches are classified into 400-category clusters based on similarity of cloud features using self-organizing feature maps (SOFMS). Finally, a fully connected layer is utilized to find the relationship of IR cloud-top temperature and rainfall rates for each classified cloud cluster. The essence of the discussed shortcoming can be due to two reasons: First, using temperature thresholds for cloud segmentation in the PERSIANN-CCS algorithm can result in associating more rain rates to the clouds with lower temperature. Second, using a fully connected network in the PERSIANN-CCS algorithm makes it hard to efficiently and effectively learn the rain structure to estimate the correct pattern and intensity of the rainfall.

Due to complexity level of fully connected networks and fuzzy nature of rainfall, a fully connected algorithm, ends up learning to one-on-one pixels in most cases, meaning that it trains the parameters of each pixel separately. This limits a fully connected model to efficiently use the neighborhood information in most cases resulting in colder clouds showing more intense precipitation. On the other hand, a CNN-based model, such as PERSIANN-CNN, can effectively leverage the local neighborhood information to estimate the rain rate for each pixel. This feature is mainly due to CNN structure which allows sharing the same filter in a single layer.

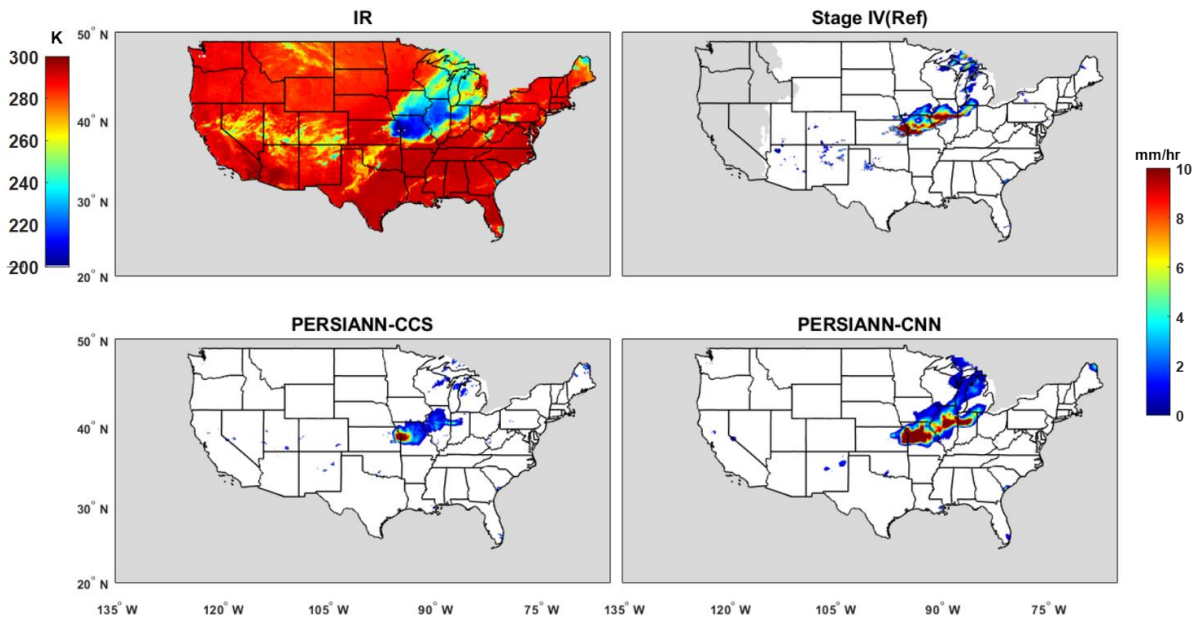

Figure 3.3 Maps of cloud-top temperature (K) from IR imagery and precipitation rate (mm/h) from NCEP stage IV radar observation (reference), PERSIANN-CCS (baseline), and PERSIANN-CNN (proposed model) for 0700 UTC 22 August 2017.

Figure 3.4 presents the spatial distribution of categorical (POD, FAR, and CSI) and continuous (MAE, RMSE, and CC) metrics of PERSIANN-CCS and PERSIANN-CNN against NCEP stage IV, at an hourly scale throughout the verification period including summer and winter 2017. The verification metrics were calculated for each pixel and at an hourly temporal scale over the CONUS for summer and winter, separately. In general, the results indicate that PERSIANN-CNN outperforms PERSIANN-CCS in terms of all categorical indices almost over all the CONUS during both summer and winter 2017. In terms of POD, FAR, and CSI, PERSIANN-CNN outperformed PERSIANN-CCS during summer (winter) by 16% (10%), 48% (68%), and 73% (50%), respectively. Additionally, the PERSIANN-CNN model showed the best overall performance in estimation accuracy over the verification period. For RMSE and CC, PERSIANN-CNN was more accurate than PERSIANN-CCS during summer (winter) by 21% (18%), and 85% (59%) respectively. In terms of MAE, PERSIANN-CNN performed better than PERSIANN-CCS by 47% during the summer; however, it performed poorer than PERSIANN-CCS by 32% during winter. Furthermore, Figure 3.4 suggests that the

performance metrics of PERSIANN-CNN are more homogeneous and consistent compared to PERSIANN-CCS across space over the CONUS. This spatial homogeneity, which is more noticeable in spatial patterns of POD and CSI, can be related to the use of geographical information in the CNN-based model. The use of latitude and longitude as inputs in PERSIANN-CNN enables the model to learn different mechanisms of precipitations occurring over the CONUS, resulting in showing more homogeneity and consistency in the performance metrics.

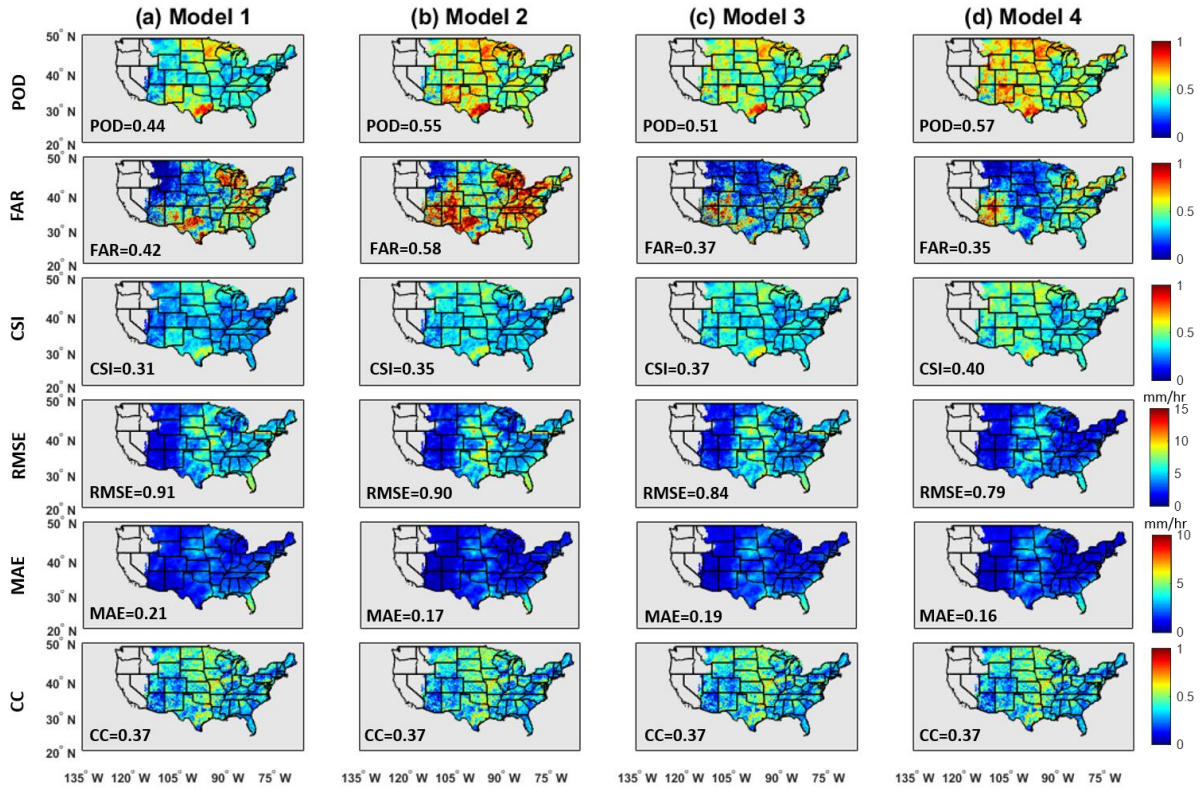

Figure 3.4 Categorical (POD, FAR, CSI) and continuous (MAE, RMSE, CC) metrics of PERSIANN-CCS, and PERSIANN-CNN at an hourly scale over the verification period (summer and winter 2017).

3.4.3. Performance Evaluation of PERSIANN-CNN and PERSIANN-CCS against NCEP stage IV at Daily Scale

To demonstrate how a CNN-based model can substantially improve the daily estimates of precipitation events, an intense event is randomly selected from noticeable precipitation events within the validation period. Figures 3.5 presents the daily estimates of PERSIANN-

CCS and PERSIANN-CNN against NCEP stage IV for the extreme precipitation event that occurred on 25 September 2017. As observable from Fig. 3.5, PERSIANN-CNN provides more accurate estimates of the rainfall intensity, while PERSIANN-CCS underestimates the intense precipitation for this event.

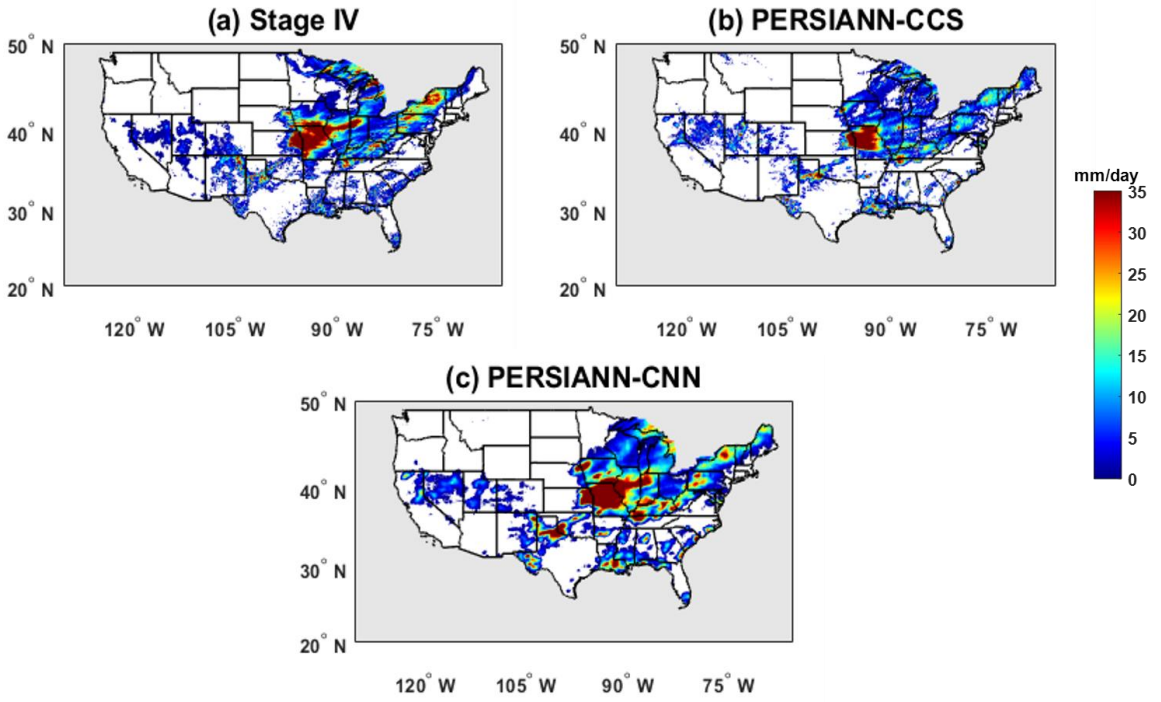

Figure 3.5 Comparison of daily rainfall from NCEP stage IV, PERSIANN-CNN, and PERSIANN CCS estimates for 25 Sep 2017.

To evaluate the daily performance of PERSIANN-CNN and PERSIANN-CCS against NCEP Stage IV throughout summer and winter, the spatial distribution of categorical and continuous metrics is plotted in Figure 3.6. The POD of the PERSIANN-CNN showed distribution patterns similar to those of the PERSIANN-CCS, but the PERSIANN-CNN achieved better agreement with radar observations and with higher PODs almost over the whole CONUS for both summer and winter. This can be related to the different correlations between cloud-top temperature and rainfall occurrence for different regions over the CONUS. In terms of FAR, PERSIANN-CNN estimated the rainfall with significantly lower FAR compared to PERSIANN-CCS. Specifically, the FAR decreased by 69% and 58% during the

summer and winter. The higher values of CSI also indicate that PERSIANN-CNN has a higher capability to detect rainfall compared to PERSIANN-CCS during both summer and winter. In term of continuous metrics, RMSE of the daily rainfall estimates for PERSIANN-CNN with respect to NCEP Stage IV were lower than that of PERSIANN-CCS by 20% and 15% during summer and winter, respectively. In terms of MAE, PERSIANN-CNN and PERSIANN-CCS estimates have similar distributions to RMSE index. Also, the CC of PERSIANN-CNN is significantly higher by 140% and 38% than that of PERSIANN-CCS over summer and winter, showing the higher estimation accuracy of PERSIANN-CNN compared to PERSIANN-CCS for daily precipitation estimation.

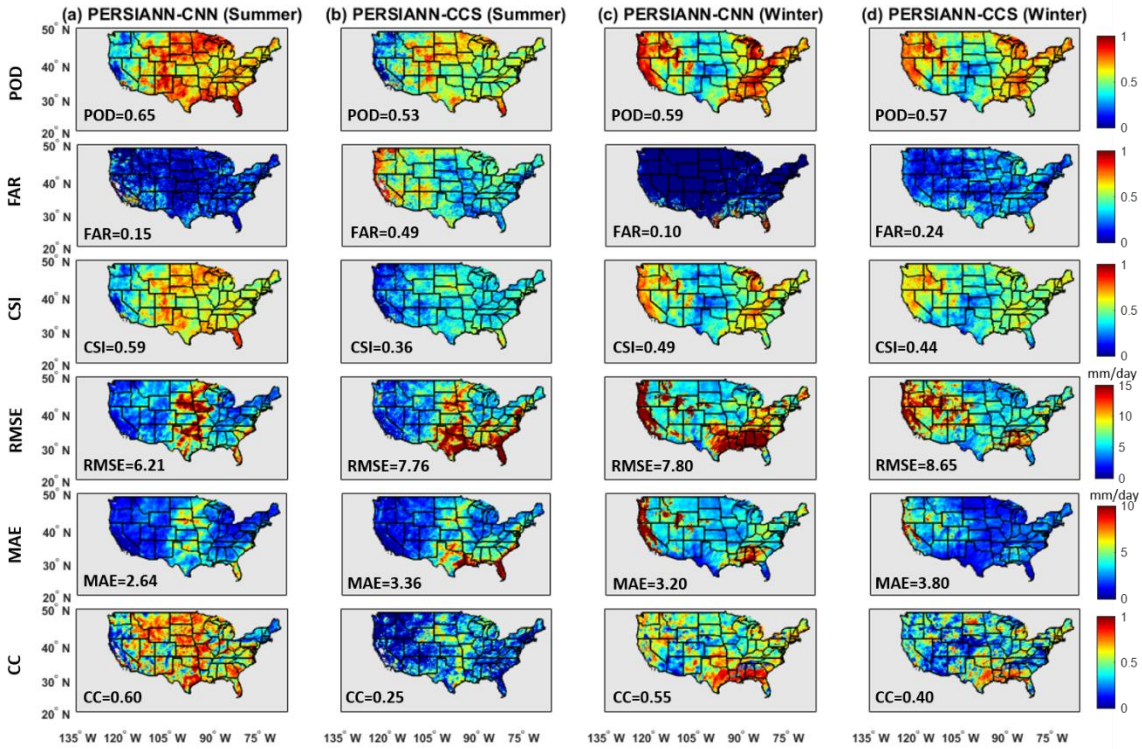

Figure 3.6 Categorical (POD, FAR, CSI) and continuous (MAE, RMSE, CC) metrics of PERSIANN-CCS, and PERSIANN-CNN at a daily scale over the verification period (summer and winter 2017).

3.4.4. Case study: Hurricane Harvey

To further evaluate the performance of PERSIANN-CNN and PERSIANN-CCS with respect to radar observationS in capturing extreme precipitation, Hurricane Harvey was studied. In August 2017, Hurricane Harvey hit the Southeastern regions of the United States mostly

Southeast Texas, and Louisiana. Hurricane Harvey is classified as a Category 4 hurricane that caused catastrophic damages and is considered as one of the costliest extreme precipitation events that struck in the United States' history. The total damage is estimated to be more than $125 billion and it is confirmed that there were more than 68 deaths (National weather service, www.weather.gov). The daily estimates of NCEP Stage IV, PERSIANN-CCS, and PERSIANN-CNN for the extreme precipitation that occurred between August 26 to 30, 2017 are presented in Figure 3.7. As shown in Fig. 3.7, PERSIANN-CCS severely underestimated the rain rate, particularly during August 26-29. Specifically, PERSIANN-CCS failed to capture most of the intense rainfalls occurred over Louisiana that are observed in the reference product (NCEP Stage IV). In contrast, PERSIANN-CNN estimated both spatial patterns and amounts of rainfall with a great resemblance to NCEP Stage IV.

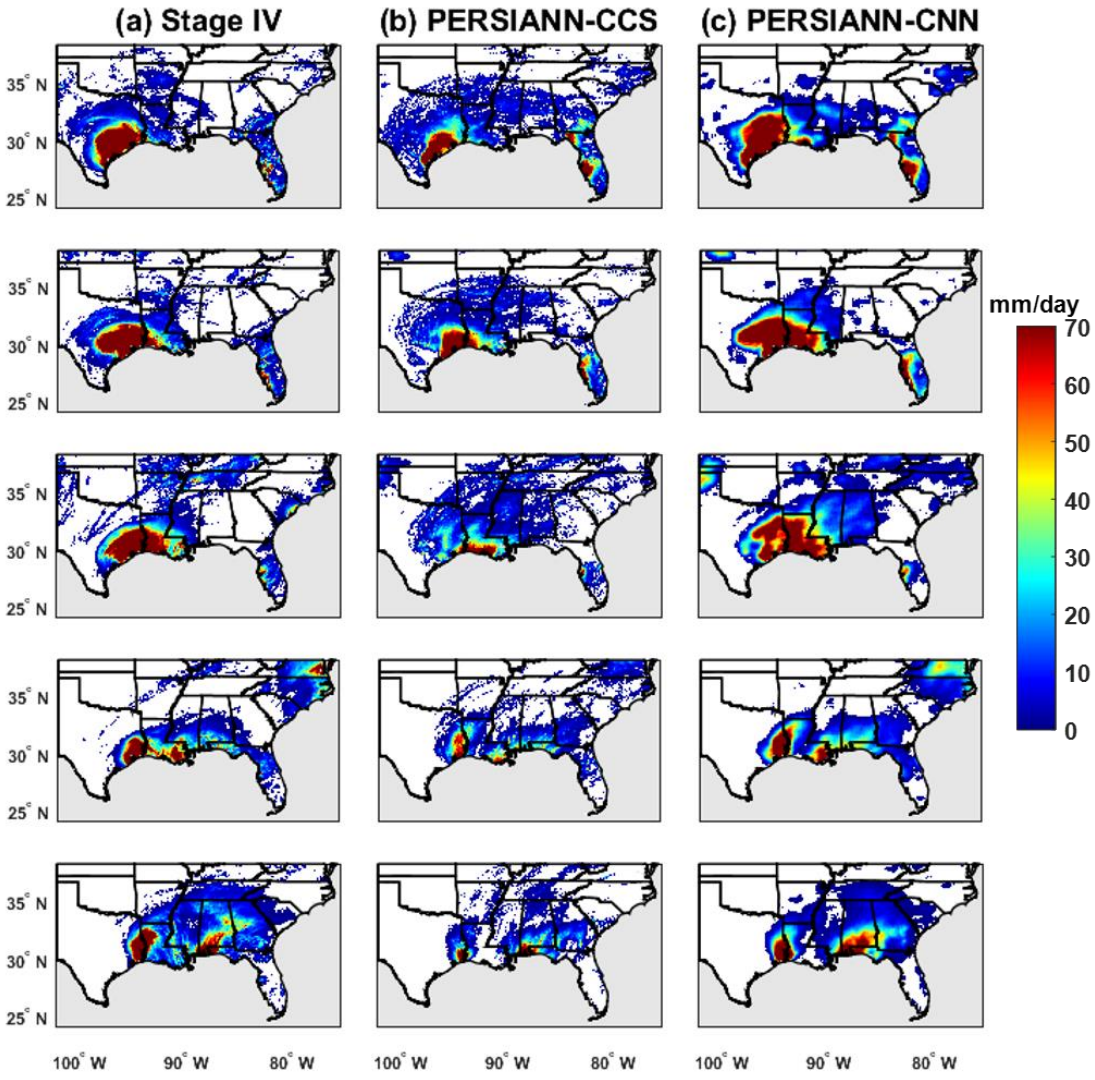

Figure 3.7 The spatial precipitation evolution of Hurricane Harvey for the period between August 26 to 30 from (a) Stage IV, (b) PERSIANN-CCS, (c) PERSIANN-CNN

To explore the daily performance of PERSIANN-CCS against PERSIANN-CNN at various spatial resolutions during Hurricane Harvey, scatterplots of their daily precipitation estimates versus the radar observations are presented (Fig. 3.8). These graphs demonstrate the pixel by pixel association between the simulated estimates (PERSIANN-CCS or PERSIANN-CNN) and the radar observations (NCEP Stage IV) for 0.04° (a, c) and 0.25° (b, d) spatial resolutions and at a daily time scale. One can see that PERSIANN-CCS severely underestimated heavier rainfalls as evidenced by the cluster of points located below the 45° perfect correlation line in both 0.04° and 0.25° spatial resolutions during this hurricane. During the described extreme event, PERSIANN-CNN showed higher correlations, and

relatively lower RMSE with respect to radar observations at both spatial resolutions. This finding also highlights the better performance of PERSIANN-CNN compared to PERSIANN-CCS for accurately estimate the amount of intense extreme events.

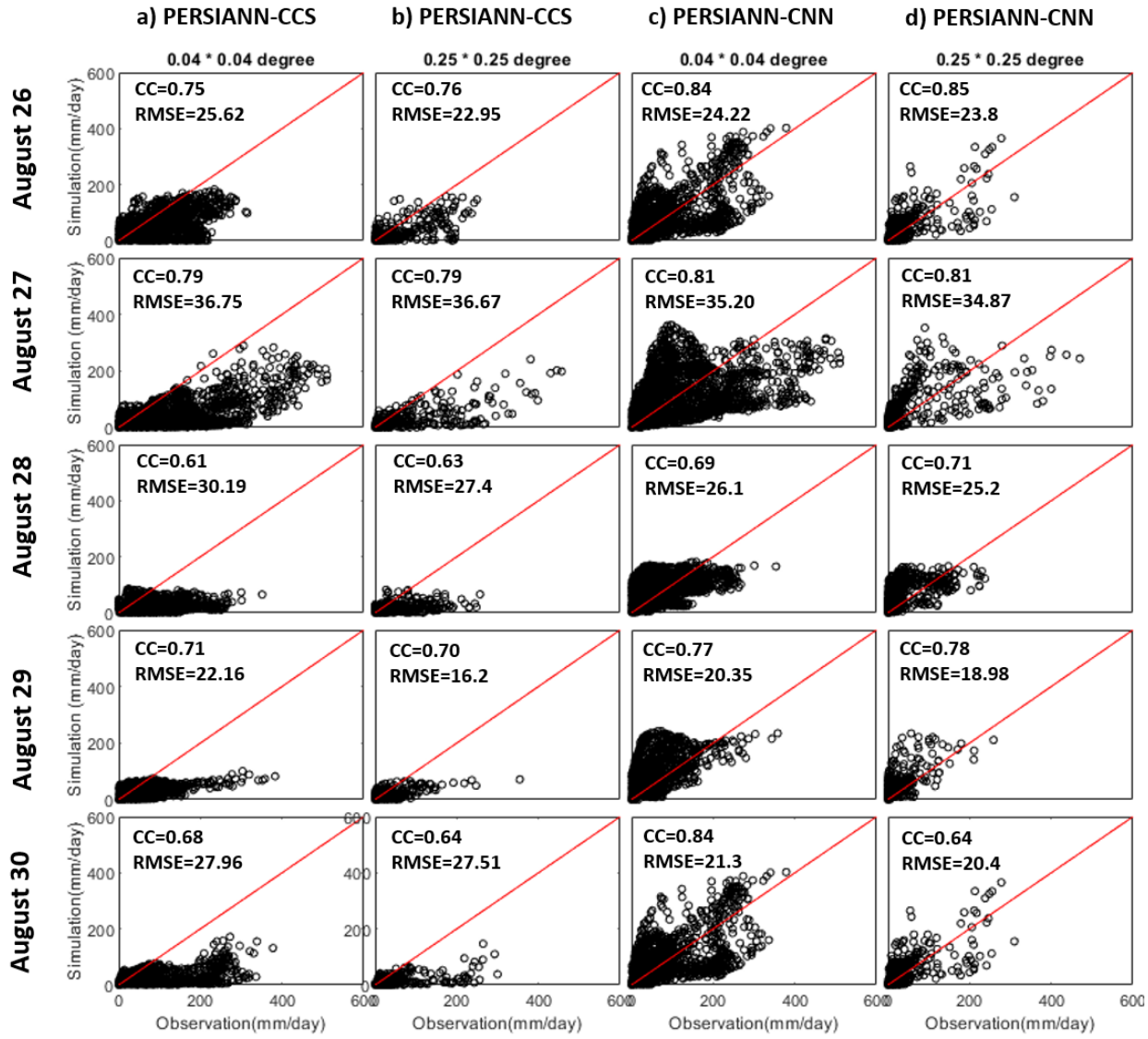

Figure 3.8 Scatterplots of radar measurements (observation) vs PERSIANN-CCS, and PERSIANN-CNN (simulations): daily rainfall estimation at two spatial scales over the affected area during the Hurricane Harvey (Aug. 26 to 30, 2017)

3.5. Conclusions

This study explored the application of a CNN-based architecture, which utilizes geographical and IR information, for detecting and estimating near real-time precipitation.

Specifically, this study was designed to investigate whether adding latitude and longitude information to IR information can improve the near real-time precipitation estimates. Also, we explored two different CNN-based architectures to show the effectiveness of applying a U-Net architecture compared to the precipitation retrieval algorithm introduced by Sadeghi et al. (2019b). For this purpose, four different CNN-based models were trained at hourly temporal and 0.04° × 0.04° spatial resolution over the CONUS using a combined PMW precipitation dataset. Then, these models were evaluated against NCEP Stage IV radar observation to investigate the effectiveness of adding geographical information and using U-Net architecture for precipitation estimation. The higher performance of models leveraging geographical information highlights that this additional information can help CNN-based models to learn the different mechanisms of rainfall occurring in different regions over the CONUS during the training process. In addition, a U-Net architecture can significantly improve the accuracy of estimates compared to the CNN-based model developed by Sadeghi et al.(2019b). In particular, we concluded that adding bypass connections between downscaling and upscaling layers in U-Net architecture helps to recover the lost information during upscaling parts of a CNN model lacking those connections.

The performance of the model which applies U-Net architecture on IR and geographical information (referred to as PERSIANN-CNN) was tested against PERSIANN-CCS at hourly and daily scales over summer and winter. Model evaluation procedures indicated that PERSIANN-CNN outperforms PERSIANN-CCS in capturing the pattern of precipitation, detecting rain/ no rain, and estimating the intensity of rainfall throughout the whole verification period. At an hourly scale, PERSIANN-CNN outperformed PERSIANN-CCS by 73% (and 50%) in the CSI during summer (and winter), showing the detection skills of the proposed model. In addition, the RMSE of the rainfall estimates with respect to the NCEP Stage IV radar observation, for PERSIANN-CNN was lower than that of PERSIANN-CCS by 21% (18%), demonstrating the estimation accuracy of the PERSIANN-CNN. Daily evaluations indicated that PERSIANN-CNN outperformed PERSIANN-CCS in terms of POD, FAR, and CSI, during summer (winter) by 23% (4%), 69% (58%), and 64% (11%), respectively. For RMSE, MAE and CC, PERSIANN-CNN was more accurate than PERSIANN-CCS during summer (winter) by 20% (10%), 21% (16%), and 140% (38%), respectively. The performance of PERSIANN-CNN and PERSIANN-CCS in estimating the extreme precipitation was assessed

for Hurricane Harvey (2017). The results showed that PERSIANN-CNN estimates rainfall intensity with a great resemblance to NCEP Stage IV, while PERSIANN-CCS underestimates the intensity occurred over the Louisiana State during the Hurricane. These results highlight that the proposed model has the potential to be used in early warning systems to mitigate natural disasters related to intense storm events such as hurricanes.

This study creates a promising opportunity for improving the near real-time satellite-based precipitation estimation datasets. Furthermore, due to availability of global IR information back to approximately 1983, there is a great potential for developing a high spatial resolution climate data record using the proposed model. Expanding on the research presented here, researchers at the Center for Hydrometeorology and Remote Sensing (CHRS) are working on global implementation of the proposed model. One of the challenges for global implementing of the proposed model is training over the regions with little PMW information. Addressing this challenge requires further investigation.

CHAPTER FOUR:

EVALUATION OF PERSIANN-CDR CONSTRUCTED USING GPCP V2.2 & V2.3 AND A COMPARISON WITH TRMM 3B42 V7 AND CPC UNIFIED GAUGE-BASED ANALYSIS IN GLOBAL SCALE

The contents of Chapter 4 are published in the Journal of Remote Sensing

Citation: Sadeghi, M., Akbari Asanjan, A., Faridzad, M., Afzali Gorooh, V., Nguyen, P., Hsu, K., ... & Braithwaite, D. (2019). Evaluation of PERSIANN-CDR constructed using GPCP V2. 2 and V2. 3 and a comparison with TRMM 3B42 V7 and CPC unified gauge-based analysis in global scale. Remote Sensing, 11(23), 2755.

4.1. Abstract

Providing reliable long-term global precipitation records at high spatial and temporal resolutions is crucial for climatological studies. Satellite-based precipitation estimations are a promising alternative to rain gauges for providing homogeneous precipitation information. Most satellite-based precipitation products suffer from short-term data records which make them unsuitable for various climatological and hydrological applications. However, Precipitation Estimation from Remotely Sensed Information using Artificial Neural Networks-Climate Data Record (PERSIANN-CDR) provides more than 35 years of precipitation record at 0.25° × 0.25° spatial and daily temporal resolutions. The PERSIANN-CDR algorithm uses monthly Global Precipitation Climatology Project (GPCP) data, which has been recently updated to version 2.3, for reducing the biases in the output of the PERSIANN model. In this study, we constructed PERSIANN-CDR using the newest version of GPCP (V2.3). We compare the PERSIANN-CDR dataset that is constructed using GPCP V2.3 (from here on referred to as PERSIANN-CDR V2.3) with the PERSIANN-CDR constructed using GPCP V2.2 (from here on PERSIANN-CDR V2.2), at monthly and daily scales for the period from 2009 to 2013. First, we discuss the changes between PERSIANN-CDR V2.3 & V2.2 over the land and ocean. Second, we evaluate the improvements in PERSIANN-CDR V2.3 with respect to the Climate Prediction Center (CPC) unified gauge-based analysis, a gauged-based reference, and Tropical Rainfall Measuring Mission (TRMM 3B42 V7), a commonly-used satellite reference, at monthly and daily scales. The results show noticeable differences between PERSIANN-CDR V2.3 & V2.2 over oceans between 40° and 60° latitude in both Northern and Southern hemispheres. Monthly and daily scale comparisons of the two bias-adjusted versions of PERSIANN-CDR with the above-mentioned references emphasize that PERSIANN-CDR V2.3 has improved mostly over the global land area, especially over the CONUS and Australia. The updated PERSIANN-CDR V2.3 data has replaced V2.2 data for the 2009-2013 period on https://chrsdata.eng.uci.edu

4.2. Materials:

Global Precipitation Climatology Project (GPCP) Monthly product

GPCP is part of the Global Energy and Water Cycle Exchanges (GEWEX) activity under the World Climate Research Program (WCRP). The GPCP monthly 2.5° x 2.5° precipitation product provides consistent global data by merging different satellite-based estimations (passive microwave/infrared) over the land and ocean along with precipitation gauge information from GPCC over the land. More detail on the input data and the merging process can be found in (Huffman et al. 1997; Xie et al. 2003). Recently, Version 2.3 of the GPCP product has been released which includes updates to the cross-calibration procedures of rainfall estimation and updates in the gauge analysis methods (Adler et al. 2018). The GPCP dataset is available via the Earth System Science Interdisciplinary Center (ESSIC) and Cooperative Institute for Climate and Satellites (CICS), University of Maryland College Park[1]. Additional information can be found in (Adler et al. 2018).

CPC Global Unified Gauge-Based Analysis of Daily Precipitation

The CPC Global Unified Gauge-Based Analysis of Daily Precipitation dataset is a National Oceanic and Atmospheric Administration (NOAA) Climate Prediction Center (CPC) product. Over the globe, the CPC unified gauge-based analysis product employs more than 30,000 stations from multiple sources, including Global Telecommunication System (GTS), Cooperative Observer Network (COOP), and other national and international agencies, providing a daily precipitation estimation at a 0.5° x 0.5° spatial resolution from 1979 to the present (Xie and Arkin 1997). Over the CONUS, the CPC unified gauge-based analysis product contains information from more than 8,000 stations in order to estimate precipitation with a spatial resolution of 0.25° x 0.25° at daily scale from 1948 to the present. One of the challenges in producing a gauged-based daily precipitation data set is to handle the reported data from different stations which use various methods of reporting time (Xie et al. 2007). The end of day (EOD) definition for accumulating 24-hourly precipitation may differ from one country to another. For example, over the CONUS the rain rate values are accumulated from 12Z of the day before to 12Z of that day. In this study, we use the finer resolution CPC

[1] http://gpcp.umd.edu

unified gauge-based analysis dataset for evaluations over the CONUS. In addition, as we discuss in the Methodology section, we use a custom variant of the PERSIANN-CDR with the same EOD definition as CPC unified gauge-based analysis for our comparisons over the CONUS. The CPC global unified gauge analysis is used for comparison at monthly scale over the globe. Both CPC datasets are available for public use (ftp://ftp.cdc.noaa.gov/Datasets). A comprehensive description of the CPC unified gauge-based analysis interpolation algorithm can be found in (Xie and Arkin 1997; Chen et al. 2008)

The Tropical Rainfall Measuring Mission (TRMM 3B42 V7)

The National Aeronautics and Space Administration (NASA) in cooperation with the Japan Aerospace Exploration Agency (JAXA) launched The Tropical Rainfall Measuring Mission (TRMM) in 1997 in order to measure rainfall information around tropical and subtropical areas. TRMM Multi-Satellite Precipitation Analysis (TMPA), one of the TRMM products, provides 3-hourly precipitation estimates at 0.25° x 0.25° for the latitude band of 50°N to 50°S. In this study we utilize the daily temporal scale of TRMM 3B42 V7[1]. This product derives precipitation by combining information from two different types of satellite sensors: PMW and geostationary-infrared (Geo-IR) sensors. More detailed information can be found in (Huffman et al. 2007). In this study, the TRMM 3B42 V7 estimates are utilized for evaluating the two versions of PERSIANN-CDR over the ocean and for daily global comparison over the land. We do not use CPC unified gauge-based analysis for daily comparison over the land due to its EOD definition which may vary from one country to another.

PERSIANN-CDR

The PERSIANN-CDR product was developed by the Center for Hydrometeorology and Remote Sensing (CHRS) at the University of California, Irvine (UCI). This dataset is available as an operational climate data record via the NOAA National Centers for Environmental Information (NCEI) Program[2] and via the CHRS Data Portal[3]. This near-global (60°N-60°S),

[1] https://pmm.nasa.gov/data-access/downloads/trmm
[2] https://www.ncdc.noaa.gov/cdr
[3] http://chrsdata.eng.uci.edu/

high-resolution (0.25° x 0.25°), long-term record (from 1983 to present) precipitation product has a daily resolution on UTC days. The PERSIANN-CDR algorithm utilizes GridSat-B1 infrared information (Knapp 2008; Rossow and Duenas 2004) as input and NCEP stage IV hourly precipitation data (Lin and Mitchell 2005; Westrick et al. 1999) to update the model parameters. In order to reduce the bias, this product is bias-adjusted with GPCP precipitation product at 2.5° x 2.5° and a monthly time scale. Additional details about PERSIANN-CDR algorithm can be found in (Ashouri et al. 2015; Sadeghi et al. 2019a).

4.3. Methodology:

This study applies the same methodology used in the original PERSIANN-CDR algorithm introduced by (Ashouri et al. 2015). In the first step of the PERSIANN-CDR algorithm, the PERSIANN algorithm (Hsu et al. 1997) is applied to GridSat-B1 merged infrared data from GEO satellites. The outcome is called PERSIANN-B1 and it is a 3-hourly precipitation estimate dataset from 1983 to present at quarter degree resolution for the latitude band 60°N to 60°S. Then, in order to adjust the biases of this dataset, PERSIANN-B1 is temporally aggregated to obtain monthly scale PERSIANN-B1 dataset to match the GPCP data in temporal resolution. In the same manner, PERSIANN-B1 data with spatial resolution of 0.25° x 0.25° will be aggregated to match the 2.5° x 2.5° GPCP data. The temporal and spatial aggregations are computed using the following equation:

$$R_{\mathrm{PERSIANN-B1}}(i', j') = \sum^{nd} \sum^{nh} (\sum^{10} \sum^{10} [r_{\mathrm{PERSIANN-B1}}(i, j) \geq thd]) \qquad (1)$$

In equation (1) $R_{\mathrm{PERSIANN-B1}}$ and $r_{\mathrm{PERSIANN-B1}}$ are the aggregated monthly 2.5° PERSIANN-B1 data and original 3-hourly 0.25° PERSIANN-B1 data, respectively. The i and j are the latitude and longitude of the PERSIANN-B1 at 0.25° resolution. Similarly, i′ and j′ are the latitude and longitude of the aggregated PERSIANN-B1 at 2.5° resolution. "thd" is a pre-defined threshold to eliminate noisy low value pixels. As an artifact of PERSIANN estimation process, small fractions of non-raining pixels are falsely assigned with light rainfall rates. To minimize this effect, we applied a threshold of 0.1 mm/day which eliminates the falsely assigned light rainfall rates with no rainfall. The nd and nh are the number of days and number of 3-hourly samples in a day, respectively. In the next step, the bias-adjustment weights are calculated for each 2.5° grid cell of monthly data:

$$w(i',j') = R_{GPCP}(i',j') / R_{PERSIANN-B1}(i',j'),\ 0 \le w \le 20 \qquad (2)$$

Where R_{GPCP} is the monthly rain rate of GPCP for a given cell. Due to the linearity of the bias-adjusting technique, the bias-adjustment weights (w) at 2.5° spatial resolution and monthly temporal resolution can be linearly interpolated into its corresponding 10x10, 0.25°, 3-hourly PERSIANN-B1 grid cell estimates. The interpolation of w will ensure a smooth and continuous transition of bias-adjustment factors at the 0.25° resolution.

$$Adj\_r_{PERSIANN-B1}(i,j) = w(i,j) * r_{PERSIANN-B1}(i,j) \qquad (3)$$

$Adj\_r_{PERSIANN-B1}$ is the GPCP-adjusted 3-hourly 0.25° PERSIANN-B1 precipitation data. In the final step of PERSIANN-CDR preparation, 3-hourly PERSIANN-B1 data are aggregated to daily scale to reduce the uncertainties:

$$\text{PERSIANN-CDR}(i,j) = \sum_{n=1}^{N} Adj - r_{PERSIANN-B1}(i,j,n) \qquad (4)$$

Where N is the number of 3-hourly $Adj - r_{PERSIANN-B1}$ data for each day. Data for each 3hrly file are accumulated on a pixel by pixel basis and then converted to 24hr if N is more than 4 out of 8 per day.

It should be noted that we accumulate 3-hourly PERSIANN-B1 with two different EOD definitions in order for each to be consistent with TRMM 3b42 V7 or the CPC CONUS dataset.

In the first part of this study, we determine the amount of change between the two bias-adjusted versions of PERSIANN-CDR and two versions of GPCP (V2.2 & V2.3) at monthly scales from 2009 to 2013. Both versions of PERSIANN-CDR at daily scale are aggregated to monthly time scale. To determine the amount of change we use Mean Absolute Difference (MAD) (Equation 5). Relative Mean Absolute Difference (RMAD) is also computed to determine areas in which the percentage of change is more significant (Equation 6):

$$MAD = \frac{1}{n} \sum_{i=1}^{n} |V2.3 - V2.2| \qquad (5)$$

$$RMAD = \frac{\frac{1}{n} \sum_{i=1}^{n} |V2.3 - V2.2|}{\frac{1}{n} \sum_{i=1}^{n} V2.3} \qquad (6)$$

In the second part of the analysis, we evaluate the performance of both PERSIANN-CDR V2.2 and V2.3 over global land areas with respect to CPC unified gauge-based analysis and over the ocean with respect to TRMM 3B42 V7 at monthly and daily scales. For evaluation over land, we re-project PERSIANN-CDR V2.2 and V2.3 to 0.5° × 0.5° resolution to be consistent with the CPC unified gauge-based analysis dataset. Two commonly used statistical matrices, Correlation Coefficient (CORR) and Root Mean Square Error (RMSE) (Equation 7 & 8), are used for the evaluations. CORR is employed to measure the agreement between PERSIANN-CDR V2.3 & V2.2 with CPC unified gauge-based analysis and TRMM 3B42 V7. RMSE is widely used to measure the error in estimation of satellite-based datasets compared with observed datasets.

$$\mathrm{RMSE} = \frac{1}{n}\sqrt{\sum_{i=1}^{n}(\mathrm{Est}_i - \mathrm{Ref}_i)^2} \qquad (7)$$

$$\mathrm{CORR} = \frac{\frac{1}{n}\sum_{i=1}^{n}(\mathrm{Est}_i - \overline{\mathrm{Est}_i})(\mathrm{Ref}_i - \overline{\mathrm{Ref}_i})}{\sigma_{\mathrm{Est}}\,\sigma_{\mathrm{Ref}}} \qquad (8)$$

Where:

Est: Estimation (PERSIANN-CDR V2.2 & V2.3)

Ref: Reference (CPC unified gauge-based analysis & TRMM 3B42 V7)

4.4. Results and Discussion:

4.4.1. Changes in the PERSIANN-CDR and GPCP Monthly Analysis from V2.2 to V2.3

Comparison in spatial domain

Figures 4.1a and 1b display the mean daily precipitation estimates of PERSIANN-CDR V2.3 and GPCP V2.3 from 2009 to 2013. Both datasets show the same precipitation patterns in annual mean precipitation. This similarity is reasonable since PERSIANN-CDR is bias-adjusted with the GPCP dataset at a monthly scale. Figures 4.1c and 1d present the spatial pattern between MAD of the two versions of PERSIANN-CDR and the two versions of GPCP for that period. On average, MAD is approximately 0.07 mm/day for both versions of GPCP

and PERSIANN-CDR at a monthly scale in latitude bands of 60°N to 60°S. The changes in the mean daily precipitation rate exceed 0.3 mm/day between two versions of PERSIANN-CDR and two versions of GPCP over the North Atlantic Ocean, the North Pacific Ocean, Northern South America, Central Africa, and Indonesia. Although the absolute difference in the mean daily precipitation pattern reveals the average changes between the two versions of the datasets, it cannot demonstrate the relative importance of these changes in various regions. The spatial pattern of relative differences between the two versions of GPCP and PERSIANN-CDR is calculated to show the percentage of change in mean daily precipitation rain rate estimation for each pixel. Calculating the relative difference is important because even small differences are critical in arid regions. Figures 4.1e and 1f present the RMAD between V2.2 and V2.3 of PERSIANN-CDR and GPCP products. MAD is more significant over tropical regions and oceans between the latitudes 40°-60° in both Northern and Southern hemispheres, whereas RMAD between the two versions of PERSIANN-CDR is more noticeable over North Africa, Australia, north China, Mongolia, and southeastern Russia. These regions receive substantially less rainfall than other parts of globe; therefore, small changes in the new versions of GPCP and consequently PERSIANN-CDR V2.3 could create significant variations in RMAD.

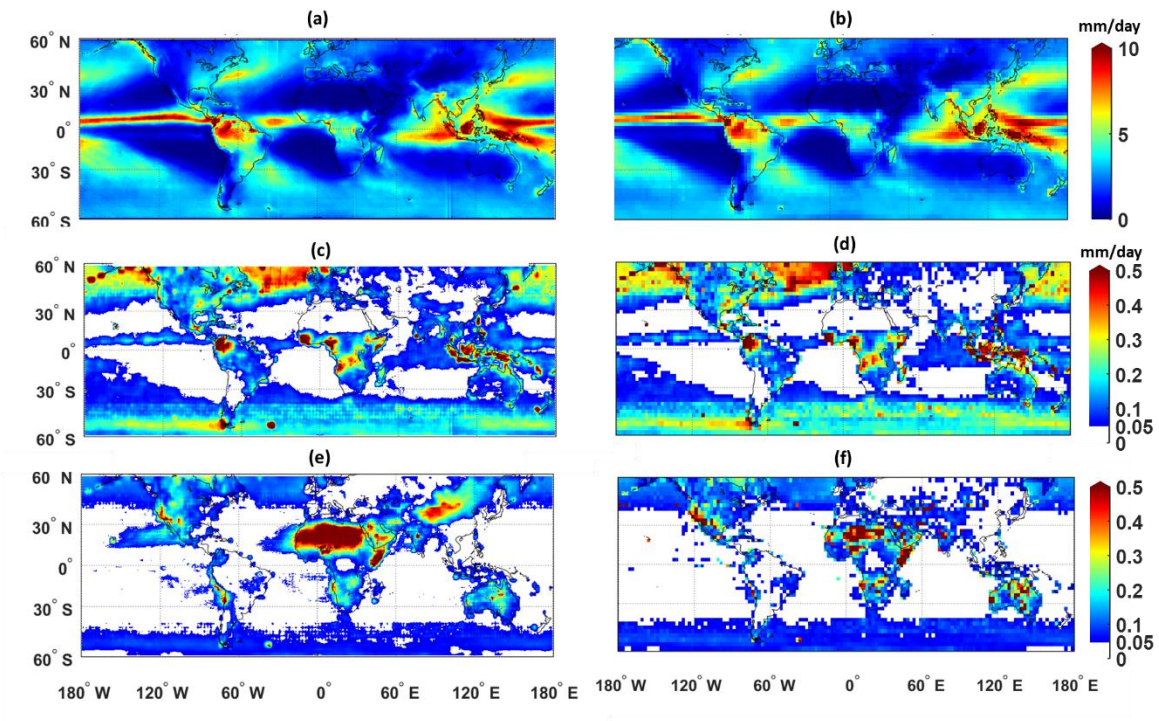

Figure 4.1 (a) PERSIANN-CDR V2.3 (mm/day) (b) GPCP V2.3 annual mean precipitation (mm/day) (c) MAD (mm/day) between PERSIANN-CDR V2.3 & V2.2 at a monthly scale (d) MAD (mm/day) between GPCP V2.3 & V2.2 at a monthly scale (e) RMAD between PERSIANN-CDR V2.3 & V2.2

4.4.2. Comparison in Temporal domain

Figure 4.2 shows the time series of differences between the mean monthly precipitation estimates for the two versions of PERSIANN-CDR (V2.2 & V2.3) and two versions of GPCP (V2.2 & V2.3) across three latitude bands. The analysis is done for tropical (20°S -20°N) and subtropical (60°S-20°S and 20°N-60°N) bands. As shown in Figure 4.2, changes between the two versions of PERSIANN-CDR (V2.2 & 2.3) and the two GPCP (V2.2 & 2.3) for tropical and subtropical zones over the land and ocean are the same, demonstrating that PERSIANN-CDR follows the GPCP in this regard . Over the ocean, the changes are more noticeable over subtropical regions, where the differences (V2.3 –V2.2) vary between 0.02 to 0.19 mm/day in Northern hemisphere, and -0.02 to 0.13 mm/day in Southern hemisphere. These findings are consistent with those in Adler et al. (2018)where they showed that corrections in the new version of GPCP result in higher rainfall accumulations over the oceans, especially in the higher latitudes and after 2003. Over oceans, most of the changes are primarily due to the sensor shifting from TOVS to AIRS for GPCP estimates, which consequently affects the PERSIANN-CDR product. Whereas GPCP V2.2 employed TOVS data for precipitation

estimates, GPCP V2.3 uses TOVS estimates before 2003 and different versions of AIRS data (based on availability of sensors) thereafter. TOVS and AIRS data are utilized for precipitation estimation at high latitudes over both land and ocean; however, changes over the land are discounted after merging with the gauge information (Adler et al. 2018). Over land, the difference between the two versions of PERSIANN-CDR and the corresponding versions of GPCP are more detectable over tropical regions than over other land regions. The changes ranged between -0.01 to 0.11 mm/day but generally positive showing an increase in precipitation estimates over the land for both PERSIANN-CDR V2.3 and their corresponding versions of GPCP. These variations are mainly related to the change from the GPCC Monitoring product in GPCP V2.2 to the GPCC V7 Full analysis in GPCP V2.3 for the time period used (2009-2013).

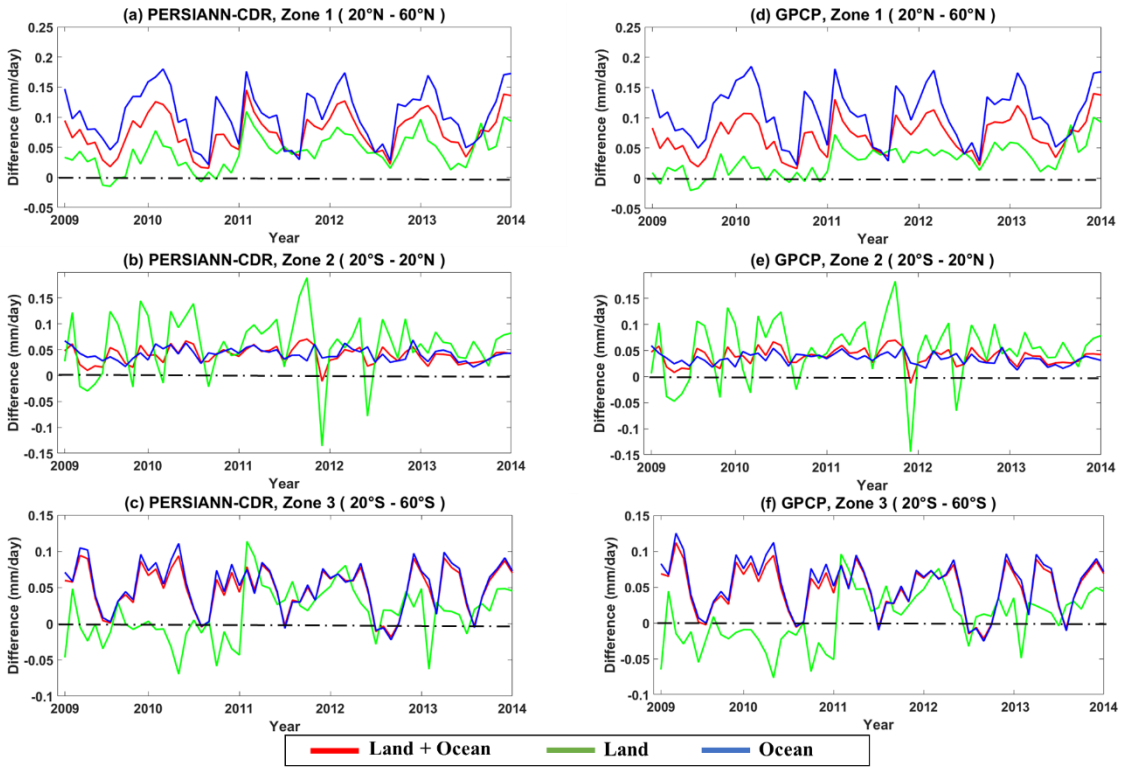

Figure 4.2 Time series of differences between precipitation estimates of PERSIANN-CDR V2.3 & V2.2 (a, b, c) and GPCP V2.3 & V2.2 (d, e, f) for three zones from 2009 to 2013.

Monthly evaluation of the two versions of PERSIANN-CDR

In this section, the performance of the two versions of PERSIANN-CDR is evaluated against the CPC gauge-based observation dataset, over the CONUS, and against TRMM 3B42 V7 over water bodies and global land areas at monthly time scales.

Evaluation over the CONUS

Figure 4.3 presents the spatial correlation and root mean squared error (mm/day) of PERSIANN-CDR V2.3 & V2.2 with respect to CPC unified gauge-based analysis over CONUS from 2009 to 2013. As mentioned in the data section, we utilized CPC unified gauge-based analysis at 0.25° × 0.25° spatial resolution for evaluation over the CONUS. Locations with higher CORR values in Figure 4.3c show where PERSIANN-CDR V2.3 is improved in terms of its correlation with CPC unified gauge-based analysis. Locations with lower RMSE values in Figure 4.3f show where PERSIANN-CDR V2.3 has a lower RMSE compared with PERSIANN-CDR V2.2. The performance of PERSIANN-CDR V2.3 is noticeably improved over the eastern and northeastern regions of United States. The highest improvement can be detected over the states of Virginia, New York, Pennsylvania, Wyoming, Idaho, and Oregon, where correlation improved by approximately 14% and RMSE decreased by 0.15 mm/day. Figure 4.4 shows the time series of average RMSE and CORR for PERSIANN-CDR V2.3 (red) and V2.2 (blue) against CPC unified gauge-based analysis over CONUS. As shown, PERSIANN-CDR V2.3 outperforms the previous version in terms of the correlation coefficient and RMSE throughout the studied period. Furthermore, the highest correlation and the lowest RMSE values are observed in June and July, when lower amounts of rainfall are observed compared to the other months of the year for both versions of PERSIANN-CDR (not shown).

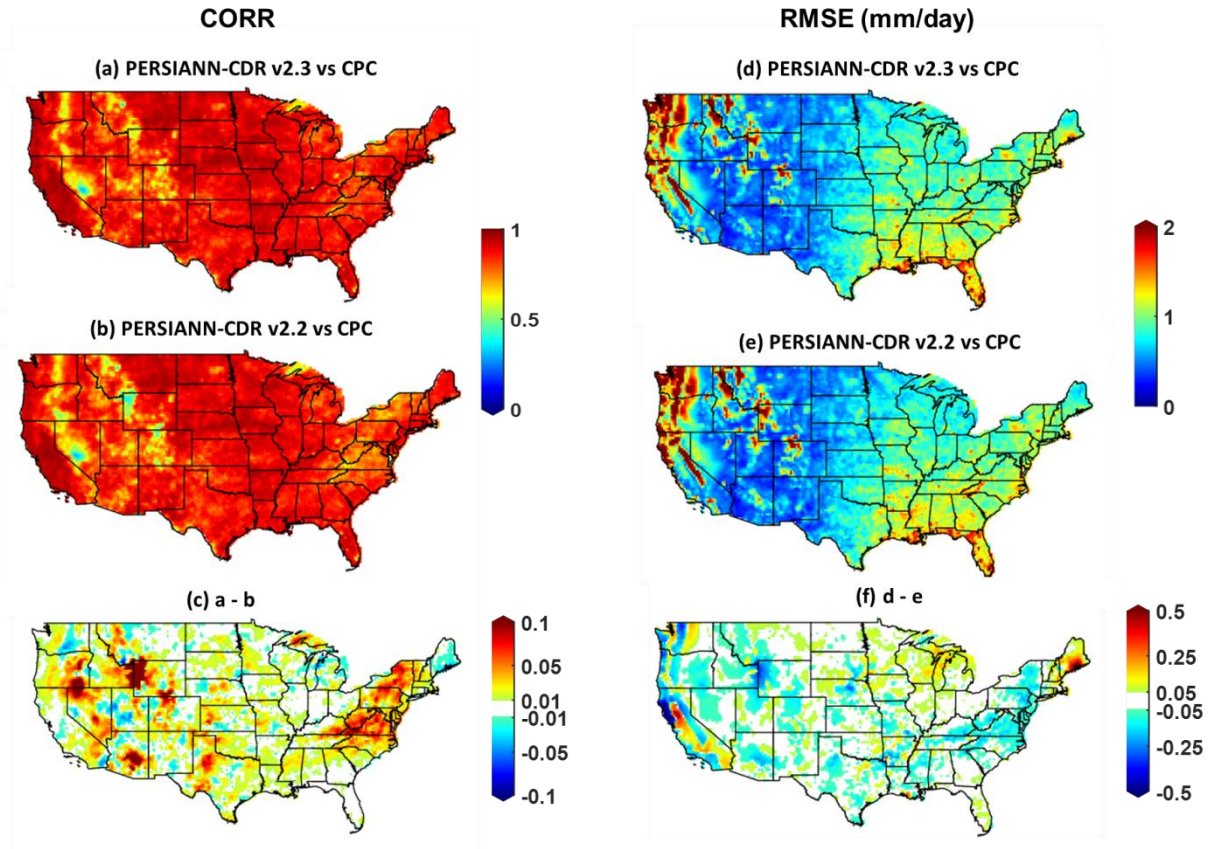

Figure 4.3 Monthly spatial CORR and RMSE (mm/day) maps for PERSIANN-CDR V2.3 (a, d) and PERSIANN-CDR V2.2 (b, e) against CPC unified gauge-based analysis and their difference (c, f) for the period of 2009 to 2013 over the CONUS.

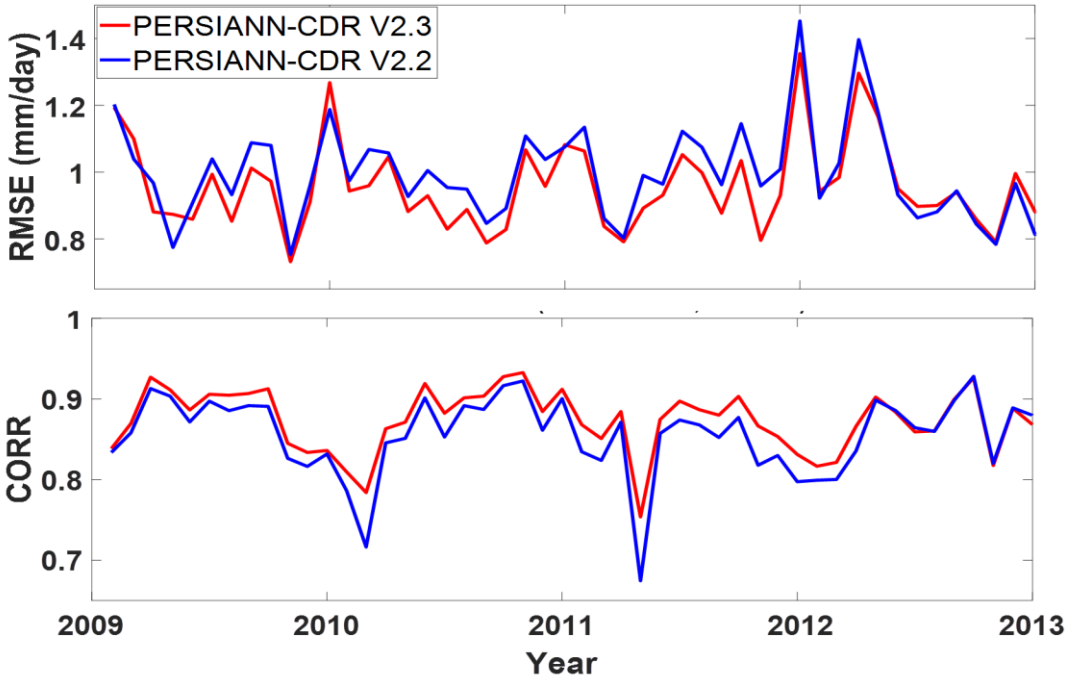

Figure 4.4 Time series of RMSE and correlation coefficient for PERSIANN-CDR V2.3 (red) and V2.2 (blue) against CPC unified gauge-based analysis for 2009-2013 over CONUS at a monthly scale.

In order to investigate the statistical behavior of various performance evaluation metrics computed for both versions of PERSIANN-CDR, frequency distribution histograms for Bias, RMSE, R99p, and R95p are presented in Figure 4.5. As can be seen in each histogram, the distribution of PERSIANN-CDR V2.3 has mean values closer to optimal (zero). The mean values closer to zero suggest that the precipitation estimation accuracy of PERSIANN-CDR V2.3 has improved compared to PERSIANN-CDR V2.2. For extreme events, both versions of PERSIANN-CDR tend to underestimate the rain rate, as the 95th (R95p) and 99th (R99p) percentiles indicate. However, the error of PERSIANN-CDR V2.3 for extreme events is less than V2.2.

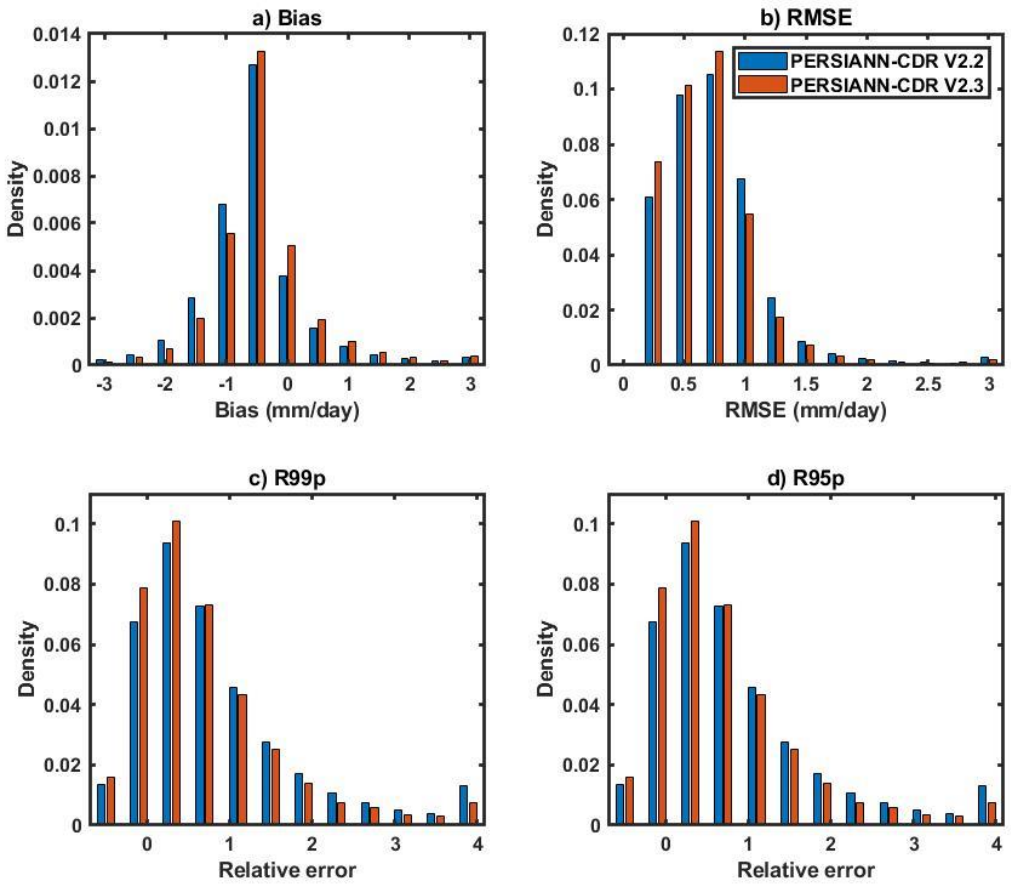

Figure 4.5 Histograms of various performance evaluation metrics, (a) Bias, (b) RMSE, (c) R99p and (d) R95p, of the two bias-adjusted versions of PERSIANN-CDR at a monthly scale over the CONUS for 2009-2013.

Evaluation Over the Globe

Figures 4.6 and 4.7 display the spatial distribution maps of CORR and RMSE for the two bias-adjusted versions of PERSIANN-CDR versus CPC and TRMM 3B42 V7 at a monthly scale over the globe, respectively. The CPC dataset at 0.5° × 0.5° spatial resolution is utilized as a gauged-based reference for comparison over global land areas. The original 0.25°PERSIANN-CDR datasets are resampled to 0.5°spatial resolution using bilinear interpolation method to match the spatial resolution of the CPC unified gauge-based analysis dataset. Moreover, due to the unavailability of gauge data over water bodies and oceans, TRMM 3B42 V7 at 0.25° spatial resolution is employed primarily for the evaluation of the two versions of PERSIANN-CDR over the ocean. As shown in Figure 4.6, the estimation accuracy of PERSIANN-CDR V2.3 is improved mostly over CONUS and Australia marked by increases in the correlation and

decreases in the RMSE with respect to CPC unified gauge-based analysis. This figure also shows that PERSIANN-CDR V2.2 estimates have a higher correlation with CPC over Africa than V2.3. However, due to inadequate number of samples used for CPC precipitation estimates over tropical Africa (Chen et al. 2008), the higher correlation in this area does not necessarily mean that the previous version of PERSIANN-CDR works better in this region. Comparison with TRMM 3B42 V7 over the ocean indicates similar performances by both versions of PERSIANN-CDR at a monthly scale. Specifically, the overall spatial CORR and RMSE of both bias-adjusted versions of PERSIANN-CDR (V 2.2 and V2.3) with TRMM 3B42 V7 is 0.78 and 1.34 mm/day, respectively. Table 4.1 summarizes the average value of the spatial maps of CORR (in black) and RMSE (in red) between the two versions of PERSIANN-CDR against the reference datasets. The table also shows that the improvement in PERSIANN-CDR V2.3 at monthly scales is more noticeable over land areas, especially over the CONUS. The CORR and RMSE between PERSIANN-CDR V2.3 and CPC unified gauge-based analysis over the CONUS have been improved by 5.2% and 2.3%, respectively. Over land globally, the CORR between PERSIANN-CDR V2.3 and CPC unified gauge-based analysis increased by 1.2%; while RMSE increased by 0.8% increases in RMSE. Evaluation over the oceans using TRMM 3B42 V7 as the reference shows that both CORR and RMSE increased by 1.25% and 0.74%, respectively.

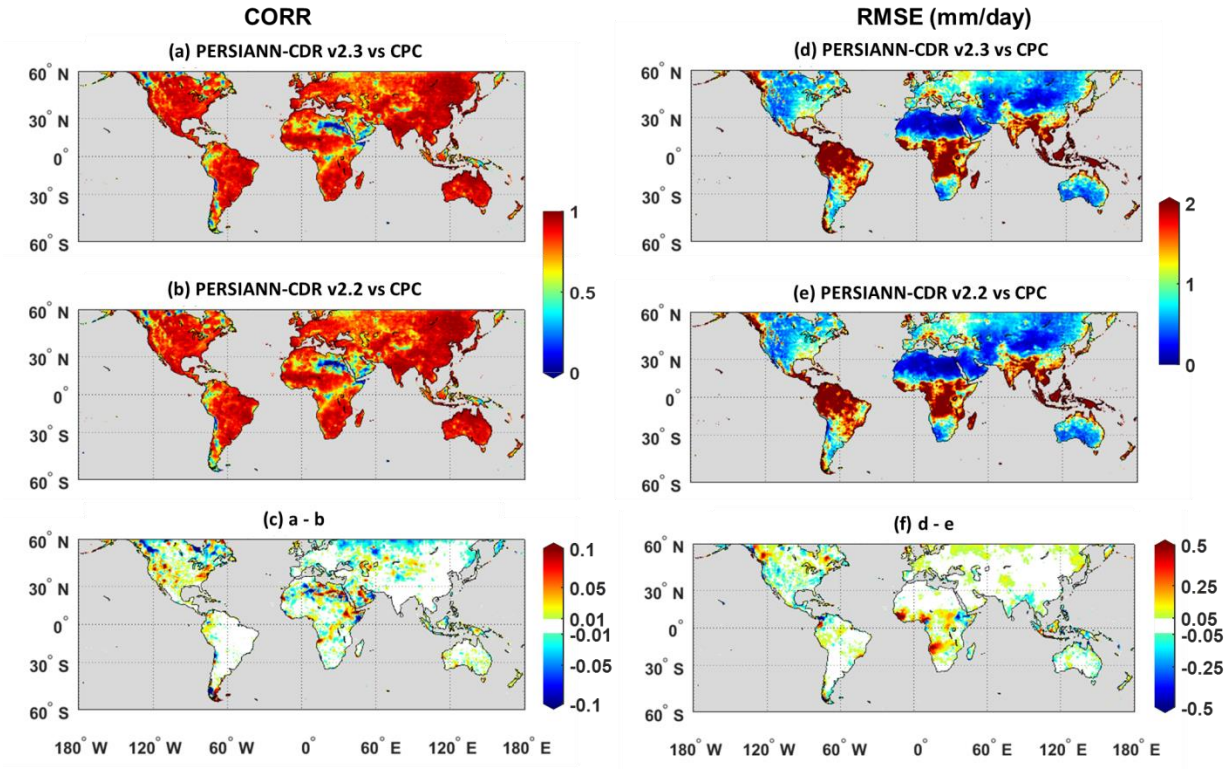

Figure 4.6 Monthly spatial CORR and RMSE (mm/day) maps over land for PERSIANN-CDR V2.3 (a, d) and PERSIANN-CDR V2.2 (b, e) against CPC unified gauge-based analysis and their differences (c, f) for the period of 2009 to 2013 over the globe.

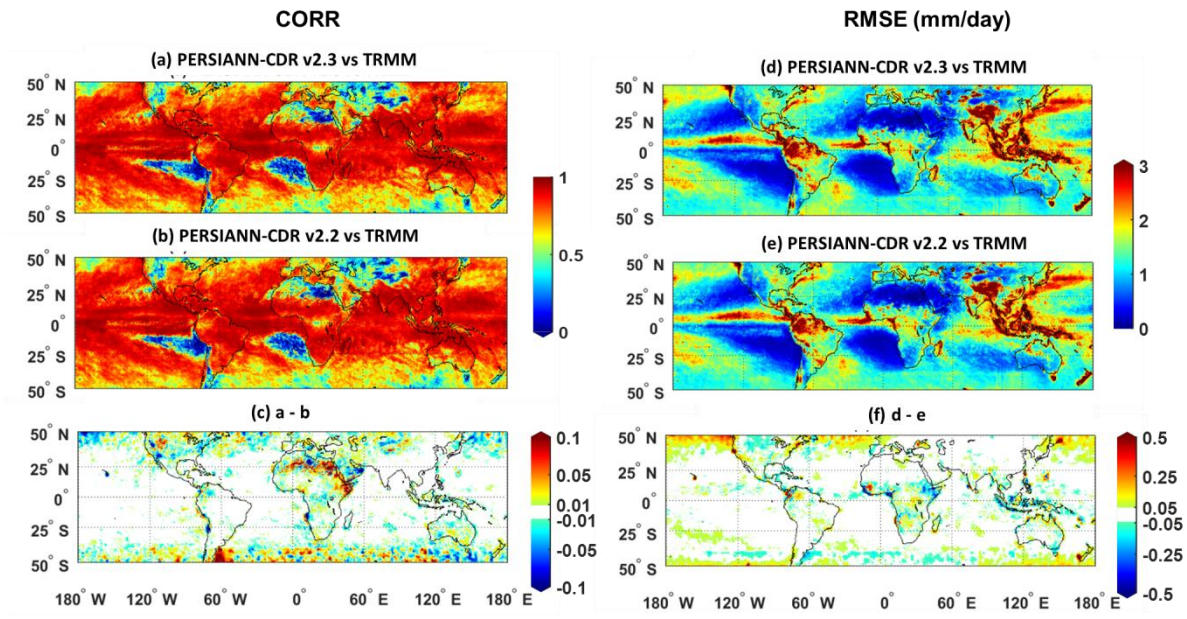

Figure 4.7 Monthly spatial CORR and RMSE (mm/day) maps for PERSIANN-CDR V2.3 (a, d) and PERSIANN-CDR V2.2 (b, e) against TRMM 3B42 V7 and their differences (c, f) for the period of 2009 to 2013 over the globe.

Table 4.1 Summary of CORR (in black) and RMSE (in red) for the two versions of PERSIANN-CDR against references (CPC unified gauge-based analysis over the CONUS and globe land & TRMM 3B42 V7 over the ocean) at a monthly scale for the period of 2009 to 2013.

Data set	CPC(CONUS)	CPC (Globe land)	TRMM(Ocean)
PERSIANN-CDR V2.3	0.87 (0.87)	0.81 (1.25)	0.79 (1.34)
PERSIANN-CDR V2.2	0.84 (0.89)	0.80 (1.24)	0.78 (1.33)
Relative Difference	5.2% (-2.3%)	1.2 % (+0.8%)	1.2% (+0.74%)

Daily evaluation of the two versions of PERSIANN-CDR

Evaluation over the CONUS

Figure 4.8 displays the maps of daily CORR and RMSE between PERSIANN-CDR V2.3 and PERSIANN-CDR V2.2 against CPC unified gauge-based analysis at a daily scale over the CONUS for the period of 2009 to 2013. Figure 4.8 indicates that the CORR between the two versions of PERSIANN-CDR and CPC unified gauge-based analysis varies geographically, with relatively higher values over the eastern states and lower values over the western states. However, RMSE shows better performance (lower values of RMSE) of PERSIANN-CDR over the western CONUS and poorer performance (higher values of RMSE) over the eastern states. This geographical pattern in CORR and RMSE is mainly due to differences in average precipitation intensity. On average, the western states receive less precipitation compared to the eastern part of the CONUS. Consequently, RMSE is affected by the amount of rain and often shows higher values over regions with higher rainfall. Note the results might have been affected by the lower number of rainfall gauges over the western CONUS that were used in the CPC unified gauge-based analysis gridded product. Based on Figure 4.8c and Figure 4.8f, a small improvement in the new bias-adjusted version of PERSIANN-CDR (V2.3) can be detected over the central United States, where CORR increased and RMSE is constant.

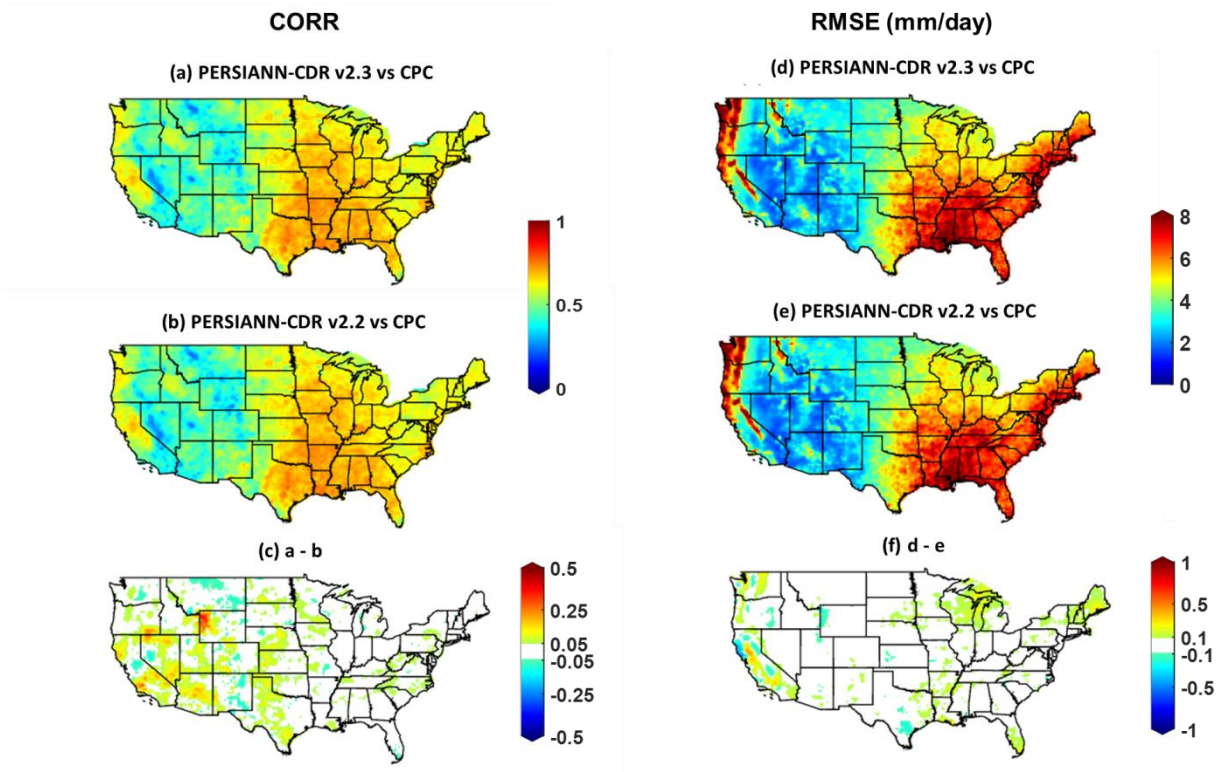

Figure 4.8 Daily spatial CORR and RMSE (mm/day) maps for PERSIANN-CDR V2.3 (a, d) and PERSIANN-CDR V2.2 (b, e) against CPC and their differences (c, f) for the period of 2009 to 2013 over the CONUS.

Evaluation over the Globe

We use TRMM 3B42 V7 for daily comparison of the two versions of PERSIANN-CDR over both land and oceans. PERSIANN-CDR and TRMM 3b42 v7 give the daily accumulated rainfall starting at 22:30Z of the previous day to 22:30Z of the day named. The reason that we do not use global CPC unified gauge-based analysis is that EOD definition varies from one country to another country. This can create inconsistency in daily evaluation since PERSIANN-CDR has a unique EOD definition but CPC unified gauge-based analysis does not.. Figure 4.9 illustrates the CORR and RMSE between TRMM 3B42 V7 and the two versions of PERSIANN-CDR over the land and oceans. The correlation between PERSIANN-CDR and TRMM 3B42 V7 shows a strong correspondence between these two datasets in estimating the daily precipitation rate. This is reasonable since the information of IR imagery has been used in both TRMM 3B42 V7 and PERSIANN-CDR algorithms for estimating 3-hourly rain rates. That

said, PERSIANN-CDR relies mainly on IR data, whereas TRMM combines IR and PMW data. Furthermore, PERSIANN-CDR is bias-adjusted with the GPCP dataset; and both GPCP and TRMM apply relatively similar procedures with different initial inputs for their precipitation estimates (Sadeghi 2018). Both the GPCP and TRMM algorithms utilize the more accurate rain rate estimates from passive microwave data captured by low-orbit satellites to adjust the more frequent geosynchronous-orbit satellite infrared information. TRMM 3B42 V7 inserts the microwave estimates into the individual precipitation maps, while GPCP only uses microwave estimates in monthly calibrations. Then in both products, the combined satellite-based products are bias-adjusted with rain gauge analysis. Particularly over low latitudes, one can see a higher correlation between both versions of PERSIANN-CDR against TRMM. This is mainly due to using SSMI microwave observations in both TRMM 3B42 V7 and GPCP V2.2 algorithms for latitude between 40° and 40°N. The statistical indices including CORR and RMSE between the two versions of PERSIANN-CDR and references at daily scale over the CONUS and the globe are summarized in Table 4.2. The changes in both CORR and RMSE between PERSIANN-CDR V2.2 and V2.3 are modest. A slight improvement can be seen in CORR between PERSIANN-CDR V2.3 as opposed to PERSIANN-CDR V2.2 against TRMM 3B42 V7 over the ocean. However, the RMSE has increased for PERSIANN-CDR V2.3 against TRMM 3B42 V7.

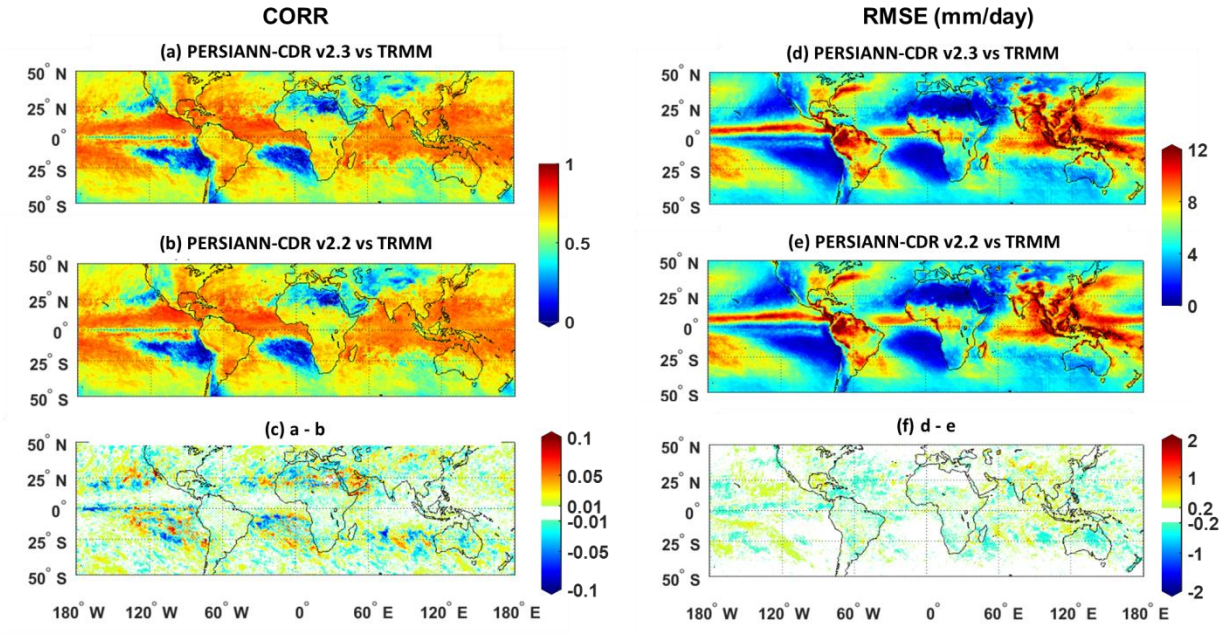

Figure 4.9 Daily spatial CORR and RMSE (mm/day) maps for PERSIANN-CDR V2.3 (a, d) and PERSIANN-CDR V2.2 (b, e) against TRMM 3B42 V7 and their difference (c, f) for the period of 2009 to 2013 over the globe.

Table 4.2 Summary of CORR (in black) and RMSE (in red) for the two versions of PERSIANN-CDR against CPC unified gauge-based analysis over the CONUS (0.25° x 0.25° spatial resolution) and TRMM 3B42 V7 (0.25° x 0.25° spatial resolution) over the global land mass and

	CPC(CONUS)	TRMM (land)	TRMM(Ocean)
PERSIANN-CDR V2.3	0.57 (4.58)	0.56 (5.65)	0.63 (5.63)
PERSIANN-CDR V2.2	0.56 (4.58)	0.55 (5.65)	0.62(5.60)
Relative Difference	1% (0%)	1% (0%)	1.6% (0.5%)

4.5. Conclusions

Historical precipitation estimates from PERSIANN-CDR have been widely used for climatological studies over the globe. Accurate precipitation information from PERSIANN-CDR could contribute to meteorological, hydrological, and water resources management applications. Recently, GPCP has been updated to version 2.3 by applying the adjustments in cross-calibration of satellite data inputs and updating the gauge analysis. In this study, we compared the PERSIANN-CDR product constructed with the GPCP V2.3 with the previous

version PERSIANN-CDR V2.2for the period between 2009 and 2013. First, the differences between the two versions of PERSIANN-CDR (V2.3 & V2.2) and GPCP (V2.3 & V2.2) were described. We utilized Mean Absolute Difference (MAD) and Relative Mean Absolute Difference (RMAD) for tracking the changes between the latest two versions of both PERSIANN-CDR and GPCP. Comparing PERSIANN-CDR V2.2 & V2.3 over ocean areas at a monthly scale indicates that the changes in MAD are more than 0.25 mm/day at latitude bands between 40° to 60° in northern and southern hemisphere after 2009. The increase in PERSIANN-CDR's estimates over the oceans is mainly due to the adjustments implemented on the GPCP V2.3 dataset. These adjustments include improvement in cross-calibration of precipitation from TOVS to AIRS since January 2003 and from SSMI to SSMIS after 2009. Over land areas, changes in MAD were more significant over the tropical region, while the highest percentage of changes (RMAD) were detectable in other regions of the globe including North Africa, Australia, North China, Mongolia, and Southeastern Russia. The main reasons for changes in MAD and RMAD over the global land areas were: i) increasing the gauge samples over the entire period of the record, and ii) updating from the GPCC Monitoring product to the GPCC Full product.

The two versions of PERSIANN-CDR were evaluated over CONUS and global land areas and oceans using the CPC unified gauge-based analysis and TRMM 3B42 V7. Over CONUS, results showed that on average the performance of PERSIANN-CDR V2.3 has improved in terms of RMSE and CORR in both daily and monthly scales. Between 2009 and 2013, RMSE at monthly (and daily) decreased by 2.3% (and 0%) and the CORR increased by 5.1 % (and 1%) compared to PERSIANN-CDR V2.2. Improvements in terms of RMSE and CORR were evident over various states (e.g., Virginia, New York, Pennsylvania, and Oregon). Over global land areas, results indicated that the performance of PERSIANN-CDR V2.3 at monthly and daily scale is better than the previous version, especially over CONUS and Australia. The performance evaluation of two versions of PERSIANN-CDR against TRMM 3B42 V7 over the oceans revealed a slight increase in both CORR and RMSE. CORR improved by 1.6 % (and 1.2%) and RMSE has increased by 0.74 % (and 0.5%) in a monthly (and daily) scale.

In summary, the analyses show that the corrections and adjustments in GPCP V2.3 were successfully translated onto PERSIANN-CDR V2.3. The results indicate that most of the

changes in amount of rainfall are detectable over tropical regions and oceans between the latitudes 40°-60° in both Northern and Southern hemispheres. The changes in amount of rainfall improve the accuracy of PERSIANN-CDR V2.3 over the most regions of the globe, especially over the CONUS and Australia. Although these corrections and adjustments are small, they are crucial when applied to large areas, particularly over oceans and arid regions. In addition, these improvements are important for investigating the changes in inter-annual rainfall variabilities (e.g. due to El Niño—Southern Oscillation (ENSO)).

CHAPTER FIVE:

PERSIANN-CCS-CDR, A 3-HOURLY 0.04° GLOBAL PRECIPITATION CLIMATE DATA RECORD FOR HEAVY PRECIPITATION STUDIES

The contents of Chapter 5 are published in the Journal of Scientific Data

Citation: Sadeghi, M., Nguyen, P., Naeini, M. R., Hsu, K., Braithwaite, D., & Sorooshian, S. (2021). PERSIANN-CCS-CDR, a 3-hourly 0.04° global precipitation climate data record for heavy precipitation studies. Scientific Data, 8(1), 1-11.

5.1. Abstract

Accurate long-term global precipitation estimates, especially for heavy precipitation rates, at fine spatial and temporal resolutions is vital for a wide variety of climatological studies. Most of the available operational precipitation estimation datasets provide either high spatial resolution with short-term duration estimates or lower spatial resolution with long-term duration estimates. Furthermore, previous research has stressed that most of the available satellite-based precipitation products show poor performance for capturing extreme events at high temporal resolution. Therefore, there is a need for a precipitation product that reliably detects heavy precipitation rates with fine spatiotemporal resolution and a longer period of record. Precipitation Estimation from Remotely Sensed Information using Artificial Neural Networks-Cloud Classification System-Climate Data Record (PERSIANN-CCS-CDR) is designed to address these limitations. This dataset provides precipitation estimates at 0.04° spatial and 3-hourly temporal resolutions from 1983 to present over the global domain of 60°S to 60°N. Evaluations of PERSIANN-CCS-CDR and PERSIANN-CDR against gauge and radar observations show the better performance of PERSIANN-CCS-CDR in representing the spatiotemporal resolution, magnitude, and spatial distribution patterns of precipitation, especially for extreme events.

5.2. Materials

5.2.1. Input data

Gridded satellite infrared data (GridSat-B1)

In 1983, the National Oceanic and Atmospheric Administration (NOAA)/National Climatic Data Center (NCDC) began collecting meteorological geostationary satellite data through the International Satellite Cloud Climatology Project (ISCCP) (Knapp 2008). The ISCCP B1 dataset provides global IR brightness temperature data with 10-km spatial and 3-hourly temporal resolution for the period from 1979 to present. The ISCCP B1 dataset consists of observations from different sensors launched by different countries, including United States [for the Geostationary Operational Environmental Satellite (GOES) series], Japan [for the Japanese Geostationary Meteorological Satellite (GMS) series and Multi-functional Transport Satellite (MTSAT)], Europe [for the European Meteorological satellite (Meteosat) series], and China [for the Chinese Fen-Yung 2 (FY2) series]. The gridded satellite (GridSat-B1) dataset

isderived from the ISCCP B1 dataset and provides near-global data with 0.07° spatial and 3-hourly temporal resolution from 1980 to present. The GridSat-B1 dataset is available via noaa.gov[1]. More information can be found in Knapp et al. (2011).

NOAA Climate Prediction Center (CPC-4km) IR product

The NOAA Climate Prediction Center (CPC) globally merged IR product, which is referred to as CPC-4km, was developed to provide near-real time data for monitoring global precipitation (Janowiak et al. 2001).This dataset offers near-global (60°N-60°S) IR data with 4-km spatial and half-hourly temporal resolutions from the present international constellation of operational geostationary meteorological satellites for the period from 2000 to present. The CPC-4km product is comprised of IR observations from several international GEO satellites, including Meteosat-5 and Meteosat-7, GMS, and GOES. CPC-4km data is publicly accessible through the Climate Prediction Center webpage[2].

Global Precipitation Climatology Project (GPCP V2.3)

GPCP is part of the Global Energy and Water Cycle Exchanges (GEWEX) project under the World Climate Research Program (WCRP) (Huffman et al. 1997). This product provides monthly precipitation at a 2.5° x 2.5° spatial resolution by merging different satellite-based estimation information (passive microwave/infrared) along with precipitation gauge networks from GPCC. A comprehensive description of GPCP monthly v2.3 data inputs and the merging process can be found in (Adler et al. 2018). The GPCP dataset is available for public use through the Earth System Science Interdisciplinary Center (ESSIC) and Cooperative Institute for Climate and Satellites (CICS), University of Maryland College Park[3].

5.2.2. Reference Data

CPC Global Unified Gauge-Based Analysis of Daily Precipitation

The National Oceanic and Atmospheric Administration (NOAA) Climate Prediction Center (CPC) provides the CPC Global Unified Gauge-Based Analysis of Daily Precipitation dataset

[1] https://www.ncdc.noaa.gov/gridsat/gridsat-index.php
[2] https://www.cpc.ncep.noaa.gov/products/global_precip/html/web.shtml
[3] http://gpcp.umd.edu

(Chen et al. 2008). This dataset offers global precipitation estimates at 0.5° x 0.5° spatial and daily temporal resolutions from 1979 to present. The daily precipitation reports of roughly 30,000 stations from different sources across global land areas have been collected and quality controlled by the NOAA Climate Prediction Center. The data sources include Global Telecommunication System (GTS), the CPC unified daily gauge datasets over the CONUS, Cooperative Observer Network (COOP), and other national and international agencies. A comprehensive description of this CPC dataset and the interpolation algorithm that is used can be found in Xie et al. (2007). The CPC Global Unified Gauge-Based Analysis of Daily Precipitation dataset is accessible to the public through (ftp://ftp.cdc.noaa.gov/Datasets).

NCEP Stage IV QPE Data

NCEP Stage IV QPE is widely considered as the best long-term gridded rain accumulation dataset over the CONUS due to its extensive quality control procedures (Smalley et al. 2014). This product merges the national Weather Surveillance Radar-1988 Doppler (WSR-88D) network of ground radars and ground-based rain gauge observations (Yilmaz et al. 2005; Lin and Mitchell 2005). NCEP Stage IV provides precipitation observations at 0.04° (4 km) spatial resolution and hourly, 6 hourly, and 24 hourly temporal resolution. For this study, daily NCEP Stage IV observations were obtained from the distribution website[1] and used as the benchmark for evaluating the remotely sensed precipitation datasets over the CONUS.

Precipitation Estimation from Remotely Sensed Information using Artificial Neural Networks–Climate Data Record (PERSIANN-CDR)

PERSIANN-CDR is a satellite-based precipitation estimation product that provides more than three decades (from 1983 to present) of daily precipitation estimates at 0.25° × 0.25° spatial resolution for the 60°S–60°N latitude band(Ashouri et al. 2015). PERSIANN-CDR utilizes the archive of infrared brightness temperature from GridSat-B1 (Knapp et al. 2011; Rossow and Duenas 2004) as the input of the PERSIANN algorithm. Then the rainfall estimates of the PERSIANN algorithm are bias corrected using the monthly Global Precipitation Climatology Project (GPCP) version 2.3 product at 2.5° × 2.5° spatial resolution (Sadeghi 2018). This

[1] http://www.emc.ncep.noaa.gov/mmb/ylin/pcpanl/stage4/

dataset is available for public access through the NOAA National Centers for Environmental Information (NCEI) Program[1] and through the Center for Hydrometeorology and Remote Sensing (CHRS) Data Portal[2]. Additional details about the PERSIANN-CDR algorithm can be found in Ashouri et al. (2015) and Sadeghi et al.(2019a)

5.3. Methodology

5.3.1. PERSIANN-CCS-CDR description

PERSIANN-CCS-CDR is generated beginning with rain rate (RR) outputs from the PERSIANN-CCS model. The IR inputs used by PERSIANN-CCS to generate RR outputs come from two distinct periods: From 1983 through February 2000 GridSat-B1 IR data are used but from March 2000 to the present CPC-4km IR data are available and those are used instead. All IR inputs are resampled to 0.04° resolution before input. The GridSat-B1 images are every 3 hours and the output RR data are mm/hr rain rates every 3 hours. The input CPC-4km images are available every 30-minutes, so the output RR data are mm/hr rain rates every 30-minutes.

In the second stage of the PERSIANN-CCS-CDR model the 0.04° RR grids, after a threshold (thd) of 0.1 is applied, are aggregated to monthly temporal resolution for comparison to monthly GPCP v2.3 precipitation. The monthly PERSIANN-CCS RR accumulations (mm/month) at 0.04° spatial resolution must be aggregated then to 2.5° using the bilinear method to match GPCP v2.3.

$$R_{\mathrm{Cum-PERSIANN-CCS}}(i', j') = \sum^{nd} \sum^{nh} (\sum \sum [r_{\mathrm{PERSIANN-CCS}}(i, j) \geq thd]) \qquad \text{(Eq.1)}$$

In this equation, $R_{Cum-PERSIANN-CCS}$ and $r_{PERSIANN-CCS}$ are the monthly 2.5° aggregated PERSIANN-CCS estimates and 30min/3-hourly PERSIANN-CCS estimates at 0.04° spatial resolution, respectively. The i and j represent the latitude and longitude of the 30min/3-hourly PERSIANN-CCS at 0.04° × 0.04° spatial resolution. Similarly, i' and j' are the latitude and longitude of the aggregated PERSIANN-CCS at 2.5° × 2.5° resolution. The nd and nh are the number of days and the number of 30min/3-hourly PERSIANN-CCS samples in each day,

[1] https://www.ncdc.noaa.gov/cdr
[2] http://chrsdata.eng.uci.edu/

respectively. Due the nature of neural network algorithms, some fractions of non-raining pixels are falsely associated with light precipitation. As mentioned, we applied a threshold (thd) of 0.1 mm/day in order to eliminate the falsely assigned light rain rates with no rainfall.

In the next stage, the bias-adjustment weights for each monthly 2.5° grid cell are calculated as follows:

$$w(i',j') = R_{GPCP}(i',j') / R_{Cum-PERSIANN-CCS}(i',j'),\ 0 \le w \le 2.5, \quad \text{(Eq.2)}$$

where R_{GPCP} is the monthly rain rate of GPCP for a given pixel.

The 2.5° weights grids must then be bilinearly interpolated back to 0.04° spatial resolution for the next stage. In the final 2 stages, the 0.04° monthly weights are applied to each original input RR grid available. Each RR grid, either every 3 hours RR or every 30-minute RR depending on the IR data source, is multiplied by the weight.

$$PERSIANN - CCS - CDR\ (i,j) = w(i,j) * r_{PERSIANN-CCS}(i,j) \quad \text{(Eq. 3)}$$

Finally, the bias-adjusted RR files are aggregated to produce the final PERSIANN-CCS-CDR product, consisting of an accumulation at 3-hourly resolution and 0.04° spatial resolution. At this last stage the RR mm/hr are limited by a historical maximum rain rate for each 0.04° grid location and each calendar month for seasonal and geographical specificity.

5.3.2. Performance Measurements

To evaluate the performance of PERSIANN-CDR and PERSIANN-CCS-CDR against the Stage IV and CPC datasets, Root Mean Squared Error (RMSE), Correlation Coefficient (CC), and Mean Absolute Error (MAE), are calculated by the following equations (equations 4-5):

$$RMSE = \frac{1}{n}\sqrt{\sum_{i=1}^{n}(Sim_i - Ref_i)^2} \quad \text{(Eq. 4)}$$

$$CC = \frac{\frac{1}{n}\sum_{i=1}^{n}(Sim_i - \overline{Sim_i})(Ref_i - \overline{Ref_i})}{\sigma_{Sim}\,\sigma_{Ref}} \quad \text{(Eq. 5)}$$

where:

Sim: Simulation (PERSIANN-CDR, PERSIANN-CCS-CDR)

Ref: Reference observations (Stage IV and CPC)

5.4. Results and Discussion

5.4.1. Performance Evaluation for extreme events over the Globe and the CONUS

Figure 1 presents the performance of PERSIANN-CDR and PERSIANN-CCS-CDR against CPC in detecting the 99th percentile indices (RR99p) of the daily precipitation on wet days (days with daily precipitation >=1 mm) for the period of 1983 to 2019 over global land areas. The CPC unified gauge-based analysis dataset at 0.5° × 0.5° spatial resolution is used as a gauged-based reference for comparing and calculating the continuous evaluation indices including CC, RMSE, and MSE. The original 0.25° PERSIANN-CDR and 0.04° PERSIANN-CCS-CDR datasets are resampled to 0.5° spatial resolution using the bilinear interpolation method to match the spatial resolution of the CPC dataset. Then, the 99th percentile of daily precipitation of CPC, PERSIANN-CDR, and PERSIANN-CCS-CDR datasets were calculated for each pixel using the whole period of record (1983-2019). Clearly in Figure 5.1, PERSIANN-CCS-CDR offers more accuracy for the intensity of rain rates in comparison to PERSIANN-CDR in terms of estimating extreme events. PERSIANN-CDR tends to underestimate heavy precipitation over the globe, while PERSIANN-CCS-CDR provides a more realistic representation of heavy precipitation. Figure 5.1 also reveals that PERSIANN-CCS-CDR's estimates have both higher correlation and lower RMSE with CPC observations compared to PERSIANN-CDR over the globe. The correlation between PERSIANN-CCS-CDR and CPC unified gauge-based analysis over land is increased by 15%, and the RMSE decreased by 28%, respectively, versus PERSIANN-CDR.

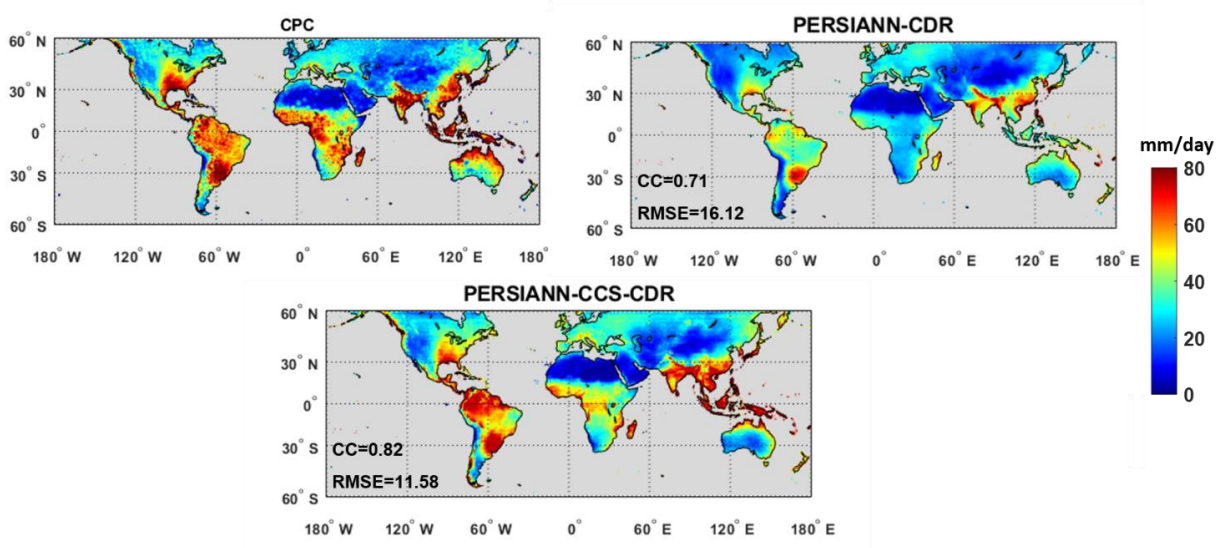

Figure 5.1 Evaluation of PERSIANN-CDR and PERSIANN-CCS-CDR against CPC for the 99th percentile of daily precipitation on wet days (days with daily precipitation >=1 mm) for the period of 1983-2019.

Figure 5.2 shows the performance of PERSIANN-CDR and PERSIANN-CCS-CDR against Stage IV, as a reference, in capturing the RR99p of daily precipitation at 0.25° × 0.25° spatial resolution for the period of 2003 to 2019. The PERSIANN-CCS-CDR estimates were resampled to 0.25° spatial and daily temporal resolution using the bilinear method for the comparison. As shown in Figure 5.2, high values of RR99p appear in the southeastern part of the United States. In general, PERSIANN-CCS-CDR captures the magnitude and the pattern of RR99p better than PERSIANN-CDR compared to radar observations, especially over the southeastern part of the CONUS. Although PERSIANN-CDR shows similar patterns to Stage IV, it underestimates magnitudes of precipitation. On the other hand, PERSIANN-CCS-CDR captures the volume of the extreme events fairly well. The disagreement between PERSIANN-CCS-CDR and Stage IV radar observations is mainly over the northern part of the United States, including Minnesota, Iowa, and Michigan, where most values are overestimated. According to Figure 5.2, the spatial correlation, RMSE, and MSE of PERSIANN-CDR and PERSIANN-CCS-CDR with respect to CPC unified gauge-based analysis indicate that PERSIANN-CCS-CDR has better performance than PERSIANN-CDR for extreme event

analyses in climatological applications. CC and RMSE of PERSIANN-CCS-CDR estimates with Stage IV are improved by 25% and 31%, in comparison to PERSIANN-CDR, respectively.

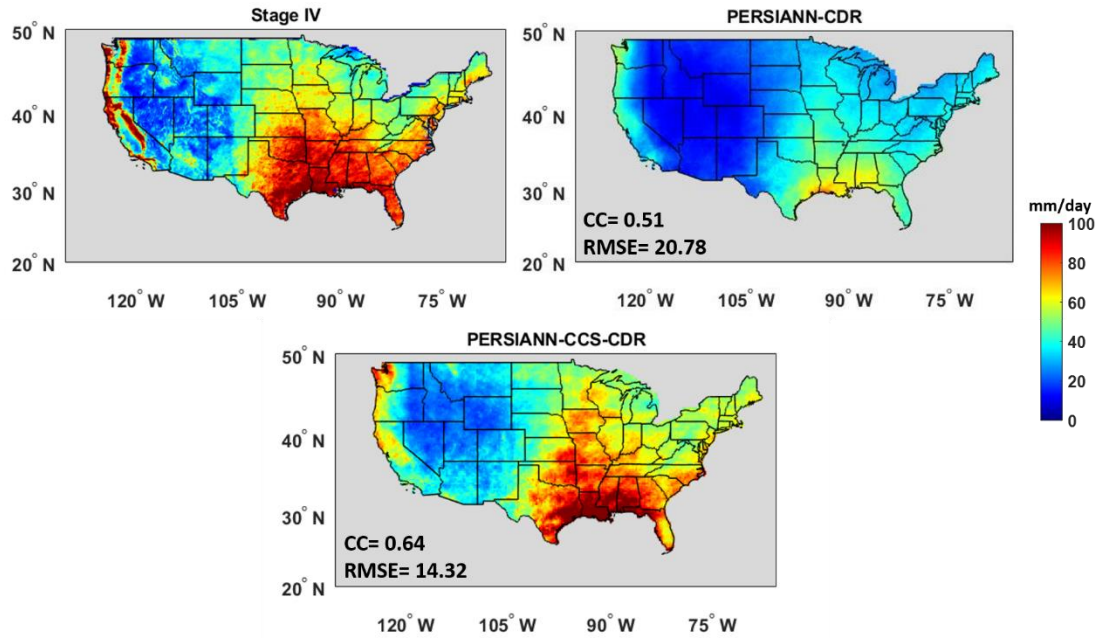

Figure 5.2 Evaluation of PERSIANN-CDR and PERSIANN-CCS-CDR against Stage IV for the 99th percentile of daily precipitation on wet days (days with daily precipitation >=1 mm) for the period of 2003-2019.

5.4.2. Case Studies

To further investigate the performance of PERSIANN-CCS-CDR estimates with Stage IV as a reference, the following verification studies have been done at different temporal and spatial resolutions. The first case study targets Hurricane Harvey in 2017 and investigates the performance of the PERSIANN-CCS-CDR estimates over the Southeastern United States at daily temporal resolution. The second case study is related to the flood that occurred in Louisiana in 2016 and evaluates the performance of the developed product at the watershed scale for 3-hourly and daily temporal scales.

Hurricane Harvey, August 2017 (Daily Assessment)

During August 25-30, 2017, Hurricane Harvey hit the Southeastern regions of the United States, including Southeast Texas, and Louisiana. Hurricane Harvey is classified as a Category 4 storm that caused catastrophic damages. This storm is referred as one of the costliest

extreme precipitation events that struck in the history of the United States (Amadeo 2018). According to the National Hurricane Center, the total damage is estimated to be more than $125 billion and it is confirmed that there were more than 80 fatalities (Van Oldenborgh et al. 2017). In this section, PERSIANN-CCS-CDR and PERSIANN-CDR are evaluated against Stage IV as the reference at 0.25° spatial resolution and daily temporal resolution. The original 0.04° × 0.04° spatial resolution of Stage IV and PERSIANN-CCS-CDR datasets were resampled to 0.25° × 0.25° spatial resolution using bilinear interpolation to match the spatial resolution of PERSIANN-CDR. Then the 3-hourly estimates of PERSIANN-CCS-CDR were aggregated to obtain daily scale to match the PERSIANN-CDR estimates in temporal resolution. Figure 5.3 presents daily values for extreme precipitation that occurred from August 27 to 30, 2017 using Stage IV data and PERSIANN-CDR and PERSIANN-CCS-CDR estimates. As shown in Figure 5.3, PERSIANN-CCS-CDR captures both the spatial pattern and the intensity of rainfall better than PERSIANN-CDR. For more exploration of the accuracy of estimation, the scatter plots for PERSIANN-CDR and PERSIANN-CCS-CDR versus Stage IV are presented and the relevant statistics are calculated in Figure 5.3. In general, PERSIANN-CCS-CDR outperforms PERSIANN-CDR for CC and FAR. As shown in Figure 5.3, both PERSIANN-CDR and PERSIANN-CCS-CDR show a high correlation with Stage IV radar. The correlation for PERSIANN-CDR and PERSIANN-CCS-CDR with Stage IV are 0.79 and 0.84, respectively. RMSE improves from 20 mm/day to 18.7 mm/day for PERSIANN-CCS-CDR estimates compared to PERSIANN-CDR. Furthermore, PERSIANN-CDR underestimates intense precipitation, while PERSIANN-CCS-CDR performs relatively well. As can be seen, both Stage IV and PERSIANN-CCS-CDR show rain rates with more than 500 mm/day that occurred over some pixels. However, PERSIANN-CDR does not show any value more than 195 mm/day and underestimates the rain rates.

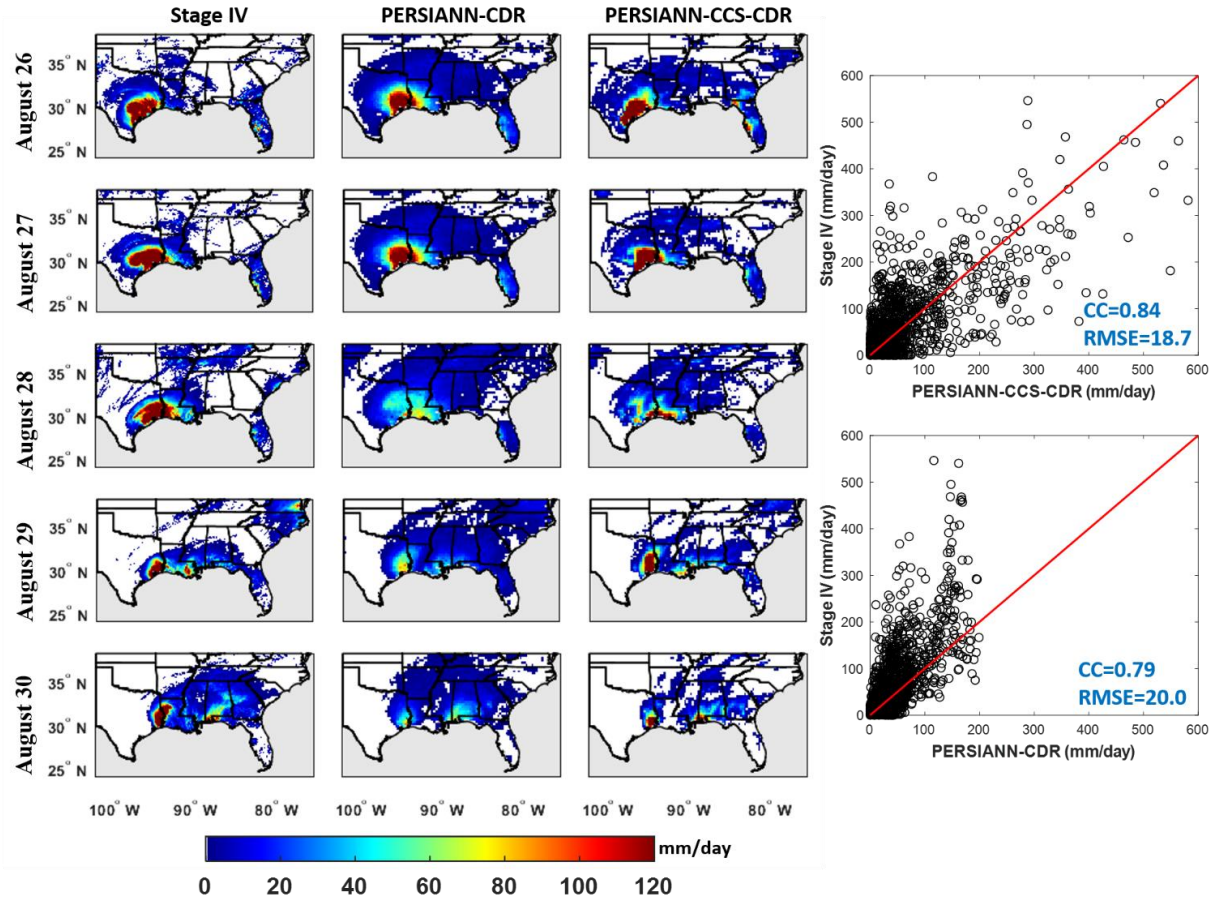

Figure 5.3 The spatial precipitation evolution of Hurricane Harvey for the period from August 26-30, 2017 from (a) Stage IV, (b) PERSIANN-CDR, and (c) PERSIANN-CCS-CDR

Louisiana Flood, August 12, 2016 (3-hourly, and Daily Assessment)

In August 2016, an intense rainfall event occurred over the state of Louisiana with more than 30 inches (760 millimeters) of rainfall in some locations, resulting in a catastrophic flood[1]. This event led to more than a dozen deaths and more than $30 million in damages[2]. The performances of PERSIANN-CDR and PERSIANN-CCS-CDR for this flood are evaluated against Stage IV radar observations (Figure 5.4). Figure 5.4 b shows Stage IV rainfall

[1] https://www.usgs.gov/news/
[2] https://www.cnn.com/

estimates at 0.04° × 0.04° spatial resolution on August 12, 2016. Figure 5.4 c and figure 5.4 d shows PERSIANN-CDR estimates (with a 0.25° × 0.25° spatial resolution) and PERSIANN-CCS-CDR estimates (with a 0.04° × 0.04° spatial resolution), respectively. This figure demonstrates two attractive aspects of the PERSIANN-CCS-CDR dataset in comparison to the PERSIANN-CDR dataset for climatological studies: 1) PERSIANN-CCS-CDR performs better than PERSIANN-CDR for this extreme event by capturing the volume of heavy rain over the southwest area of the watershed as shown. 2) The high temporal resolution of PERSIANN-CCS-CDR is another feature which is beneficial for studying the diurnal cycle and is essential for rainfall-runoff modeling studies. These two features of PERSIANN-CCS-CDR make this new dataset attractive for integrating its high spatiotemporal resolution estimates into hydrological and land-surface models for flood forecasting (or other applications that are sensitive to heavy precipitation rates).

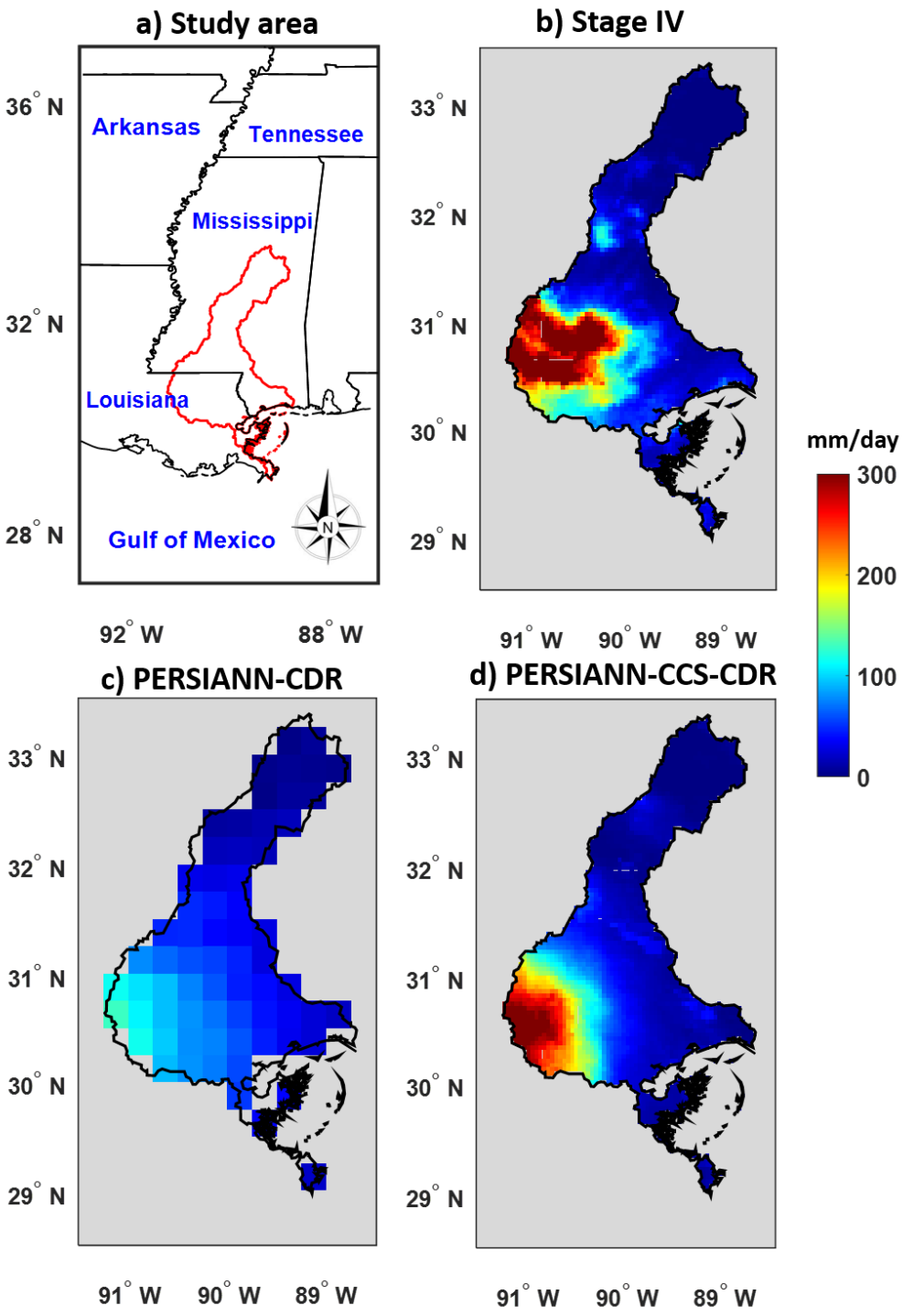

Figure 5.4 Evaluation of daily PERSIANN-CDR and PERSIANN-CCS-CDR against Stage IV for the Louisiana flood of Aug. 12, 2016.

Figure 5.5 illustrates the evolution of the precipitation that occurred on August 12, 2016 based on Stage IV and PERSIANN-CCS-CDR estimates at 3-hourly temporal and 0.04° × 0.04°

spatial resolutions. The hourly estimates of Stage IV data are aggregated to a 3-hourly scale to match the PERSIANN-CCS-CDR data in temporal resolution. This figure demonstrates the superior performance of PERSIANN-CCS-CDR in detecting the magnitude of precipitation at the 3-hourly temporal scale. For the period between 6:00 to 9:00 UTC, PERSIANN-CCS-CDR estimates the rain rates fairly well compared to Stage IV radar data; however, a southward shifting can be seen in PERSIANN-CCS-CDR's estimates. During 9:00 to 12:00 UTC, 12:00 to 15:00 and 15:00 to 18:00 UTC, PERSIANN-CCS-CDR successfully detects the amount of intense precipitation over the eastern regions of the watershed, yet it misses some parts of the rainfall that occurred over the central parts of the region. During 18:00 to 21:00 UTC, the PERSIANN-CCS-CDR detects most of the intense rainfall. A northward shift can be seen in PERSIANN-CCS-CDR's estimates for the period of 21:00 to 24:00 UTC. Table 5.1 summarizes PERSIANN-CCS-CDR performance in detecting (POD, FAR, CSI) and estimating (RMSE, MAE, Correlation) rainfall intensity at 3-hourly temporal and 0.04° × 0.04° spatial resolutions over the shown watershed on August 12, 2016.

Table 5.1 Summary of 3-hourly precipitation estimation performance of PERSIANN-CCS-CDR for the Louisiana flood of Aug. 12, 2016 at 0.04° × 0.04° spatial resolution.

Criteria	**PERSIANN-CCS-CDR**
POD	0.85
FAR	0.24
CSI	0.67
RMSE (mm/3hr)	13.6
MAE (mm/3hr)	6.12
CC	0.64

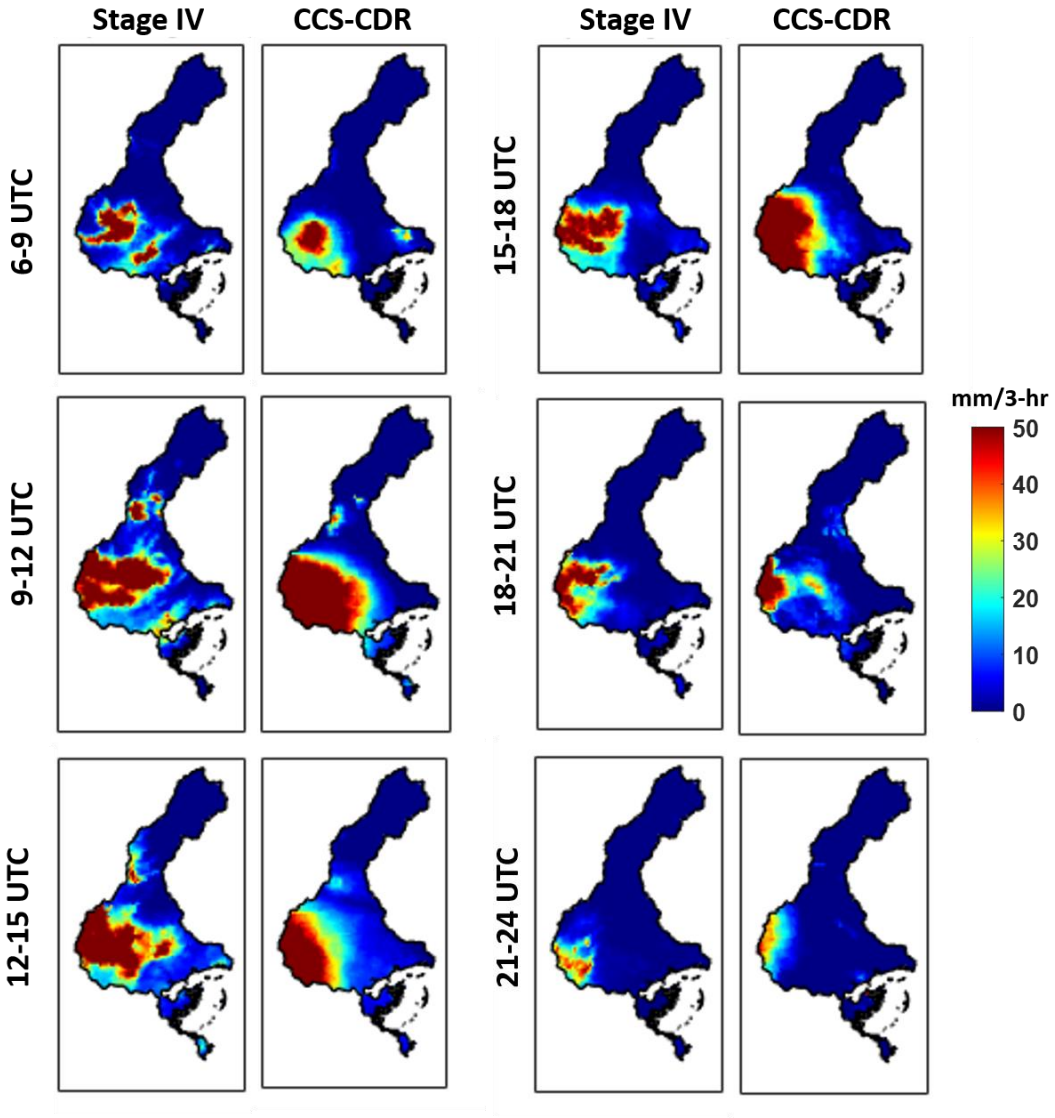

Figure 5.5 Evaluation of 3-hourly PERSIANN-CCS-CDR against Stage IV for the Louisiana flood of Aug. 12, 2016.

5.4.3. Missing Data

Figure 5.6 and Figure 5.7 show the temporal and spatial distributions of the 3-hourly missing data for the whole globe. Figure 5.7 shows the percentage of missing 3-hourly pixels in a month for the top zone (20°N to 60°N), middle zone (20°S to 20°N) and bottom zone (20°N to 60°N). According to Figure 5.6, most of the missing data is attributed to the GridSat-B1 dataset (1983-2000) and less missing is observed for CPC-4km (2000-2020). However, the number of missing pixels for GridSat-B1dataset declines from 1983 to 2000. Considering the

2000 to 2020 period, October 2005 has the largest number of missing pixel data, especially in the bottom zone. These missing pixels are due to problems with the aging Japanese satellite for that period. The number of missing data pixels for the rest of the period is close to zero. Among the three presented zones, the middle zone has the least number of missing data as can be observed in both Figure 5.6 and Figure 5.7. According to Figure 5.7, most of the missing pixels are between 60°E to 90°E and between the 45° to 60° S and N. These patterns are due to the missing information from the satellite image retrieval. Similar patterns with fewer missing data counts can be observed between 135°W to 165°W.

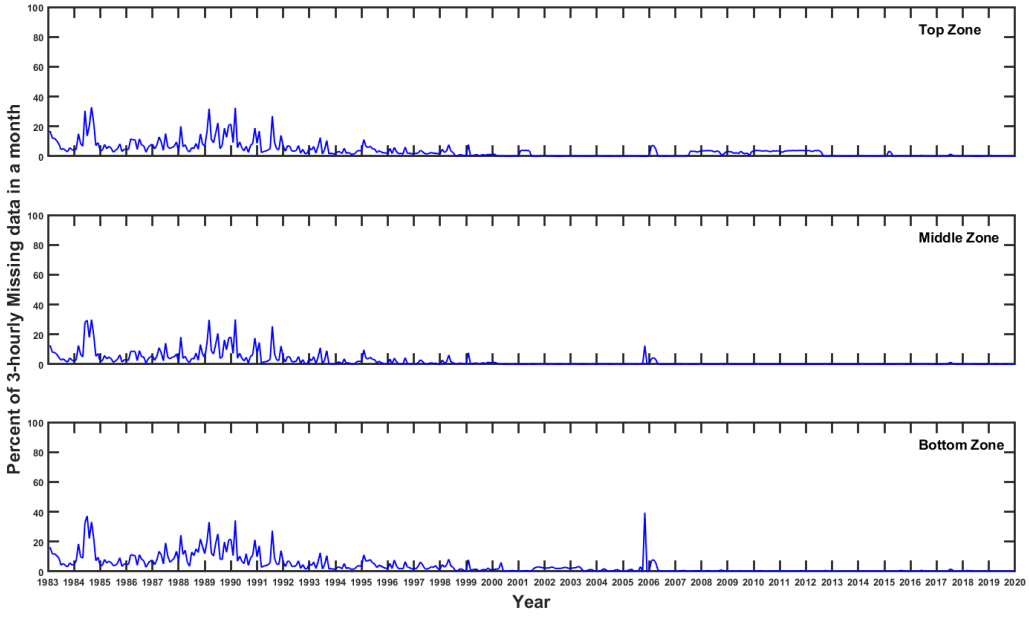

Figure 5.6 Percent of 3-hourly missing data in each month

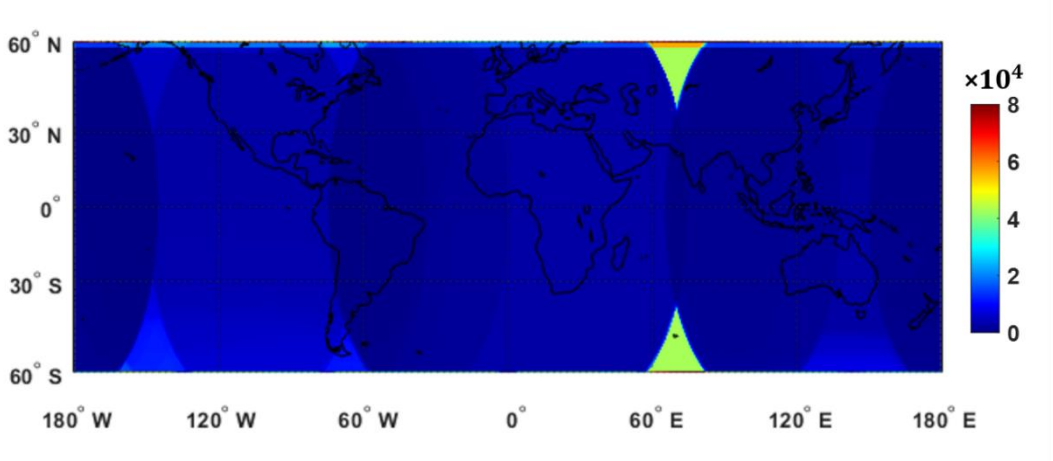

Figure 5.7 Spatial distribution of the 3-hourly missing pixels

5.5. Conclusions

Accurate long-term precipitation estimates with fine spatiotemporal resolution, especially accurate heavy precipitation rates, are crucial for a wide variety of applications, including rainfall frequency analysis, early warning system development, disaster management strategies, and water resource management. PERSIANN-CCS-CDR, which provides accurate estimation of extreme precipitation with fine spatiotemporal resolution (0.04° spatial and 3-hourly temporal resolution) from 1983 to present over the global domain of 60°S to 60°N, has been developed and is presented in this manuscript.

One of the most attractive features of PERSIANN-CCS-CDR is its improved performance for detecting heavy precipitation. While current operational satellite-based precipitation datasets provide significant opportunities for providing precipitation estimates at high spatiotemporal resolution over the globe, numerous studies have argued that they have a weakness in detecting heavy precipitation that occurs at high temporal resolution (sub-daily or 3-hourly) (Mehran and AghaKouchak 2014; AghaKouchak et al. 2011). The current limitations for accurate estimation of extreme precipitation hinder the use of satellite-based precipitation datasets for applications that are sensitive to heavy rain rates such as designing warning systems, integrating precipitation data into hydrological models, etc. The performance of PERSIANN-CCS-CDR for heavy precipitation detection suggests that this dataset is an attractive dataset for the mentioned hydrological applications.

Another important feature of the PERSIANN-CCS-CDR dataset is the combination of high spatial and temporal resolution with a long period of record. A reliable long-term precipitation record with fine spatiotemporal resolution is essential for many applications including hydrological modelling, rainfall frequency analysis, and development of depth duration curves. However, the majority of current operational datasets are either high resolution with short-duration estimates or lower resolution with long-term estimates (Kidd and Levizzani 2011). PERSIANN-CCS-CDR, which provides accurate estimations of extreme precipitation with fine spatiotemporal resolution (0.04° × 0.04° spatial and 3-hourly temporal resolution) from 1983 to present over the global domain of 60°S to 60°N, has been developed to address the lack of available datasets that meet both needs.

To develop the PERSIANN-CCS-CDR dataset, archives of the historical GridSat-B1 IR and CPC-4km IR datasets are used as input to the PERSIANN-CCS algorithm to produce historical precipitation estimates. PERSIANN-CCS-CDR then utilizes the resulting PERSIANN-CCS estimates as input. PERSIANN-CCS-CDR bias adjusts the PERSIANN-CCS estimates using monthly GPCP v2.3 at 2.5° spatial scale through probability density function (PDF) matching. The performance of both PERSIANN-CCS-CDR and PERSIANN-CDR for estimating extreme events was evaluated over the globe and the CONUS. The results highlight the superior performance of PERSIANN-CCS-CDR by 15% in correlation and 28% in RMSE compared to PERSIANN-CDR against the CPC rainfall dataset for extreme events over globe. The evaluation of extreme events over the CONUS revealed that PERSIANN-CCS-CDR compared to PERSIANN-CDR can estimate rain rates with a 25% higher correlation and a 31% lower RMSE. Further evaluation of PERSIANN-CCS-CDR performance was demonstrated using two case studies over the CONUS. The first case study for Hurricane Harvey, which occurred in 2017, shows the capability of the newly developed dataset for capturing heavy rain rates at a larger spatial scale. The results indicate that PERSIANN-CCS-CDR can detect precipitation with lower RMSE and higher CC versus to PERSIANN-CDR against Stage IV radar observations. Additionally, PERSIANN-CCS-CDR outperformed PERSIANN-CDR for estimating heavy rain rates. The second case study evaluated the performance of PERSIANN-CCS-CDR at a watershed scale for the flood event that occurred in Louisiana during August 2016. The results at daily scale revealed again the superior performance of PERSIANN-CCS-CDR compared to PERSIANN-CDR for detecting and estimating heavy rain rates.

Furthermore, PERSIANN-CCS-CDR provides precipitation at higher spatiotemporal resolutions (0.04° × 0.04° spatial and 3-hourly temporal) compared to PERSIANN-CDR (0.25° × 0.25° and daily) making this new dataset an attractive product for many hydrological applications.

One of the few potential shortcomings of the PERSIANN-CCS-CDR dataset is that the available time scale of GridSat-B1 is 3-hourly, rather than hourly, for the period before 2000. This limits the capability of the dataset to that coarser temporal resolution for the period from 1983 to 2000. Another limitation is the PERSIANN-CCS algorithm's capability to capture the spatial patterns of rainfall. PERSIANN-CCS extracts cloud information based on manually defined features including coldness, texture, and geometry, which can limit its ability to accurately estimate rainfall because manual feature extraction is always biased toward the most relevant and physically obvious features that have direct impacts on precipitation occurrence. Due to the complexity of the precipitation phenomena, there may be some other factors as yet hidden to CHRS researchers that play crucial roles in the accuracy of the model's simulations. CHRS researchers are currently working on the development of even more advanced satellite retrieval algorithms by applying new data-driven methodologies to automatically extract features from the input datasets. While more research needs to be done to verify the performance of the developed dataset, this paper presents promising validation results and demonstrates example applications for the PERSIANN-CCS-CDR dataset. This newly introduced dataset provides an opportunity for scientists and stakeholders to leverage the more accurate estimates of PERSIANN-CCS-CDR to improve disaster mitigation models and strategies.

CHAPTER SIX:

APPLICATION OF REMOTE SENSING PRECIPITATION DATA AND THE CONNECT ALGORITHM TO INVESTIGATE SPATIOTEMPORAL VARIATIONS OF HEAVY PRECIPITATION: CASE STUDY OF MAJOR FLOODS ACROSS IRAN (SPRING 2019)

The contents of Chapter 6 are published in the Journal of Hydrology

Citation: Sadeghi, M., Shearer, E. J., Mosaffa, H., Gorooh, V. A., Naeini, M. R., Hayatbini, N., ... & Sorooshian, S. (2021). Application of remote sensing precipitation data and the CONNECT algorithm to investigate spatiotemporal variations of heavy precipitation: Case study of major floods across Iran (Spring 2019). Journal of Hydrology, 600, 126569.

6.1. Abstract

In recent years, the number of floods following unprecedented rainfall events have increased in Iran during early spring (March 21st to April 20th, referred to in Iran as the month of "Farvadin"). While numerous studies have addressed changes in climate extremes and precipitation trends at different temporal scales from daily to annual across the country, analyses of short-duration and heavy precipitation, especially during recent years, are rarely considered. Furthermore, most studies investigate the variations in extremes and total precipitation using a limited number of synoptic weather stations across Iran. This study assesses the variations in heavy precipitation (precipitation with intensities greater than or equal to 3 mm/3 hours) at 0.04° spatial and 3-hourly temporal resolution during the month of Farvardin. In addition, the effect of atmospheric river conditions over Iran and their possible link to intensifying heavy precipitation is explored. For this purpose, the CONNected-objECT (CONNECT) algorithm is applied on a precipitation dataset, Precipitation Estimation from Remotely Sensed Information Using Artificial Neural Networks-Cloud Classification System (PERSIANN-CCS), and an Integrated Water Vapor Transport (IVT) dataset from the NASA Modern-Era Retrospective Analysis for Research and Applications Version-2 (MERRA-2). The results suggest that the increase in the number of floods in recent years is related to the increase in the intensity and volume of heavy precipitation events, although the frequency and duration of heavy precipitation events have not changed significantly. Furthermore, the results show that atmospheric river conditions over the country are present during the same window as each year's most extreme events. It is found that 8 out of 13 of the largest ARs over Iran come from moisture plumes with pathways over the African and Red Sea.

6.2. Study area & Data

6.2.1. Study area

Iran is in a semi-arid and arid subtropical region of southwest Asia at longitude 25–40°N and latitude 44–65°E. The country is bounded by the Caspian Sea on the north and the Persian Gulf and Gulf of Oman in the south (Figure 6.1). The study area covers the extent of Iran's borders, measuring at about 1.6 million km2. Iran is characterized by complex topography:

most of the central and southeastern parts of Iran are covered by barren/arid areas (Dashte-e Kavir and Dashte-e Lut) and western and northern regions are covered by Zagros and Alborz main mountain ranges. Iran is the scene of various meteorological and climatological mechanisms (mostly induced by the subtropical high-pressure regimes) resulting in uneven spatial and temporal distribution of precipitation across the country. The southern part of Iran is affected by the anticyclonic circulation over the Arabian Sea (Raziei et al. 2012), the El Niño-Southern Oscillation (ENSO) (Saghafian et al. 2017; Nazemosadat and Ghasemi 2004), and the Monsoon phenomenon(Zarrin et al. 2010; Yadav 2016) while mountainous regions in western Iran block moisture-loaded ARs from the tropical Atlantic Ocean and Europe driven by the Black Sea and Mediterranean cyclones(Azizi et al. 2013; Vaghefi et al. 2019).

In our study, to identify the spatial and temporal variations of heavy precipitation events during the month of Farvardin and examine the effect of ARs on these variations, we consider a large spatial domain from 10°W to 70°E and from 0° to 50°N, including some parts of North Atlantic Ocean, Europe, Middle East, and North Africa (Figure 6.1).

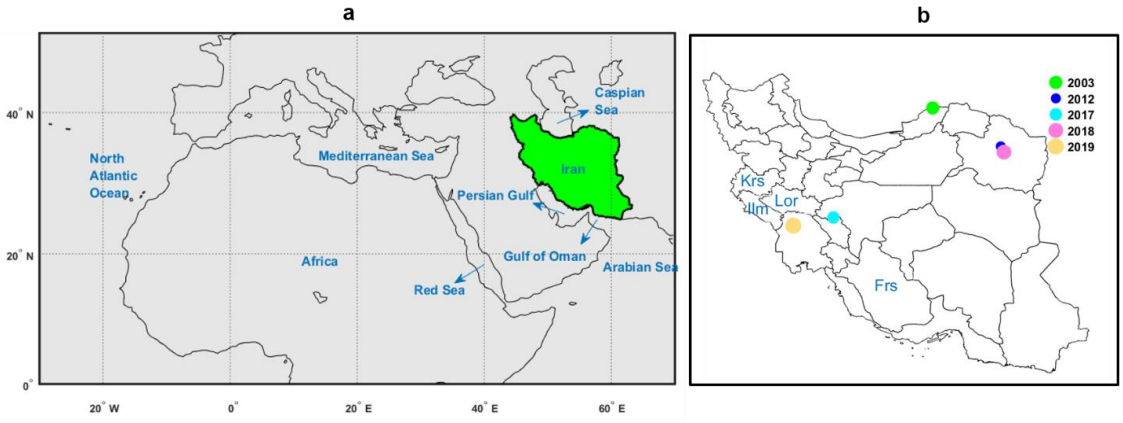

Figure 6.1 a) The study area (green) and surrounding regions b) Selected provinces including Ilam (Ilm), Fars (Frs), Kermanshah (Krs), and Lorestan (Lor) and location of the five heaviest events in Farvardin in terms of volume (2003, 2012, 2017, 2018, and 2019) tha

6.2.2. Data sets

PERSIANN-CCS

PERSIANN-CCS is a satellite-based operational product that consists of hourly rainfall estimates at 0.04°x0.04° (approximately 4 km) spatial resolution(Hong et al. 2007). It uses infrared (IR) imagery from geostationary satellites and extracts the cloud features such as temperature, geometry, and texture to estimate rainfall using a data-driven model. PERSIANN-CCS is a useful tool for monitoring and analyzing heavy precipitation events in near-real-time at a quasi-global scale (60°N to 60°S). This dataset is available as an operational climate data record via the CHRS Data Portal[1].

PERSIANN-CDR

PERSIANN-Climate Data Record (CDR), like PERSIANN-CCS, is a rainfall product that is a quasi-global and satellite-based. PERSIANN-CDR differs from PERSIANN-CCS by its intention: while PERSIANN-CCS is primarily for real-time measurements, PERSIANN-CDR's long duration (1983-present) makes it most useful for climate-scale studies (Ashouri et al. 2015). As accuracy is a primary motivation for the development of PERSIANN-CDR data, daily passive microwave data and monthly GPCP v2.3 rain gauge values are used for bias correction. PERSIANN-CDR's focus on accuracy means it's not available at scales as fine as PERSIANN-CCS—PERSIANN-CDR's spatiotemporal resolution is limited to daily and 0.25°x0.25° pixels. In this study, PERSIANN-CDR is used to investigate the climatology of AR-associated rainfall during Farvardin. Like PERSIANN-CCS, PERSIANN-CDR is available from the CHRS Data Portal (see above.)

Integrated Water Vapor Transport from MERRA-2

Integrated water Vapor Transport (IVT) is the amount of atmospheric moisture integrated across all levels of the atmosphere, calculated from the following formula:

$$\boldsymbol{IVT} = \frac{1}{g}\int_{P_{surf}}^{P_{200}} q\boldsymbol{V}\, dp$$

where p is pressure (hPa), p_200 is pressure at 200 hPa, assumed to be the top of the atmosphere, p_surf is the geopotential height at the Earth's surface (1000 hPa), q is specific

[1] http://chrsdata.eng.uci.edu/

humidity at pressure height p, V is the wind velocity (m/s) at p, and g is gravitational acceleration. IVT was calculated from the wind and pressure values retrieved from the National Aeronautical and Space Agency's (NASA) Modern-Era Retrospective Analysis for Research and Applications-version 2 (MERRA-2) data (Gelaro et al. 2017).

Gauge dataset

To evaluate PERSIANN-CCS's accuracy during Farvardin 2019, the PERSIANN-CCS estimates are compared with ground-based gauge observations from 70 synoptic meteorological stations from the Iran Meteorological Organization at the daily scale. These evaluations are performed over 4 provinces (Fars, Lorestan, Kermanshah, and Ilam) which were affected the most by the heavy precipitation events during Farvardin 2019. The comparison is conducted against PERSIANN-CCS pixels that contained at least one meteorological ground-based observation.

6.3. Methodology

6.3.1. CONNECT Algorithm

The CONNected-objECT (CONNECT) algorithm (Sellars et al., 2013; 2015; 2017) is a big data algorithm that uses connectivity (overlap) to segment, group, and track elevated or anomalous data signatures in large volumes of data. It was developed to study hydroclimate extremes, including, but not limited to, ARs (Shearer et al. 2020), tropical and extratropical cyclones, droughts, and more. The algorithm's architecture is designed with object-oriented analysis in mind, where "objects" are identified items, events, etc. that can be represented by attributes and statistics and object-oriented analysis is the study of populations of "objects" from their attributes and statistics (Figure 6.2). Object-oriented analysis has noteworthy benefits for hydroclimate studies: events are discretely counted and recorded, meaning they can be examined individually, or their population considered statistically, from techniques as simple as calculating averages and percentiles to distribution building and cluster analysis.

CONNECT uses three-dimensional (x,y-spatial and temporal) voxels of a target variable (e.g. rainfall) to construct objects where voxels with intensities above a user-defined threshold are contiguous over space and time, performed using a flood filling algorithm. As grouping

voxels across the time axis captures the evolution of an object from genesis to terminus, CONNECT performs well as a tracking algorithm, meaning objects segmented by CONNECT are the lifecycles of weather phenomena. CONNECT auto-calculates object characteristics, such as spatiotemporal properties like volume, speed, duration, etc. and outputs it into a table for statistical/object-oriented analysis.

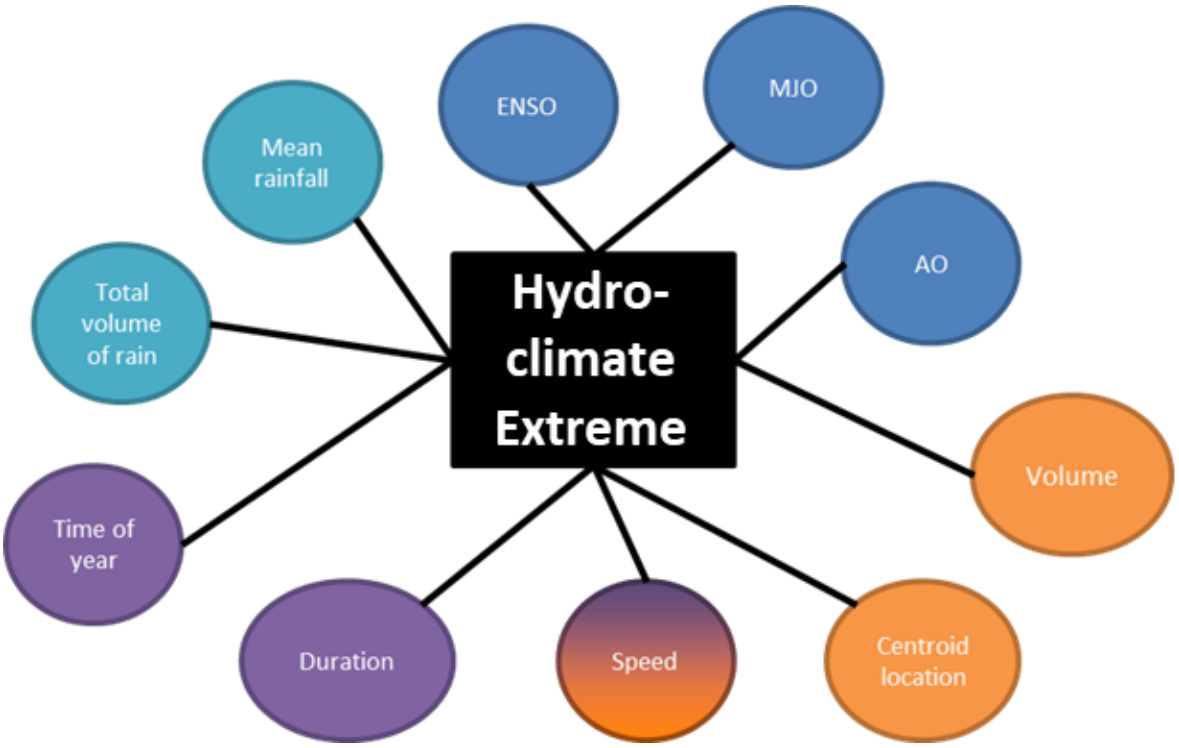

Figure 6.2 An object ("hydroclimate extreme") described by its characteristics ("total volume of rainfall", "duration", etc.)

For this study, 3-hourly precipitation data from PERSIANN-CCS during the month of Farvardin every year from 2003-2020 was used as input to CONNECT. As our interest for this study lies entirely within the boundaries of Iran, precipitation fields are clipped to the country's borders. To capture longer-duration heavy events over the region, CONNECT was set up to only consider rainfall totals equal to or greater than 3 mm/3 hours and to filter objects with durations shorter than twelve hours. Selecting the threshold parameter for CONNECT is largely based on balancing between over-segmenting and under-segmenting. Over-segmented rainfall disrupts the tracking functionality of CONNECT: smaller objects moving at faster speeds will not overlap during subsequent timesteps and will not be

considered as the same object. At the same time, under-segmented rainfall will track multiple events as a singular "conglomerate" event. As an example, consider rainfall systems in the intertropical convergence zone. At very low thresholds, CONNECT will not differentiate between the light rainfall that constantly occurs in the region and the periodic heavy rainfall from transient mesoscale convective systems that also frequently form and dissipate over the course of a day. If a researcher's goal is to study the lifecycles of the latter phenomena, a higher rainfall threshold rate is required for suitable results. We note similarities between the geography of Iran and California (further explained in the subsequent section) and therefore elect to use the 1 mm/hour (here, 3 mm/3-hour) threshold used in Sellars et al. (2013). At this value, rainfall is a less than half of the Glossary of Meteorology's definition of moderate rainfall (2.5 mm/hour), but well above the rainfall rates of a drizzle (0.3 mm/hour), meaning rainfall rates captured are impactful but not necessarily extreme. A higher threshold is undesirable as it omits important data and serves to underestimate storm total volume calculations.

6.3.2. Defining the thresholds for detecting AR over Iran.

An AR is a narrow, transient atmospheric pathway that transports a large amount of water vapor from distant water bodies. In dry countries like Iran, which is located in subtropical latitudes, ARs originating from water bodies located west of the country can be a significant source of precipitation. Furthermore, Guan and Waliser (2015) showed that ARs are contribute to orographic rainfall occurrences and can cause extreme precipitation events and flooding in Iran. Therefore, for hydrological purposes it would be useful to study extreme precipitation events

and ARs particularly in mountainous region of Iran (e.g, Zagros Range). To investigate whether the most extreme CCS-CONNECT objects over Iran were related to AR activity, we utilized the methodology from Rutz et al. (2014, hereby referred to as "Rutz"). Rutz defines an AR as a region of IVT greater than 250 kgm^(-1) s^(-1) that extends to a length greater than or equal to 2,000 km. The Rutz methodology is referred to as a "permissive" methodology (as opposed to a "restrictive" method), which means its requirements are laxer and generally tend to classify anomalous IVT regions as ARs more often than other methodologies. This methodology was selected because Iran has notable analogs to

California, where the methodology was developed, including its northwest-southeast trending Zagros Mountain range with peaks up to 4,400 meters, which has the same orientation and prominence as the Sierra Nevada Range, along with its location in the lower mid-latitudes. However, we acknowledge that Iran's position east of the dry Saharan Desert is in stark contrast to California's proximity west of the Pacific Ocean, a water body source which feeds Pacific ARs with their moisture, though a notable analog exists in the Red and Mediterranean Seas, along with the Persian Gulf (Dezfuli 2019). Furthermore, ARs over Iran have yet to be analyzed using an precipitation-linked IVT threshold which can be utilized in global studies, like that used in Rutz et al., (2014); the 85th percentile of IVT over Iran and the surrounding region was used as a threshold in Dezfuli (2019) and Esfandiari and Lashkari (2020) the values of which would be far too low of a threshold to be useful over North America, Europe, etc. It is important to note that we do not argue that using a regionally derived IVT threshold makes the ARs in these studies less deserving of the AR label. However, by proving that ARs exist at IVT levels that can be utilized globally and is tied to precipitation, we prove that Iran is a region where ARs of noteworthy strength frequently occur, at least in the month of Farvardin, making it comparable to the North American west coast, Europe, Chile, and other regions of the world.

To robustly investigate the influence ARs have in the region during Farvardin, the climatology of ARs and AR precipitation over Iran during the month of Farvardin is investigated using the Rutz methodology and the multi-decade PERSIANN-CDR precipitation dataset over 1990-2019. The 30-year duration was chosen in compliance with the standards of the World Meteorological Organization (WMO). Figure 6.3 explores three metrics that seek to investigate how ARs impact Iran during Farvardin, specifically regarding frequency and its link to precipitation. In the Zagros mountains, precipitation and IVT are correlated to values as high as 55%, including the greater Tehran metropolis. Moreover, moderate correlations of 35%-45% exist across the entirely of north and central Iran. AR frequencies are greatest along the coast of the Persian Gulf and the Gulf of Oman up to the foot of the Zagros Mountains, where they occur on average 7-10% of the month, or up to 3 days a month. Thus, two similarities between the climatology of Iran and California are observed: the high correlation between IVT and rainfall, especially in topographically complex regions (Rutz et al., 2014) and the high frequency of elevated IVT fluxes that perpendicularly strike a

prominent mountain range. In addition, the fraction of AR rainfall is over 50% in the southern part of the country. Owing to these similarities, it can established that 1) atmospheric rivers at IVT fluxes required by the Rutz methodology (impact-linked) are non-insignificant players in Iran's Farvardin hydroclimate, meaning 2) The Rutz methodology and others that aren't linked to climatological averages, like what is done in Defuzli (2019), are appropriate to use in the region for AR-related studies. In this study, we investigate the contribution of ARs on heavy precipitation using IVT and gauge information.

Despite the breadth of analysis done in this study regarding ARs over Iran and their perceived link to heavy precipitation events, it is vital to note that establishing a concrete link between ARs and heavy precipitation requires numerical modeling simulation as described by Davolio et al. (2020) and such research should be conducted before solid conclusions can be made. Such numerical simulations are outside the scope of this study.

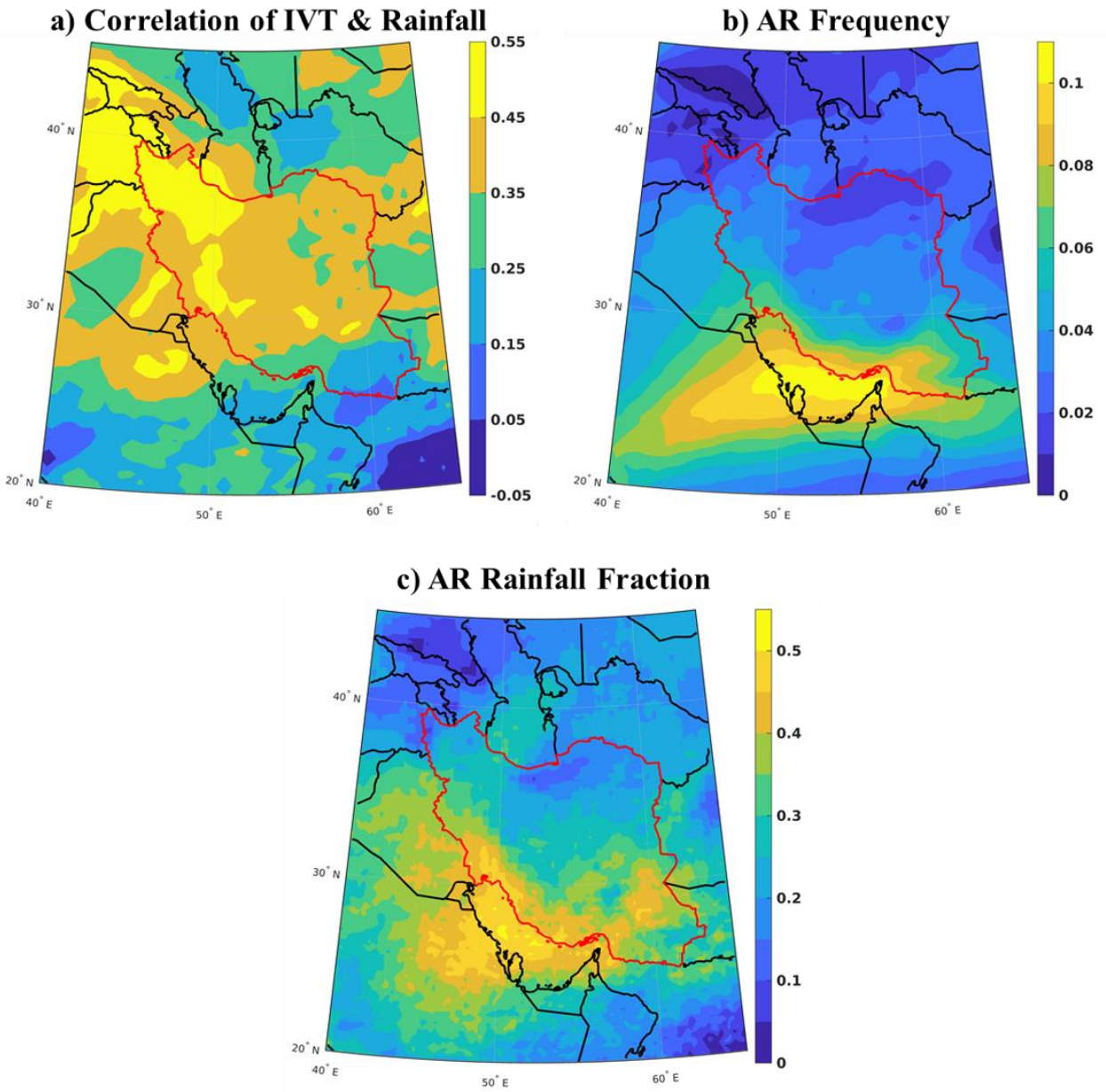

Figure 6.3 Climatology of ARs over Iran during Farvardin, using 1990-2019 baseline period. a) The correlation of 24-hr (00z-00z) IVT averages to 24-hr precipitation accumulations from PERSIANN-CDR. b) Frequency of AR conditions. c) Fraction of precipitation.

6.3.3. Performance measurements

Categorical evaluation statistics including Probability of Detection (POD), False Alarm Ratio (FAR), Critical Success Index (CSI) are utilized to evaluate the performance of the PERSIANN-CCS dataset for detecting rain/no rain pixels. Continuous indices including Pearson's correlation coefficient (CC), Root Mean Square Error (RMSE) and Bias (BIAS; BIAS=estimation-observation) are used to assess the accuracy performance of PERSIANN-

CCS in estimating the rainfall intensity (Wilks, 2011). A value of 1 mm/day is utilized as a rain/no rain threshold in both PERSIANN-CCS estimates and ground-based gauge observations.

6.4. Results and Discussion

Figure 6.4 displays the spatial map of the accumulated precipitation for the month of Farvardin during the period from 2003 to 2020 using PERSIANN-CCS data. The mean monthly precipitation during Farvardin for this period was 86 mm. For the most recent years, the average precipitation was 107 mm (in 2018), 178 mm (in 2019), and 100 mm (in 2020), all of which were higher than the baseline mean precipitation from 2003 to 2020. Furthermore, the year 2019, when Iran experienced many floods, was the wettest year in the last two decades. In addition, Figure 6.4 reveals that the spatial pattern of accumulated precipitation varies among different years. The greatest concentration of rainfall occurred over northeastern Iran in 2003 while southwestern Iran experienced the bulk of precipitation in 2019.

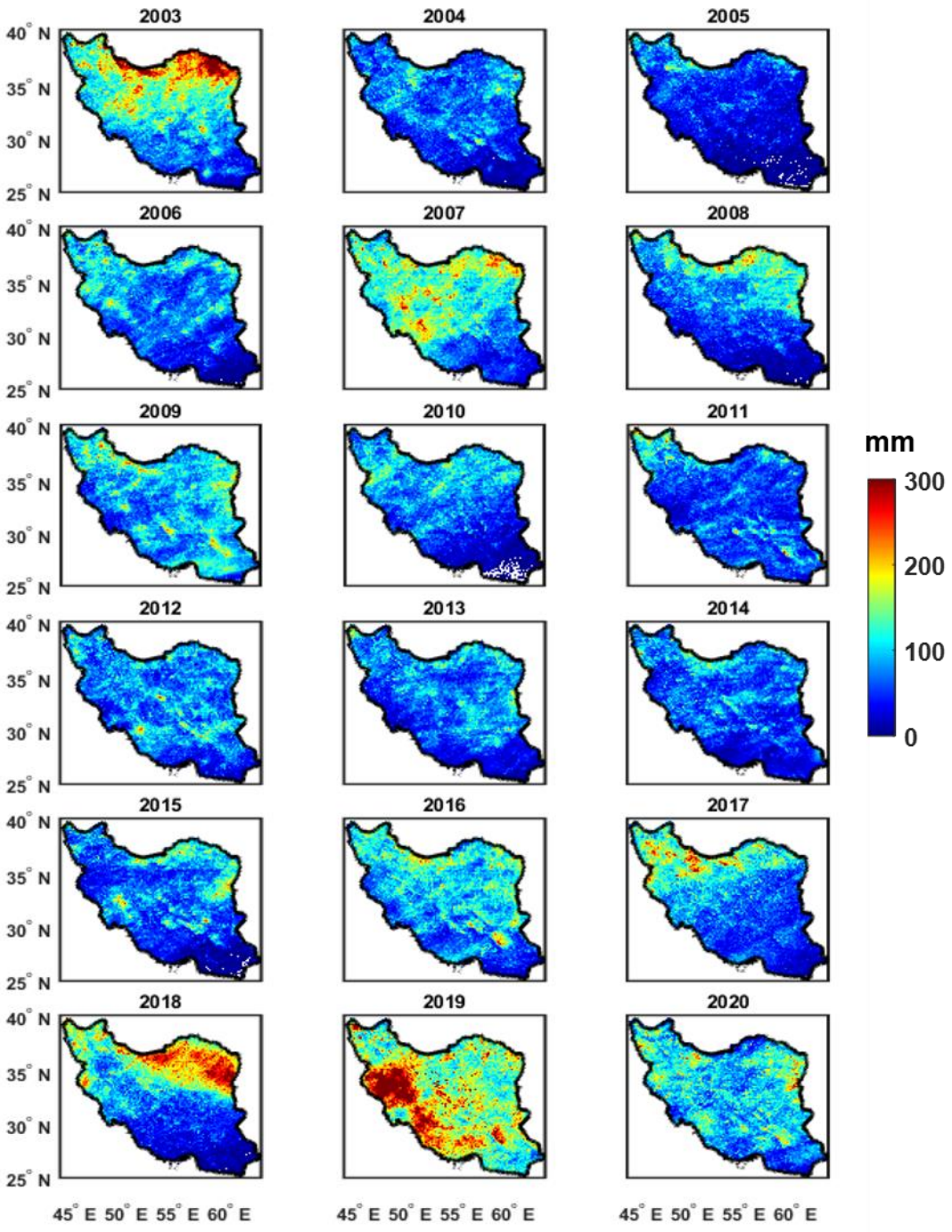

Figure 6.4 Accumulated precipitation estimates for the month of Farvardin over Iran from 2003 to 2020 using PERSIANN-CCS estimates.

6.4.1. Evaluation of PERSIANN-CCS for 2019

As discussed in the introduction, Katiraie-Boroujerdy et al. (2020)and Mosaffa et al. (2020) evaluated the performance of the daily PERSIANN-CCS estimates over Iran for the period

prior to 2018. The intention of this study is not to evaluate the capability of PERSIANN-CCS for precipitation estimation, but rather evaluate rainfall totals during Farvardin 2019 against ground-based observations for the provinces that experienced floods. Table 6.1 presents spatial averages of categorical and continuous evaluation metrics over four selected provinces: Fars, Ilam, Kermanshah, and Lorestan. These are among the provinces that reported the greatest flooding damages during the Farvardin 2019 floods. In terms of categorical statistics, POD and FAR values are 0.78 and 0.28 over these provinces, respectively. PERSIANN-CCS with 0.65 (0.53) has the best (worst) performance in terms of CSI over Kermanshah (Ilam) province. According to continuous statistical metrics, the correction coefficient (CC) is approximately 0.55 in the selected provinces and the highest CC values appear over the Ilam province with the value of 0.75. Also, RMSE ranges from 16.55 to 23.14 mm/day. In terms of bias, PERSIANN-CCS mainly overestimates (BIAS>0) precipitation intensity. When comparing our results to those of previous studies which evaluated different satellite precipitation products over Iran (Alijanian et al. 2017; Mahbod et al. 2019; Moazami et al. 2013; Mosaffa et al. 2020), it must be pointed out that PERSIANN-CCS performs better than other near-real time products during Farvardin 2019.

Table 6.1 Statistical evaluation of daily PERSIANN-CCS over selected provinces.

	Average on selected Province	**Fars Province**	**Ilam Province**	**Kermanshah Province**	**Lorestan Province**
POD	0.78	0.83	0.71	0.76	0.79
FAR	0.28	0.37	0.32	0.18	0.21
CSI	0.60	0.55	0.53	0.65	0.64
CC	0.62	0.48	0.75	0.47	0.69
RMSE (mm/day)	19.97	20.10	21.95	16.55	23.14
BIAS (mm/day)	3.44	6.38	6.31	0.96	1.37

Figure 6.5 presents the spatial distribution of POD, FAR, CSI, CC, RMSE, and BIAS over the four selected provinces. This figure shows that POD values in all stations is above 0.75 except a station in the north of Fars province and a couple of stations in the middle of western provinces which have POD about 0.6. Western provinces including Kermanshah, Ilam, and Lorestan have lower FAR than the Fars province in the south of Iran. Except for a few stations with CSI below 0.5, mostly found in the Fars province, other stations have CSI greater than 0.5. The spatial distribution of CC indicates that the PERSIANN-CCS algorithm has better performance over the western provinces than over Fars. According to Figure 6.5, CC in regions that experienced heavier precipitation is higher than in the other regions. Stations in the Lorestan province have the highest RMSE compared with other stations. On the contrary, stations in the south of Fars and Kermanshah provinces have the lowest RMSE. Although precipitation is overestimated (BIAS>0) in most of the stations, results of BIAS in the north of the Kermanshah province and a couple of stations in the east of the Lorestan province shows an underestimation of precipitation. Comparing with the conducted evaluation studies for near-real time precipitation over Iran, PERSIANN-CCS has the potential to be used as a candidate for short-term duration precipitation studies.

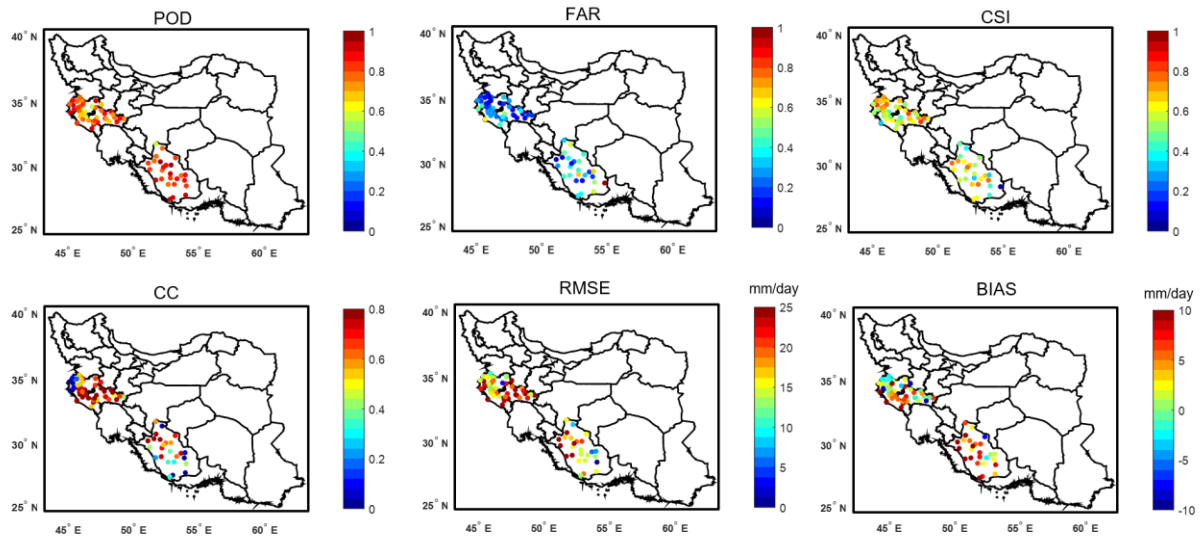

Figure 6.5 Spatial distribution of different statistical evaluation metric over the four selected provinces.

6.4.2. Temporal variations of heavy precipitation events during the period 2003 to 2020 using PERSIANN-CCS estimates

To quantify how the number of floods has been increasing during the last three years, we plot the frequency, intensity, duration, and volume of precipitation for the period 2003 to 2020 over the study area (Figure 6.6). For this purpose, we apply the CONNECT algorithm with a 3mm/3-hour threshold on the PERSIANN-CCS estimates for the period 2003 to 2020 for the month of Farvardin across Iran. The frequency (Figure 6.6a) of heavy precipitation events—events with more than 3mm/3-hour rainfall—does not show a significant change across the country during the month of Farvardin. The average number of intense events is 97; however, the highest number is 151 events occurring in 2019. The variations in intensity of heavy precipitation events (Figure 6.6b) demonstrate that the average magnitude of heavy rainfall has increased during the last three years. The average intensity of heavy precipitation events is 15.7 mm/3-hour for the whole period compared with 55.3 mm/3-hour in 2018, 79.0 mm/3-hour in 2019, and 30.1 mm/3-hour in 2020. These results are consistent with the increase in the number of floods reported across Iran during the last three years. The average duration of heavy precipitation (Figure 6.6c) was 14.2 hours during the last two decades, while peaking to 23.8 hours in 2019. The average volume of heavy precipitation (Figure 6.6d) during the month of Farvardin for the whole study period is 0.7 km3/event, while an average of 0.97 km3/event was recorded over the last three years of the study. The total volume of heavy precipitation per year (Figure 6.6e) was 77 km3 on average, compared with an average of 132 km3 of precipitation occurring during the last three years. Most notably, the total precipitation volume was 191 km3 in 2019. Overall, we can conclude that the increase in intensity, average volume per event, and total volume of heavy precipitation are the main reasons for the increases in the number of floods during the last three years over Iran.

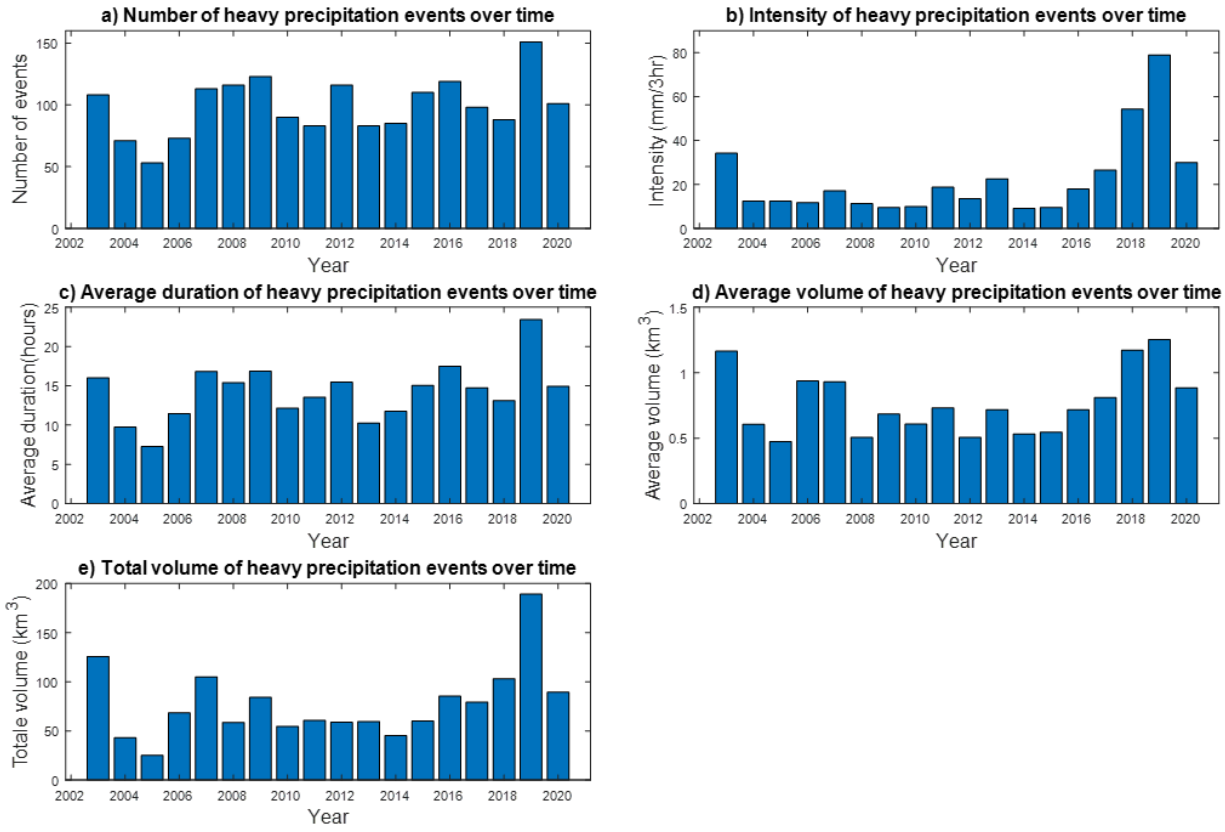

Figure 6.6 Temporal variations of heavy precipitation events during the period 2003 to 2020 using PERSIANN-CCS estimates.

6.4.3. Investigating atmospheric river presence during heavy precipitation events from 2003 to 2020

The Rutz et al. (2014) methodology was used to determine whether there was AR activity during the most extreme Farvardin rainfall events every year during 2003-2020, including extra significant events in 2019 and 2020. As Rutz is considered a permissive methodology, which implies an enhanced possibility of non-AR IVT features being classified as ARs, we further checked to see if AR activities existed over any area in Iran for at least 24 hours, thereby ensuring that an event satisfies the requirements of an "AR-1", the weakest category for an AR from the scale introduced by Ralph et al. (2019).

Over the study period, it was observed that AR conditions existed during every year's most extreme events, along with the two extra extreme events in 2019 and 2020. Among them, only three years (2010, 2011, and 2013) had AR conditions for less than 24 hours, with the

shortest (2011) that lasted for 9 hours. Furthermore, some events, such as the extreme rainfall event of 2004, could be traced back to multiple AR events affecting different regions of Iran.

Dezfuli (2019) observed that the sources of moisture for ARs that impact Iran come from the surrounding bodies of water, including the Mediterranean Sea, the Caspian Sea, the Persian Gulf, the Red Sea, and the Atlantic Ocean. From our analysis, we identify that the sources of moisture for ARs in the region are from the Atlantic Ocean via a northern Africa pathway and from the Red Sea via the Red Sea Strait (Bab-el-Mandeb). These pathways are also recognized in Esfandiari and Lashkari (2020). In Figure 6.7, we showcase the three most observed AR lifecycles in the region: 1) those that propagate from the Atlantic Ocean over northern Africa without significant influence from the Red Sea (Figure 6.7c, Figure 6.7d) driven by the Saharan anticyclone (Shay-El et al. 1999), 2) those with moisture chiefly coming from the Red Sea (Figure 6.7b) via the Red Sea Strait driven by a moisture transport at the 850 hPa level following a favorable position of the Arabian cyclone and mid-tropospheric troughs (Raziei et al. 2012) and 3) those which are created by merging bodies of moisture from both the Red Sea and the Atlantic Ocean (Figure 6.7a, Figure 6.7e), though the timing between ARs can vary between being simultaneous (Red Sea and African moisture at the same time; 2003 and 2019) and being subsequent (one source of moisture followed by other). Of these two different timings, it is the former that produces the events of greater volume, with the precipitation events of 2003 and 2019 being 4th and 1st heaviest by rainfall volume.

Table 6.2 showcases each AR with its pathway, determined by examining IVT objects at the 200 and 250 kg m-1 s-1 levels. Of the AR examined, three were found to come from moisture via the African pathway, seven from the Red Sea Strait, ten from both sources, and two from other sources (Gulf of Aden and Arabian Sea). This means that out of the 22 observed ARs, 17 were reliant on moisture fluxes from the Gulf of Aden while 13 could be linked to moisture transport over the African continent. Furthermore, each AR was ranked by the amount of precipitation it produced over Iran as calculated by CONNECT. The three highest ranking ARs all come from the three different AR classes, each occurring within the 2018-2019 period. Afterwards, ARs with moisture from both sources make up 7 out of 10 of the ARs

ranked 4th to 13th, yet only 3 out of 9 of the ARs ranked 14th onwards are from both sources. In summary, ARs with moisture from both the African and Red Sea sources are the most frequently observed ARs that coincide with heavy precipitation over Iran.

Table 6.2 The heaviest precipitation events during 2003 to 2020 and the presence of ARs bringing moisture over north Africa ("Af") or the Red Sea ("RS") during the event period.

Date	AR ?	>24 Hours	Pathway	Rainfall Volume (km3)	Rank
22 March - 26 March, 2003	Yes	Yes	Af & RS	34.22	4
April 1 - April 6, 2004	Yes	Yes	Af & RS	12.49	13
April 13 - April 19, 2005	Yes	Yes	RS	12.33	14
27 March - 31 March, 2006	Yes	Yes	RS	11.71	15
24 March - 27 March, 2007	Yes	Yes	Af & RS	17.09	10
April 6 - April 10, 2008	Yes	Yes	Af & RS	11.25	16
29 March - 2 April, 2009	Yes	Yes	Gulf of Aden	9.48	20
26 March - 29 March, 2010	Yes	No	RS	9.87	17
3 April - 8 April, 2011	Yes	No	Af & RS	18.71	8
26 March - 31 March, 2012	Yes	Yes	RS	13.48	11
4 April - 8 April, 2013	Yes	No	Arabian Sea	22.53	7
1 April - 4 April, 2014	Yes	Yes	Af & RS	9.07	21
28 March - 1 April, 2015	Yes	Yes	Af & RS	9.51	19
11 April - 15 April, 2016	Yes	Yes	Af & RS	12.91	12
23 March - 28 March, 2016	Yes	Yes	Af & RS	17.94	9

12 April - 16 April, 2017	Yes	Yes	Af	26.57	6
21 March - 26 March, 2018	Yes	Yes	Af	54.29	2
22 March - 27 March, 2019	Yes	Yes	Af & RS	78.99	1
31 March - 6 April, 2019	Yes	Yes	RS	44.94	3
20 March - 25 March, 2020	Yes	Yes	Af	8.17	22
27 March - 1 April, 2020	Yes	Yes	RS	9.84	18
11 April - 18 April, 2020	Yes	Yes	RS	29.92	5

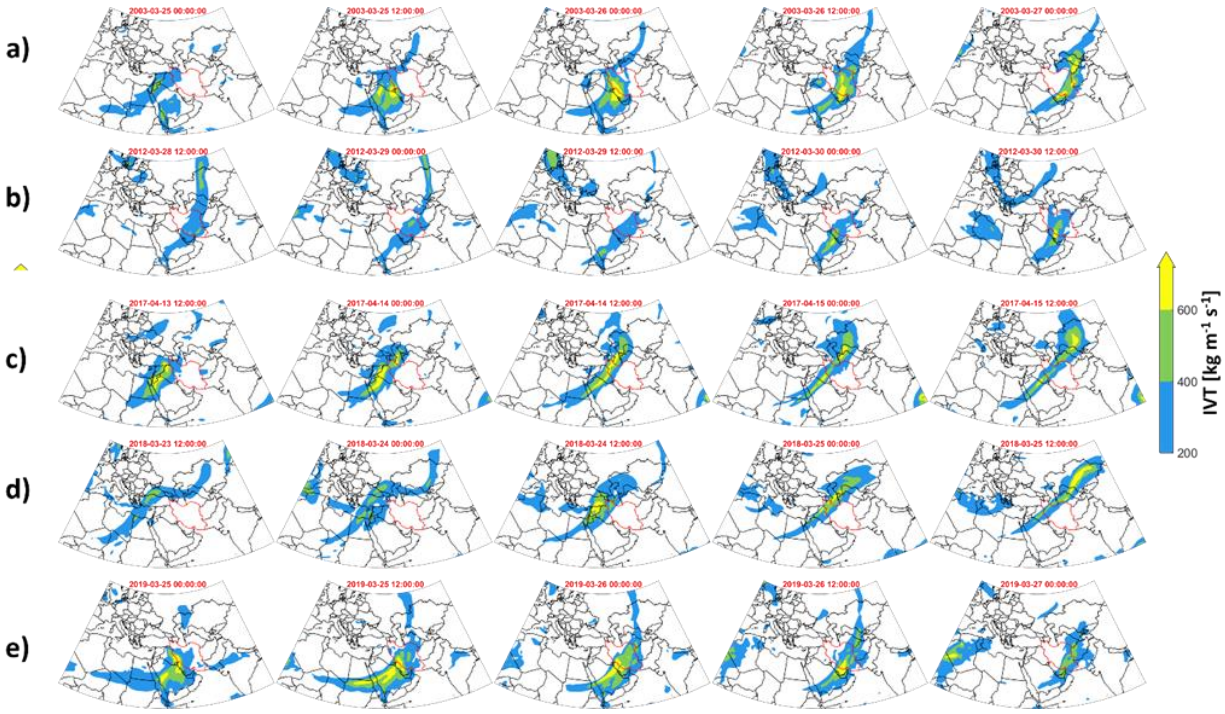

Figure 6.7 AR presence during the most severe heavy precipitation events during 2003 to 2020: a) 2003 b) 2012 c) 2017 d) 2018 e) 2019.

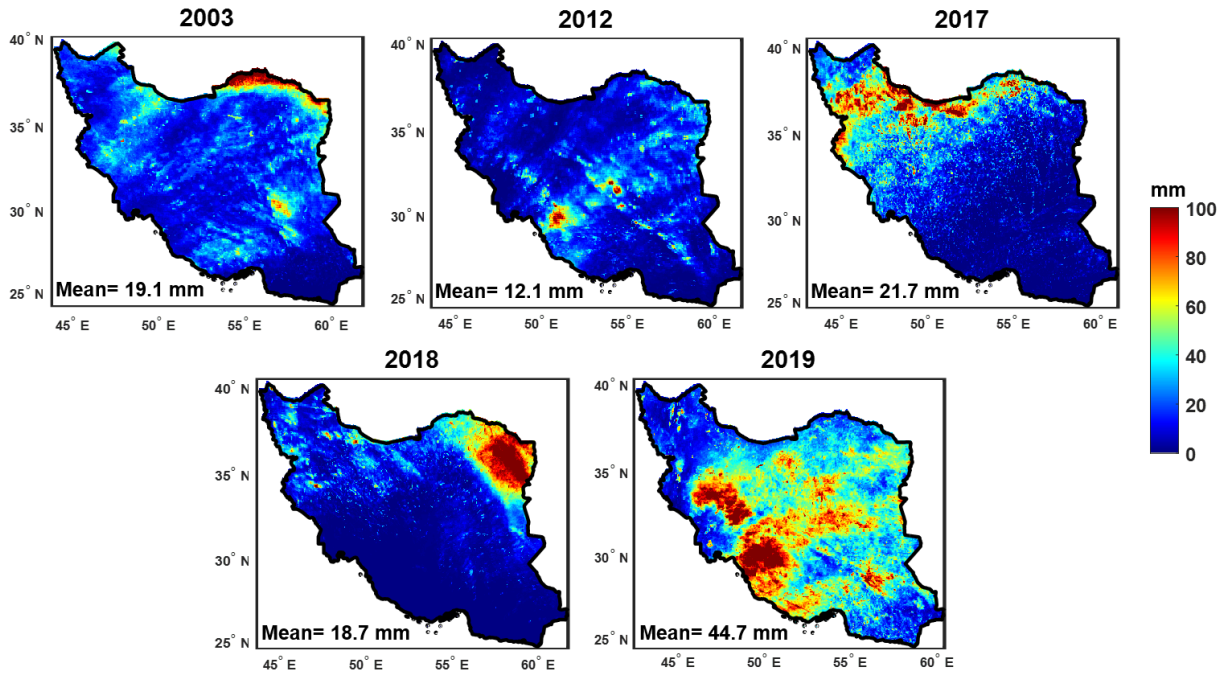

Figure 6.8 PERSIANN-CCS estimates correspond to the heavy precipitation events shown in Figure 7.

Figure 6.8 shows the accumulated amount of precipitation occurring during the events shown in Figure 6.7. The most extreme event that occurred in Farvardin 2003, which was ranked the 4th greatest event by volume and propagated from the Red Sea and the Atlantic Ocean, mainly occurred in northeastern Iran. On the other hand, the heavy precipitation that occurred in Farvardin 2019 that involved the most extreme events in terms of volume during the last two decades and had similar pathway to that from 2003 mainly occurred over Southwestern Iran. This figure shows precipitation from the most extreme events in 2003, 2012, 2017, 2018, and 2019 and highlights that extreme events in recent Farvardins (2018 and 2019) are heavier than those of the past.

6.5. Conclusion

Spring precipitation, especially during the month of Farvardin, is important for Iranian agriculture. Over the past few years, an increase in the number of floods occurring after unprecedented rainfall events during the month of Farvardin have affected millions of people across Iran, caused the loss of life, damaged infrastructure, and engendered

substantial economic losses in Iran's agriculture sector. The apparent increase in the number of floods during the last three years (2018 to 2020) led us to investigate the variations in different aspects of heavy precipitation events like intensity and frequency, as well as their associated mechanisms during the month of Farvardin. To our knowledge, there is no study which explores the precipitation variations and mechanisms during this month.

The previous studies over Iran mainly focused on analyzing heavy precipitation at daily scales over the whole year. However, there is a need to assess the flood-causing short-duration heavy precipitation that occurs in early spring. In addition, using a limited number of synoptic gauge observations has hindered the ability to explore the variations in precipitation at a high spatial resolution. In this study, we applied the CONNECT algorithm with a 3mm/3-hour threshold on the PERSIANN-CCS estimates at 0.04° spatial resolution to explore the variations in frequency, intensity, duration, and volume of heavy precipitation during Farvardin for the period from 2003 to 2020. The results indicated that increases in intensity and volume of heavy precipitation are the main reasons for the rising number of floods during Farvardin over the years 2018-2020. However, a significant increase in frequency and duration of heavy precipitation are not observed. The results also show that the frequency, intensity, duration, and volume of heavy precipitation was the highest in 2019 during the last two decades based on the PERSIANN-CCS estimates. This is also supported by the International Emergency Events database[1] which ranked the floods in Farvardin 2019 as the costliest economic loss in Iranian history during the last two decades. Spatial analyses revealed that heavy precipitation events occurred over almost the entire country in Farvardin during the period 2003 to 2020 with the heaviest volume of rainfall hitting southwestern Iran in 2019 and the second highest volume in northeastern Iran in 2018. In addition, we observe that the spatiotemporal distribution of heavy precipitation events extracted by the CONNECT algorithm are consistent with extreme events occurred over Iran.

Investigating the presence of AR conditions on heavy precipitation events that occurred during the month of Farvardin revealed that ARs exist during every year's most extreme events. In addition, we classify the AR pathways that occurred in the country during

[1] https://www.emdat.be/

Farvardin into three main categories. 1) ARs that propagated from the Atlantic Ocean via North Africa driven by the Saharan anticyclone, 2) ARs that propagated from the Red Sea via the Red Sea Strait and are influenced by the Arabian cyclone and mid-tropospheric troughs, 3) ARs created by merging bodies of moisture from both the Atlantic Ocean and the Red Sea. Our further investigations revealed that 8 out of 13 of the largest ARs over Iran come from moisture plumes with pathways over the African continent and the Red Sea.

Although this study mainly explored the variations of short-term precipitation over Iran for a specific month, the same procedure can be followed for other regions. This study highlighted that the high spatial (0.04°) and temporal (3-hourly) resolution of PERSIANN-CCS at a global scale is an attractive feature for analyzing precipitation variations, especially over the countries with limited rain gauge observations. In addition, the CONNECT algorithm, which is an object-oriented tracking algorithm, can be used for the investigation of natural hazards associated with AR events such as floods and mudslides over different regions.

REFERENCES

Adler, R. F., and A. J. Negri, 1988: A satellite infrared technique to estimate tropical convective and stratiform rainfall. *Journal of Applied Meteorology*, **27**, 30–51.

——, and Coauthors, 2018: The Global Precipitation Climatology Project (GPCP) monthly analysis (new version 2.3) and a review of 2017 global precipitation. *Atmosphere*, **9**, 138.

AghaKouchak, A., A. Behrangi, S. Sorooshian, K. Hsu, and E. Amitai, 2011: Evaluation of satellite-retrieved extreme precipitation rates across the central United States. *Journal of Geophysical Research: Atmospheres*, **116**.

Alijanian, M., G. R. Rakhshandehroo, A. K. Mishra, and M. Dehghani, 2017: Evaluation of satellite rainfall climatology using CMORPH, PERSIANN-CDR, PERSIANN, TRMM, MSWEP over Iran. *International Journal of Climatology*, **37**, 4896–4914.

Anagnostou, E. N., V. Maggioni, E. I. Nikolopoulos, T. Meskele, F. Hossain, and A. Papadopoulos, 2009: Benchmarking high-resolution global satellite rainfall products to radar and rain-gauge rainfall estimates. *IEEE Transactions on Geoscience and Remote Sensing*, **48**, 1667–1683.

Arkin, P. A., and B. N. Meisner, 1987: The relationship between large-scale convective rainfall and cold cloud over the western hemisphere during 1982-84. *Monthly Weather Review*, **115**, 51–74.

Ashouri, H., K.-L. Hsu, S. Sorooshian, D. K. Braithwaite, K. R. Knapp, L. D. Cecil, B. R. Nelson, and O. P. Prat, 2015: PERSIANN-CDR: Daily precipitation climate data record from multisatellite observations for hydrological and climate studies. *Bulletin of the American Meteorological Society*, **96**, 69–83.

Azizi, G., M. Arsalani, A. Bräuning, and E. Moghimi, 2013: Precipitation variations in the central Zagros Mountains (Iran) since AD 1840 based on oak tree rings. *Palaeogeography, Palaeoclimatology, Palaeoecology*, **386**, 96–103.

Beck, H. E., E. F. Wood, M. Pan, C. K. Fisher, D. G. Miralles, A. I. J. M. Van Dijk, T. R. McVicar, and R. F. Adler, 2019: MSWEP V2 global 3-hourly 0.1 precipitation: methodology and quantitative assessment. *Bulletin of the American Meteorological Society*, **100**, 473–500.

Behrangi, A., K. Hsu, B. Imam, S. Sorooshian, G. J. Huffman, and R. J. Kuligowski, 2009: PERSIANN-MSA: A precipitation estimation method from satellite-based multispectral analysis. *Journal of hydrometeorology*, **10**, 1414–1429.

Bessho, K., and Coauthors, 2016: An introduction to Himawari-8/9—Japan's new-generation geostationary meteorological satellites. *Journal of the Meteorological Society of Japan. Ser. II*, **94**, 151–183.

Chen, M., W. Shi, P. Xie, V. B. S. Silva, V. E. Kousky, R. Wayne Higgins, and J. E. Janowiak, 2008: Assessing objective techniques for gauge-based analyses of global daily precipitation. *Journal of Geophysical Research: Atmospheres*, **113**.

Chen, S., and Coauthors, 2013: Evaluation of the successive V6 and V7 TRMM multisatellite precipitation analysis over the Continental United States. *Water Resources Research*, **49**, 8174–8186.

Chen, Y., H. Jiang, C. Li, X. Jia, and P. Ghamisi, 2016: Deep feature extraction and classification of hyperspectral images based on convolutional neural networks. *IEEE Transactions on Geoscience and Remote Sensing*, **54**, 6232–6251.

Cristiano, E., M. ten Veldhuis, and N. van de Giesen, 2017: Spatial and temporal variability of rainfall and their effects on hydrological response in urban areas-a review. *Hydrology & Earth System Sciences*, **21**.

Das, T., A. Bárdossy, E. Zehe, and Y. He, 2008: Comparison of conceptual model performance using different representations of spatial variability. *Journal of Hydrology*, **356**, 106–118.

Davolio, S., S. Della Fera, S. Laviola, M. M. Miglietta, and V. Levizzani, 2020: Heavy precipitation over Italy from the Mediterranean storm "Vaia" in October 2018: Assessing the role of an atmospheric river. *Monthly Weather Review*, **148**, 3571–3588.

Dezfuli, A., 2019: Rare atmospheric river caused record floods across the Middle East. *Bulletin of the American Meteorological Society*,.

Erhan, D., Y. Bengio, A. Courville, P.-A. Manzagol, P. Vincent, and S. Bengio, 2010: Why does unsupervised pre-training help deep learning? *Journal of Machine Learning Research*, **11**, 625–660.

Esfandiari, N., and H. Lashkari, 2020: Identifying atmospheric river events and their paths into Iran. *Theoretical and Applied Climatology*, 1–13.

Ficchì, A., C. Perrin, and V. Andréassian, 2016: Impact of temporal resolution of inputs on hydrological model performance: An analysis based on 2400 flood events. *Journal of Hydrology*, **538**, 454–470.

Funk, C., and Coauthors, 2015: The climate hazards infrared precipitation with stations—a new environmental record for monitoring extremes. *Scientific data*, **2**, 1–21.

Gelaro, R., and Coauthors, 2017: The modern-era retrospective analysis for research and applications, version 2 (MERRA-2). *Journal of Climate*, **30**, 5419–5454.

Guan, B., and D. E. Waliser, 2015: Detection of atmospheric rivers: Evaluation and application of an algorithm for global studies. *Journal of Geophysical Research: Atmospheres*, **120**, 12514–12535.

Habib, E., A. T. Haile, Y. Tian, and R. J. Joyce, 2012: Evaluation of the high-resolution CMORPH satellite rainfall product using dense rain gauge observations and radar-based estimates. *Journal of Hydrometeorology*, **13**, 1784–1798.

He, Y., Y. Zhang, R. Kuligowski, R. Cifelli, and D. Kitzmiller, 2018: Incorporating satellite precipitation estimates into a radar-gauge multi-sensor precipitation estimation algorithm. *Remote Sensing*, **10**, 106.

Hong, Y., K.-L. Hsu, S. Sorooshian, and X. Gao, 2004: Precipitation estimation from remotely sensed imagery using an artificial neural network cloud classification system. *Journal of Applied Meteorology*, **43**, 1834–1853.

——, D. Gochis, J. Cheng, K. Hsu, and S. Sorooshian, 2007: Evaluation of PERSIANN-CCS rainfall measurement using the NAME event rain gauge network. *Journal of Hydrometeorology*, **8**, 469–482.

Hou, A. Y., and Coauthors, 2014: The global precipitation measurement mission. *Bulletin of the American Meteorological Society*, **95**, 701–722.

Houze Jr, R. A., 2012: Orographic effects on precipitating clouds. *Reviews of Geophysics*, **50**.

Hsu, K., X. Gao, S. Sorooshian, and H. V Gupta, 1997: Precipitation estimation from remotely sensed information using artificial neural networks. *Journal of Applied Meteorology*, **36**, 1176–1190.

Huang, Y., A. Bárdossy, and K. Zhang, 2019: Sensitivity of hydrological models to temporal and spatial resolutions of rainfall data. *Hydrology and Earth System Sciences*, **23**, 2647–2663.

Huffman, G. J., and Coauthors, 1997: The global precipitation climatology project (GPCP) combined precipitation dataset. *Bulletin of the American Meteorological Society*, **78**, 5–20.

——, and Coauthors, 2007: The TRMM multisatellite precipitation analysis (TMPA): Quasi-global, multiyear, combined-sensor precipitation estimates at fine scales. *Journal of hydrometeorology*, **8**, 38–55.

——, D. T. Bolvin, and E. J. Nelkin, 2015: Integrated Multi-satellitE Retrievals for GPM (IMERG) technical documentation. *NASA/GSFC Code*, **612**, 47.

Janowiak, J. E., R. J. Joyce, and Y. Yarosh, 2001: A real-time global half-hourly pixel-resolution infrared dataset and its applications. *Bulletin of the American Meteorological Society*, **82**, 205–218.

Joyce, R. J., and P. Xie, 2011: Kalman filter–based CMORPH. *Journal of Hydrometeorology*, **12**, 1547–1563.

——, J. E. Janowiak, P. A. Arkin, and P. Xie, 2004: CMORPH: A method that produces global precipitation estimates from passive microwave and infrared data at high spatial and temporal resolution. *Journal of hydrometeorology*, **5**, 487–503.

Katiraie-Boroujerdy, P.-S., M. Rahnamay Naeini, A. Akbari Asanjan, A. Chavoshian, K. Hsu, and S. Sorooshian, 2020: Bias Correction of Satellite-Based Precipitation Estimations Using Quantile Mapping Approach in Different Climate Regions of Iran. *Remote Sensing*, **12**, 2102.

Kidd, C., and V. Levizzani, 2011: Status of satellite precipitation retrievals. *Hydrology and Earth System Sciences*, **15**, 1109–1116.

Knapp, K. R., 2008: Scientific data stewardship of International Satellite Cloud Climatology Project B1 global geostationary observations. *Journal of Applied Remote Sensing*, **2**, 23548.

——, and Coauthors, 2011: Globally gridded satellite observations for climate studies. *Bulletin of the American Meteorological Society*, **92**, 893–907.

Krizhevsky, A., I. Sutskever, and G. E. Hinton, 2012: Imagenet classification with deep convolutional neural networks. *Advances in neural information processing systems*, **25**, 1097–1105.

Kummerow, C., and L. Giglio, 1995: A method for combining passive microwave and infrared rainfall observations. *Journal of Atmospheric and Oceanic Technology*, **12**, 33–45.

Kurino, T., 1997: A satellite infrared technique for estimating "deep/shallow" precipitation. *Advances in Space Research*, **19**, 511–514.

Lee, M., E. Im, and D. Bae, 2019: Impact of the spatial variability of daily precipitation on hydrological projections: A comparison of GCM-and RCM-driven cases in the Han River basin, Korea. *Hydrological Processes*, **33**, 2240–2257.

Lin, Y., and K. E. Mitchell, 2005: 1.2 the NCEP stage II/IV hourly precipitation analyses: Development and applications. *19th Conf. Hydrology, American Meteorological Society, San Diego, CA, USA*, Citeseer.

Liu, C., and E. J. Zipser, 2015: The global distribution of largest, deepest, and most intense precipitation systems. *Geophysical Research Letters*, **42**, 3591–3595.

Lobligeois, F., V. Andréassian, C. Perrin, P. Tabary, and C. Loumagne, 2014: When does higher spatial resolution rainfall information improve streamflow simulation? An evaluation using 3620 flood events.

Maggioni, V., P. C. Meyers, and M. D. Robinson, 2016: A review of merged high-resolution satellite precipitation product accuracy during the Tropical Rainfall Measuring Mission (TRMM) era. *Journal of Hydrometeorology*, **17**, 1101–1117.

Mahbod, M., F. Veronesi, and A. Shirvani, 2019: An evaluative study of TRMM precipitation estimates over multi-day scales in a semi-arid region, Iran. *International Journal of Remote Sensing*, **40**, 4143–4174.

Marzano, F. S., M. Palmacci, D. Cimini, G. Giuliani, and F. J. Turk, 2004: Multivariate statistical integration of satellite infrared and microwave radiometric measurements for rainfall retrieval at the geostationary scale. *IEEE transactions on Geoscience and remote sensing*, **42**, 1018–1032.

Mehran, A., and A. AghaKouchak, 2014: Capabilities of satellite precipitation datasets to estimate heavy precipitation rates at different temporal accumulations. *Hydrological Processes*, **28**, 2262–2270.

Michaelides, S., V. Levizzani, E. Anagnostou, P. Bauer, T. Kasparis, and J. E. Lane, 2009: Precipitation: Measurement, remote sensing, climatology and modeling. *Atmospheric Research*, **94**, 512–533.

Moazami, S., S. Golian, M. R. Kavianpour, and Y. Hong, 2013: Comparison of PERSIANN and V7 TRMM Multi-satellite Precipitation Analysis (TMPA) products with rain gauge data over Iran. *International journal of remote sensing*, **34**, 8156–8171.

Modarres, R., and V. de P. R. da Silva, 2007: Rainfall trends in arid and semi-arid regions of Iran. *Journal of arid environments*, **70**, 344–355.

Mosaffa, H., A. Shirvani, D. Khalili, and P. Nguyen, 2020: Post and near real-time satellite precipitation products skill over Karkheh River Basin in Iran ABSTRACT.

——, M. Sadeghi, I. Mallakpour, M. N. Jahromi, and H. R. Pourghasemi, 2022: Application of machine learning algorithms in hydrology. *Computers in Earth and Environmental Sciences*, Elsevier, 585–591.

Nazemosadat, M. J., and A. R. Ghasemi, 2004: Quantifying the ENSO-related shifts in the intensity and probability of drought and wet periods in Iran. *Journal of Climate*, **17**, 4005–4018.

Nguyen, P., A. Thorstensen, S. Sorooshian, K. Hsu, and A. AghaKouchak, 2015: Flood forecasting and inundation mapping using HiResFlood-UCI and near-real-time satellite precipitation data: The 2008 Iowa flood. *Journal of Hydrometeorology*, **16**, 1171–1183.

——, M. Ombadi, S. Sorooshian, K. Hsu, A. AghaKouchak, D. Braithwaite, H. Ashouri, and A. R. Thorstensen, 2018a: The PERSIANN family of global satellite precipitation data: a review and evaluation of products. *Hydrology and Earth System Sciences*, **22**, 5801–5816.

——, A. Thorstensen, S. Sorooshian, K. Hsu, A. Aghakouchak, H. Ashouri, H. Tran, and D. Braithwaite, 2018b: Global precipitation trends across spatial scales using satellite observations. *Bulletin of the American Meteorological Society*, **99**, 689–697.

——, and Coauthors, 2019: The CHRS Data Portal, an easily accessible public repository for PERSIANN global satellite precipitation data. *Scientific data*, **6**, 1–10.

——, and Coauthors, 2020: PERSIANN Dynamic Infrared–Rain Rate (PDIR-Now): A Near-Real-Time, Quasi-Global Satellite Precipitation Dataset. *Journal of hydrometeorology*, **21**, 2893–2906.

Ochoa-Rodriguez, S., and Coauthors, 2015: Impact of spatial and temporal resolution of rainfall inputs on urban hydrodynamic modelling outputs: A multi-catchment investigation. *Journal of Hydrology*, **531**, 389–407.

Prakash, S., V. Sathiyamoorthy, C. Mahesh, and R. M. Gairola, 2014: An evaluation of high-resolution multisatellite rainfall products over the Indian monsoon region. *International Journal of Remote Sensing*, **35**, 3018–3035.

Prat, O. P., and B. R. Nelson, 2015: Evaluation of precipitation estimates over CONUS derived from satellite, radar, and rain gauge data sets at daily to annual scales (2002–2012). *Hydrology and Earth System Sciences*, **19**, 2037.

Ralph, F. M., J. J. Rutz, J. M. Cordeira, M. Dettinger, M. Anderson, D. Reynolds, L. J. Schick, and C. Smallcomb, 2019: A scale to characterize the strength and impacts of atmospheric rivers. *Bulletin of the American Meteorological Society*, **100**, 269–289.

Raziei, T., A. Mofidi, J. A. Santos, and I. Bordi, 2012: Spatial patterns and regimes of daily precipitation in Iran in relation to large-scale atmospheric circulation. *International Journal of Climatology*, **32**, 1226–1237.

Rezaee, M., M. Mahdianpari, Y. Zhang, and B. Salehi, 2018: Deep convolutional neural network for complex wetland classification using optical remote sensing imagery. *IEEE Journal of Selected Topics in Applied Earth Observations and Remote Sensing*, **11**, 3030–3039.

Ronneberger, O., P. Fischer, and T. Brox, 2015: U-net: Convolutional networks for biomedical image segmentation. *International Conference on Medical image computing and computer-assisted intervention*, Springer, 234–241.

Rossow, W. B., and E. N. Duenas, 2004: The international satellite cloud climatology project (ISCCP) web site: An online resource for research. *Bulletin of the American Meteorological Society*, **85**, 167–172.

Rutz, J. J., W. J. Steenburgh, and F. M. Ralph, 2014: Climatological characteristics of atmospheric rivers and their inland penetration over the western United States. *Monthly Weather Review*, **142**, 905–921.

Sadeghi, M., 2018: Assessment of the PERSIANN-CDR Products Bias-corrected with the GPCP Datasets Versions 2.2 & 2.3.

——, A. Akbari Asanjan, M. Faridzad, V. Afzali Gorooh, P. Nguyen, K. Hsu, S. Sorooshian, and D. Braithwaite, 2019a: Evaluation of PERSIANN-CDR Constructed Using GPCP V2. 2 and

V2. 3 and A Comparison with TRMM 3B42 V7 and CPC Unified Gauge-Based Analysis in Global Scale. *Remote Sensing*, **11**, 2755.

——, ——, ——, ——, ——, ——, ——, and ——, 2019b: Evaluation of PERSIANN-CDR constructed using GPCP V2. 2 and V2. 3 and a comparison with TRMM 3B42 V7 and CPC unified gauge-based analysis in global scale. *Remote Sensing*, **11**, 2755.

——, A. A. Asanjan, M. Faridzad, P. Nguyen, K. Hsu, S. Sorooshian, and D. Braithwaite, 2019c: PERSIANN-CNN: Precipitation Estimation from Remotely Sensed Information Using Artificial Neural Networks–Convolutional Neural Networks. *Journal of Hydrometeorology*, **20**, 2273–2289.

——, J. Lee, P. Nguyen, K. L. Hsu, S. Sorooshian, and D. Braithwaite, 2019d: Precipitation Estimation from Remotely Sensed Information using Artificial Neural Networks-Cloud Classification System-Climate Data Record (PERSIANN-CCS-CDR). *AGUFM*, **2019**, H13P-1964.

——, P. Nguyen, K. Hsu, and S. Sorooshian, 2020: Improving near real-time precipitation estimation using a U-Net convolutional neural network and geographical information. *Environmental Modelling & Software*, **134**, 104856.

——, and Coauthors, 2021a: Application of remote sensing precipitation data and the CONNECT algorithm to investigate spatiotemporal variations of heavy precipitation: Case study of major floods across Iran (Spring 2019). *Journal of Hydrology*, **600**, 126569.

——, P. Nguyen, M. R. Naeini, K. Hsu, D. Braithwaite, and S. Sorooshian, 2021b: PERSIANN-CCS-CDR, a 3-hourly 0.04° global precipitation climate data record for heavy precipitation studies. *Scientific Data*, **8**, 1–11.

——, ——, ——, ——, and B. Dan, 2021c: 0 . 04 ° global precipitation climate data record for heavy precipitation studies. 1–11, https://doi.org/10.1038/s41597-021-00940-9.

Saghafian, B., A. Haghnegahdar, and M. Dehghani, 2017: Effect of ENSO on annual maximum floods and volume over threshold in the southwestern region of Iran. *Hydrological sciences journal*, **62**, 1039–1049.

Sellars, S., P. Nguyen, W. Chu, X. Gao, K. Hsu, and S. Sorooshian, 2013: Computational Earth science: Big data transformed into insight. *Eos, Transactions American Geophysical Union*, **94**, 277–278.

Shay-El, Y., P. Alpert, and A. Da Silva, 1999: Reassessment of the moisture source over the Sahara Desert based on NASA reanalysis. *Journal of Geophysical Research: Atmospheres*, **104**, 2015–2030.

Shearer, E. J., P. Nguyen, S. L. Sellars, B. Analui, B. Kawzenuk, K. Hsu, and S. Sorooshian, 2020: Examination of Global Midlatitude Atmospheric River Lifecycles Using an Object-Oriented Methodology. *Journal of Geophysical Research: Atmospheres*, **125**, e2020JD033425.

Shen, C., 2018: A transdisciplinary review of deep learning research and its relevance for water resources scientists. *Water Resources Research*, **54**, 8558–8593.

Smalley, M., T. L'Ecuyer, M. Lebsock, and J. Haynes, 2014: A comparison of precipitation occurrence from the NCEP Stage IV QPE product and the CloudSat Cloud Profiling Radar. *Journal of hydrometeorology*, **15**, 444–458.

Sorooshian, S., K.-L. Hsu, X. Gao, H. V Gupta, B. Imam, and D. Braithwaite, 2000: Evaluation of PERSIANN system satellite-based estimates of tropical rainfall. *Bulletin of the American Meteorological Society*, **81**, 2035–2046.

——, and Coauthors, 2011: Advanced concepts on remote sensing of precipitation at multiple scales. *Bulletin of the American Meteorological Society*, **92**, 1353–1357.

Stohl, A., and P. James, 2004: A Lagrangian analysis of the atmospheric branch of the global water cycle. Part I: Method description, validation, and demonstration for the August 2002 flooding in central Europe. *Journal of Hydrometeorology*, **5**, 656–678.

Sun, Q., C. Miao, Q. Duan, H. Ashouri, S. Sorooshian, and K. Hsu, 2018: A review of global precipitation data sets: Data sources, estimation, and intercomparisons. *Reviews of Geophysics*, **56**, 79–107.

Tao, Y., X. Gao, K. Hsu, S. Sorooshian, and A. Ihler, 2016: A deep neural network modeling framework to reduce bias in satellite precipitation products. *Journal of Hydrometeorology*, **17**, 931–945.

——, K. Hsu, A. Ihler, X. Gao, and S. Sorooshian, 2018: A two-stage deep neural network framework for precipitation estimation from Bispectral satellite information. *Journal of Hydrometeorology*, **19**, 393–408.

Tapiador, F. J., and Coauthors, 2012: Global precipitation measurement: Methods, datasets and applications. *Atmospheric Research*, **104**, 70–97.

Trenberth, K. E., A. Dai, R. M. Rasmussen, and D. B. Parsons, 2003: The changing character of precipitation. *Bulletin of the American Meteorological Society*, **84**, 1205–1218.

Vaghefi, S. A., M. Keykhai, F. Jahanbakhshi, J. Sheikholeslami, A. Ahmadi, H. Yang, and K. C. Abbaspour, 2019: The future of extreme climate in Iran. *Scientific reports*, **9**, 1–11.

Vieux, B. E., and J. M. Imgarten, 2012: On the scale-dependent propagation of hydrologic uncertainty using high-resolution X-band radar rainfall estimates. *Atmospheric research*, **103**, 96–105.

Wang, B., J. Liu, H.-J. Kim, P. J. Webster, and S.-Y. Yim, 2012: Recent change of the global monsoon precipitation (1979–2008). *Climate Dynamics*, **39**, 1123–1135.

Weng, F., L. Zhao, R. R. Ferraro, G. Poe, X. Li, and N. C. Grody, 2003: Advanced microwave sounding unit cloud and precipitation algorithms. *Radio Science*, **38**.

Wentz, F. J., L. Ricciardulli, K. Hilburn, and C. Mears, 2007: How much more rain will global warming bring? *Science*, **317**, 233–235.

Westrick, K. J., C. F. Mass, and B. A. Colle, 1999: The limitations of the WSR-88D radar network for quantitative precipitation measurement over the coastal western United States. *Bulletin of the American Meteorological Society*, **80**, 2289–2298.

Xie, P., and P. A. Arkin, 1997: Global precipitation: A 17-year monthly analysis based on gauge observations, satellite estimates, and numerical model outputs. *Bulletin of the American Meteorological Society*, **78**, 2539–2558.

——, J. E. Janowiak, P. A. Arkin, R. Adler, A. Gruber, R. Ferraro, G. J. Huffman, and S. Curtis, 2003: GPCP pentad precipitation analyses: An experimental dataset based on gauge observations and satellite estimates. *Journal of Climate*, **16**, 2197–2214.

——, A. Yatagai, M. Chen, T. Hayasaka, Y. Fukushima, C. Liu, and S. Yang, 2007: A gauge-based analysis of daily precipitation over East Asia. *Journal of Hydrometeorology*, **8**, 607–626.

Yadav, R. K., 2016: On the relationship between Iran surface temperature and northwest India summer monsoon rainfall. *International Journal of Climatology*, **36**, 4425–4438.

Yamashita, R., M. Nishio, R. K. G. Do, and K. Togashi, 2018: Convolutional neural networks: an overview and application in radiology. *Insights into imaging*, **9**, 611–629.

Yang, J., M. N. Nguyen, P. P. San, X. L. Li, and S. Krishnaswamy, 2015: Deep convolutional neural networks on multichannel time series for human activity recognition. *Twenty-fourth international joint conference on artificial intelligence*.

Yilmaz, K. K., T. S. Hogue, K.-L. Hsu, S. Sorooshian, H. V Gupta, and T. Wagener, 2005: Intercomparison of rain gauge, radar, and satellite-based precipitation estimates with emphasis on hydrologic forecasting. *Journal of Hydrometeorology*, **6**, 497–517.

Yong, B., D. Liu, J. J. Gourley, Y. Tian, G. J. Huffman, L. Ren, and Y. Hong, 2015: Global view of real-time TRMM multisatellite precipitation analysis: Implications for its successor global precipitation measurement mission. *Bulletin of the American Meteorological Society*, **96**, 283–296.

Yoshimoto, S., and G. Amarnath, 2017: Applications of satellite-based rainfall estimates in flood inundation modeling—A case study in Mundeni Aru River Basin, Sri Lanka. *Remote Sensing*, **9**, 998.

Zarrin, A., H. Ghaemi, M. Azadi, and M. Farajzadeh, 2010: The spatial pattern of summertime subtropical anticyclones over Asia and Africa: A climatological review. *International Journal of Climatology: A Journal of the Royal Meteorological Society*, **30**, 159–173.

Zhu, X. X., D. Tuia, L. Mou, G.-S. Xia, L. Zhang, F. Xu, and F. Fraundorfer, 2017: Deep learning in remote sensing: A comprehensive review and list of resources. *IEEE Geoscience and Remote Sensing Magazine*, **5**, 8–36.